KAYAKING AND WAGGING OF
RIGID ROD-LIKE COLLOIDS IN SHEAR FLOW

Yu-Guo TAO

Front cover: *The path of the director of a kayaking (left) and wagging (right) system of rod-like particles on the unit sphere*

Back cover: *Snapshots of rigid rods collectively changing their orientations by 180 degrees*

Typeset in LaTeX, by the author

KAYAKING AND WAGGING OF
RIGID ROD-LIKE COLLOIDS IN SHEAR FLOW

DISSERTATION

to obtain

the doctor's degree at the University of Twente,

on the authority of the rector magnificus,

prof. dr. H.W.M. Zijm,

on account of the decision of the graduation committee,

to be publicly defended

on Friday, 12 May 2006 at 16.45

by

Yu-Guo TAO

born on 8 September 1975

in Changchun, P. R. China

This dissertation has been approved by:

the promoter

Prof. dr. W.J. Briels

and the assistant-promoter

Dr. ir. W.K. den Otter

Contents

1 Introduction

1.1 Liquid crystalline polymers

Liquid crystalline polymers are beautiful examples of materials that both fascinate from a fundamental point of view — they form complex fluids with intriguing symmetries and unusual elastic properties — and are highly interesting for technological applications. Liquid crystals possess spontaneous orientational order but lack the full three-dimensional positional order of solid crystals. Crystals consisting of spherically symmetric molecules can have positional order, while those consisting of less symmetrical molecules, *e.g.*, rod-like or disk-like molecules, can have orientational order. Positional order implies that the molecules' centers of mass tend to lie on lattice points, while orientational order implies that molecules tend to point in the same direction.

Fig. 1.1 shows some typical configurations of hard spherocylinders, which represent isotropic, nematic, smectic-A and solid phases, respectively. In the isotropic state, the liquid crystalline polymers are randomly displaced and there is no favored direction of their end to end vectors. In the uniaxial nematic phase, molecules prefer to point along a special direction designated by a unit vector $\hat{\mathbf{n}}$ called the director. $\hat{\mathbf{n}}$ is the eigenvector of the orientational order parameter tensor $\mathbf{S}$ with respect to its largest eigenvalue P_2 which measures the degree of orientational order and can also be defined as $P_2 \equiv \frac{3}{2}\langle\cos^2(\theta)\rangle - \frac{1}{2}$, where θ is the angle between the long axis of a particle and the average orientation $\hat{\mathbf{n}}$ of all particles. In the isotropic phase the scalar orientational order parameter P_2 is zero, while in the nematic state P_2 becomes nonzero, reaching unity when all molecules point in the same direction. Smectic-layered materials can be either liquid crystalline or crystalline, depending on the presence or absence of long-range three-dimensional order. Besides the simplest smectic-A, there are

1
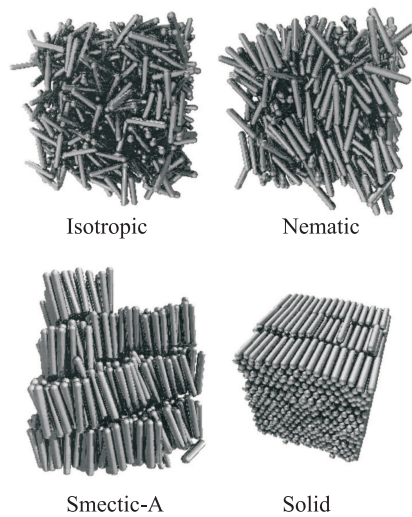
Figure 1.1: *Typical configurations for hard spherocylinders with $L/D = 5$. These four snapshots present isotropic, nematic, smectic-A and solid phases, respectively. (adapted from Ref. 101)*

many other smectic structures, which are well described by Gray and Goodby [54].

There are two types of liquid-crystalline polymers (LCPs): thermotropic LCPs lack solvent and their phase transitions are driven by temperature changes; lyotropic LCPs mix with solvent and their phase transitions are driven by concentration changes. In this thesis, we focus on the concentration-dependent lyotropic LCPs, and our research interests are in the regions of isotropic and nematic order.

1.2 Rod-like colloidal system : the *fd* virus

In the 1960's, Hoffmann-Berling [66, 100], who was very familiar with bacteria and viruses, purified two previously unknown bacteriophages from Escherichia coli extracted from a manure pile. He named one of the phages, which contained a single-stranded DNA, the *fd* virus. The second virus proved to be an example of a single-stranded RNA bacteriophage and was named *fr* virus. Although at that time all known bacteriophages were spherical, electron microscopy and X-ray crystallography revealed the rod-shaped helical structure of the *fd* virus.

Therefore the *fd* virus proved to be the first example of a filamentous bacteriophage. Later on, the analysis of *fd*'s protein shell showed that its viral capsid was unusually stable. Compared to other viruses, *fd* was not only difficult to break apart, but also reaggregated rapidly when individual units were mixed together.
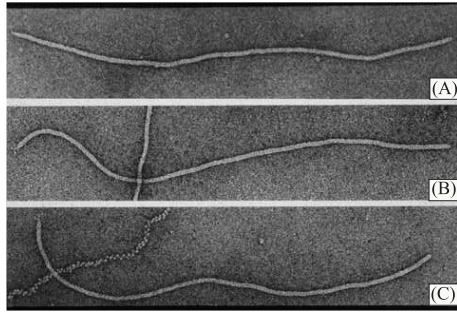
Figure 1.2: *Electron micrograph of single fd virus. (adapted from Ref. 104)*

Fig. 1.2 shows three Transmission Electron Microscopy (TEM) images of *fd* viruses. The *fd* virus consists of a single-stranded circular DNA molecule coated with a protein layer of 2700 identical protein subunits. The slightly flexible *fd* virus has a contour length of $L = 880$ nm and a diameter of $D = 6.6$ nm, as obtained with electron microscopy [30, 47, 88]. The persistence length of this virus is $L_P = 2200$ nm, which is about 2.5 times its contour length. The *fd* molecules are charged, resulting in an effective diameter which is larger than the above mentioned thickness of 6.6 nm. From Onsager's expression for the effective diameter of a charged rod [114] a diameter of 14.8 nm is obtained, resulting in an effective aspect ratio L/D of 60.

The *fd* virus is a good model system to study liquid crystalline behavior experimentally, not only because it is easily grown in large quantities, very monodisperse and very stable in solution, but also because it is easy to use standard molecular cloning techniques to alter the basic properties of the virus. The *fd* virus is considered an excellent representative for hard spherocylinder (HSC), irrespective of its inherent small flexibility. Some dynamical and rheological properties of these biomacromolecules are comparable with those obtained by theoretical investigations and computer simulations of rigid rods.

1.3 Isotropic-nematic phase transition of rod-like colloidal systems
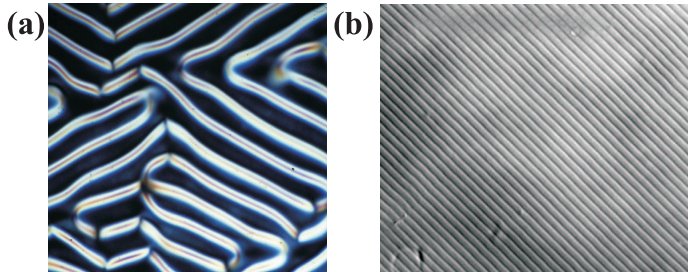
Figure 1.3: *Optical birefringent micrographs of fd viruses in (a) nematic and (b) smectic solution. (adapted from http://www.elsie.brandeis.edu/Picture_Archive/)*

Fd viruses can form, in order of increasing concentration, a stable isotropic and nematic phase, and even a smectic phase at extremely high concentrations. Micrographs of the later two are shown in Fig. 1.3. Theoretically, according to Onsager [113, 114] a concentrated homogeneous system of non-spherical colloidal particles can become unstable or meta-stable with respect to fluctuations in orientation. This can induce concentration differences and finally lead to a separation into a low concentration phase and a high concentration phase. In the low concentration phase, the particles are in an orientationally disordered isotropic phase; while in the high concentration phase, the particles are in an orientationally ordered nematic phase. Two kinds of phase transition concentrations should be distinguished. One of them is called the binodal concentration, which measures the concentration of the isotropic or nematic phase in thermodynamic equilibrium with the other phase. The other one is named the spinodal concentration, which is defined as the concentration at which a homogeneous system becomes absolutely unstable. In other words, the spinodal separates the (meta-) stable region from the unstable region in the phase diagram.

In the experiments on *fd* viruses [30, 88], the two binodal concentrations are found to be equal to 13.0 mg/ml and 14.5 mg/ml, respectively. Using a molar mass of 1.64×10^7 g/mol, these correspond to $L\varphi/D = 4.5$ and 4.8, respectively, where φ is the volume fraction. These values are higher than the theoretically predicted values of 3.329 and 4.219 by Onsager [114].

The discrepancy is probably due to the slight flexibility of the *fd* virus and the tendency of the rods to acquire mutually perpendicular orientations due to their charges.

For solutions of very long and thin rods, the binodal concentrations are relatively easily determined experimentally: one can measure directly the concentrations of the two phases after phase separation. Theoretically, the binodal points have been determined using different approximations in minimizing Onsager's function for the free energy. These theoretically predicted binodal concentrations of rod-like colloids have been confirmed by computer simulations for various shape anisotropies L/D [10]. For a more complete description of binodal concentrations, we refer to a detailed review article of Vroege and Lekkerkerker [139] and references given there in.

Spinodal points, on the other hand, are difficult to obtain experimentally, because one has to perform a concentration quench from a phase with a relatively lower or higher concentration into a two-phase region, where the initial state is either isotropic or nematic. The two spinodal concentrations can not be detected with arbitrary accuracy, because close to the theoretical spinodal on the (meta-) stable side, the amplitude of the order parameter fluctuation necessary to initiate demixing is very small. When the free energy barrier to demixing is less than about $k_B T$, the demixing will occur immediately, making a sharp experimental determination of the location of the spinodal impossible.

The spinodal concentration can be calculated from thermodynamic considerations, since, by definition, the spinodal is the set of variables where the free energy barrier for phase separation becomes equal to zero. The location of the spinodal can be obtained by a linear stability analysis of the equation of motion. The set of thermodynamic controlled variables (we consider the concentration in the current work) where the equation of motion becomes absolutely unstable defines the spinodal. This kinetic definition of the spinodal should reduce to the usual thermodynamic definition. For rod-like colloidal systems, the spinodal points can be obtained theoretically when the equation of motion for the orientational order parameter tensor predicts unstable behavior beyond some concentration. In the current work, we treat the system by means of Brownian dynamics simulation. We can therefore analyze the fluctuations of the orientational order, and find the spinodal concentrations, directly. To this end, in the simulations we measure the orientational order parameter tensor $\mathbf{S}$, defined as

$$\mathbf{S}(t) = N^{-1} \sum_i \hat{\mathbf{u}}_i(t) \hat{\mathbf{u}}_i(t) - \frac{1}{3}\hat{\mathbf{I}}, \qquad (1.1)$$

where $\hat{\mathbf{u}}_i(t)$ describes the orientation of rod i at time t. N denotes the total number of particles while $\hat{\mathbf{I}}$ is the unit matrix. As already mentioned in Section 1.1, the largest eigenvalue P_2 of the tensor $\mathbf{S}$ measures the degree of nematic alignment of rods. $P_2 = 0$ denotes that the system is in the isotropic state, while $P_2 = 1$ stands for a perfectly aligned state.
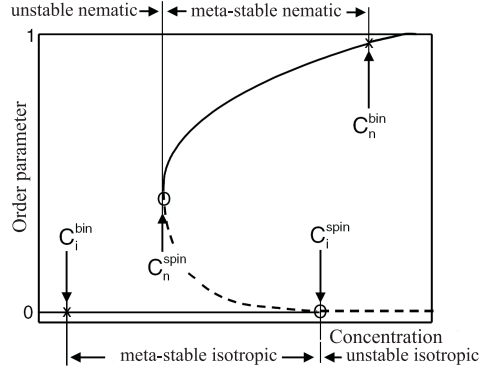
Figure 1.4: *The bifurcation phase diagram, which indicates various meta- and unstable regions for the two different homogeneous suspensions. Here, $\times$ and $\bigcirc$ are used to denote binodal and spinodal points, respectively. (adapted from Ref. 26)*

In the bifurcation phase diagram of homogeneous systems in Fig. 1.4, the scalar orientational order parameter P_2 is plotted against the concentration. In equilibrium, there is an isotropic phase with concentration C_i^{bin} in coexistence with a nematic phase with concentration C_n^{bin}, after completion of the phase separation. The two solid lines stand for stable stationary solutions of the equation of motion for the orientational order parameter tensor, while the dashed lines represent unstable stationary solutions. The isotropic state becomes unstable when the system concentration is larger than the critical spinodal concentration, C_i^{spin}, while the nematic state becomes unstable at concentrations lower than another spinodal concentration, C_n^{spin}. On the one hand, when the system concentration is above C_i^{spin}, the isotropic state is still a stationary solution, but unstable; on the other hand, when the concentration is below C_n^{spin}, there is no nematic state which is a stationary solution of the equation of motion. The two spinodal concentrations C_i^{spin} and C_n^{spin} are connected by a separatrix which separates the basins of attraction for the isotropic and nematic state. A homogeneous initial state above this

separatrix develops a higher degree of alignment, while an initial state below the separatrix becomes more isotropic.

It is known that shear flow increases the tendency of rod-like colloids to align along the flow direction. An initial stable isotropic rod system will slightly align in the presence of shear flow and form a paranematic phase, where the degree of alignment is lower than that in a nematic phase. Therefore, the spinodal concentrations will be shifted to lower values when an external shear flow is applied. Unfortunately, phase coexistence and the kinetics of phase transition in lyotropic solutions of rigid rods in shear flow are less well understood [24, 112].

In principle, the spinodal points can be obtained numerically by solving the equation of motion of the orientational order parameter tensor **S**. Some approximations then have to be introduced due to the complexity of this tensor. Dhont and Briels [24] developed theoretically a bifurcation diagram from the equation of motion for the orientational order parameter tensor in shear flow and worked out a set of non-equilibrium spinodals for infinitely long and thin rod systems. The only experimental evidence, based on suspensions of *fd* viruses [88], shows difficulties in the investigation of the shear-induced shift of the isotropic-nematic spinodals. Computer simulations are therefore needed to provide further information.

1.4 Collective periodic orientational motions of rigid rods in shear flow

In a simple plane Couette shear flow, the flow field $\mathbf{V}(\mathbf{r})$ is given by

$$\mathbf{V}(\mathbf{r}) = \mathbf{\Gamma} \cdot \mathbf{r} = \begin{pmatrix} 0 & \dot{\gamma} & 0 \\ 0 & 0 & 0 \\ 0 & 0 & 0 \end{pmatrix} \cdot \mathbf{r}, \tag{1.2}$$

where $\dot{\gamma}$ is the shear rate and $\mathbf{\Gamma}$ is the velocity gradient tensor. Anczurowski and Mason [3, 4] observed experimentally that a single rigid rod-like particle rotates indefinitely when the long axis of the rod is in the shear plane (the plane parallel to both the flow and the gradient direction), which was investigated theoretically and named Jeffery orbit [70]. The rod rotates slowly when its long axis is nearly parallel to the flow direction, but rapidly otherwise.

Nematic solutions of rigid rods exhibit collective periodic orientational motions, *i.e.*, tum-

bling, kayaking, wagging, flow-aligning or log-rolling, depending on the applied shear rates and the initial configurations of the systems. This fascinating dynamical phenomenon was first investigated theoretically by Hess [59] and Doi [33]. They independently studied homogeneous systems of rigid Brownian rods with infinite aspect ratio. In the Doi-Hess model, the key object is the time evolution of the orientational distribution function (ODF) $\psi(\hat{\mathbf{u}}, t)$, which gives the probability density that a rod is oriented along $\hat{\mathbf{u}}$ at time t. The kinetic equation, which describes the dynamics of rod-like polymers, is derived as

$$\frac{\partial \psi}{\partial t} = \mathrm{D}_r \frac{\partial}{\partial \hat{\mathbf{u}}} \cdot \left[\frac{\partial \psi}{\partial \hat{\mathbf{u}}} + \frac{\psi}{k_B T} \frac{\partial V(\hat{\mathbf{u}})}{\partial \hat{\mathbf{u}}} \right] - \frac{\partial}{\partial \hat{\mathbf{u}}} \cdot \left(\frac{\partial \hat{\mathbf{u}}}{\partial t} \psi \right) , \tag{1.3}$$

where D_r is the constant rotational diffusion coefficient and $k_B T$ is the thermal energy. The partial derivative with respect to $\hat{\mathbf{u}}$ represents the gradient over the unit sphere. $V(\hat{\mathbf{u}})$ represents a mean field nematic potential, which is approximated by the Maier-Saupe [95] form:

$$V(\hat{\mathbf{u}}) = -\frac{3}{2} U k_B T \langle \hat{\mathbf{u}}\hat{\mathbf{u}} \rangle : \hat{\mathbf{u}}\hat{\mathbf{u}} , \tag{1.4}$$

where U is a dimensionless potential intensity and the brackets denote ensemble averaging.

The Doi-Hess model has been extended with some closure approximations, which shows that it is indeed capable of predicting most rheological responses of liquid crystalline polymers in the nematic phase. Marrucci and Maffettone [97, 98, 99] analyzed the Doi-Hess equation numerically by reducing the orientational distribution function in two dimensions. Larson and Öttinger [80, 84] solved this model by expanding the ODF in spherical harmonic functions. In these ways, various types of motions, *e.g.*, in-plane tumbling, out-of-plane kayaking, wagging, flow-aligning, as well as log-rolling were investigated.

In contrast to theoretical works, experimental observations [91] show great difficulties in measuring these periodic motions. Existing computer simulations of sheared systems are limited to either isotropic solutions of rods [142] or ellipsoid systems with small aspect ratios [106]. We therefore perform Brownian dynamics simulation to investigate the orientational behavior of concentrated liquid crystalline polymers in shear flow.

1.5   Brownian dynamics simulation

Computer simulation is an increasingly valuable supplement to experiment and theory in the quest to understand complex liquids. It provides a direct route from the microscopic details

of a system to the macroscopic properties of experimental interests. The advantage of simulation is that they can be aimed at either molecular or microstructure length scales. The most widely used molecular-scaled simulation methods are molecular dynamics (MD), Brownian dynamics (BD) and Monte Carlo sampling (MC). Molecular dynamics is the most detailed simulation method, where Newton's equations of motion are solved for a large collection of molecules which interact with each other via intermolecular potentials. For fluids that contain large polymer molecules or colloidal particles in a small-molecule solvent, this method becomes inefficient, because the typical time step in the simulation must be scaled to the motions of fast-moving solvent particles. This leads to an insufficient probing of the interesting large scale motions of large polymer molecules or particles. The Monte Carlo sampling method generates a large number of configurations or microstates of the equilibrated system by stepping from one microstate to the next in small random increments. It is not particularly well suited to simulate time-dependent phenomena.

In a simulation of very large molecules or a collection of heavy ions in a solvent, the motions of the solvent molecules are of little interest, but they will make a full molecular dynamics simulation very expensive. This difficulty has successfully been circumvented by the development of Brownian dynamics [39, 135], which shows a high efficiency for simulating complex fluids. In Brownian dynamics simulations, the positions and momenta of the small solvent molecules do not appear and the effects of these solvent molecules on the solute are considered by a combination of random and frictional forces. In other words, the Brownian motion of the large solute particles, which is produced by the random collisions with solvent molecules, can be treated by a stochastic force generated by random numbers. In this way, Newton's equations of motion are replaced by a Langevin equation:

$$\frac{d\mathbf{p}_i}{dt} = -\zeta_i(\dot{\mathbf{x}}_i - \mathbf{v}^s) + \mathbf{F}_i^c + \mathbf{F}_i^b \, , \tag{1.5}$$

where $\mathbf{p}_i$ is the momentum of particle i and $\mathbf{x}_i$ its position coordinate. ζ_i is a friction coefficient which represents viscous dissipation. $\mathbf{v}^s$ denotes the local solvent velocity, which is controlled by the imposed flow field, *e.g.*, a shear flow in this study. $\mathbf{F}_i^c$ is the conservative force acting on particle i produced by intermolecular interaction, while $\mathbf{F}_i^b$ is the Brownian force which has zero mean and variance of

$$\langle \mathbf{F}_i^b(t)\mathbf{F}_i^b(0) \rangle = 2k_B T \zeta_i \delta(t) \, , \tag{1.6}$$

where $\delta(t)$ is the Dirac delta function.

To update the position $\mathbf{x}_i$ of each Brownian particle, one has to carry out two integrations: the momentum and the position coordinate. On the diffusive time scale (also known as the Smoluchowski time scale), the momentum is in thermal equilibrium with the solvent. For constant ζ_i, the average of Eq. (1.5) equals zero. By doing so, one arrives at

$$\frac{d\mathbf{x}_i}{dt} = \mathbf{v}^s + \zeta_i^{-1}(\mathbf{F}_i^c + \mathbf{F}_i^b) \,. \tag{1.7}$$

This integrated Langevin equation, which only involves the position coordinates, is thus ready to be solved. See *Chapter* 2 for more details.

In the Langevin equations of motion, the temperature of the system is set by the amplitude of the autocorrelation function of the imposed stochastic force, which is proportional to $k_B T$ according to Eq. (1.6). This will prevent the occurrence of temperature drift due to accumulated integration errors. In the overdamped case, when Brownian dynamics applies, the system looses its memory of the initial velocities long before its configuration has changed appreciably. Thus, the velocities are eliminated altogether and the time step is adjusted to the rate of change of the configuration. On the diffusive time scale, the average force acting on a particle is considered equal to zero, indicating that the mass of a particle plays no role in Brownian dynamics simulation.

The problem of surface effects in a finite simulation box can be overcome by implementing periodic boundary conditions [1]: a rectangular box is replicated throughout space to form an infinite lattice. When a molecule moves in the original box, its periodic images in each of the neighboring boxes move in the exact same way. Thus when a molecule leaves the central box, one of its images will enter through the opposite face. There are no walls at the boundary of the central box and no surface molecules. The number density in the central box and hence in the entire system is conserved. The box simply forms a convenient axis system for measuring the coordinates of the N molecules. The periodic boundary conditions can introduce a small effect on some equilibrium thermodynamic properties or structures of fluids. However, when the simulation box size (as well as the number of simulated particles) is chosen effectively large enough, the properties of a small infinitely periodic system and the macroscopic system which it represents can be proved to be the same.

1.6   Thesis outline

This thesis describes Brownian dynamics simulations of rigid long and thin rod-like colloids. We investigate the rotational diffusivities, isotropic-nematic phase transitions, periodic orientational motions and some rheological properties, *i.e.*, viscosities and normal stress differences of rigid spherocylinders in shear flow by a newly developed Brownian dynamics simulation program. This program is then transplanted, with few changes, to study some dynamical properties of sheared colloidal crystals. The thesis is organized as follows.

In *Chapter 2*, we present the calculated self and collective rotational diffusion coefficients of rods in dilute or semi-dilute solutions by means of Brownian dynamics simulation. In this simulation algorithm, we take the excluded volume interactions between rods into account but neglect hydrodynamic interactions. The simulation results are compared with a recent microscopic theory of rigid long thin rods by Dhont and Briels [24].

The Brownian dynamics simulation method described in *Chapter 2* proves disadvantageous when applied to concentrated solutions of rods. Therefore, we developed a new event-driven algorithm, which exhibits great success in investigating the dynamical properties of dense rod systems. The isotropic-nematic phase transitions in solutions of rigid rods with various aspect ratios are described in *Chapter 3*. The influences of shear can also be taken into account in this new simulation method, allowing us to study the shear induced shift of isotropic-nematic spinodals.

In *Chapter 4*, we present some preliminary results of the dynamics of dense solutions of rigid rods in shear flow. Various collective orientational motions *i.e.*, tumbling, kayaking, wagging, flow-aligning and log-rolling, have been "observed". This is the first time that the periodic orientational motions of concentrated rigid liquid crystalline polymers with large aspect ratio have been simulated. Our results agree very well with theoretical predictions for rigid rods and experimental measurements of *fd* viruses.

A detailed description of the periodic orientational motions of nematic solutions of rigid rods is presented in *Chapter 5*. Solutions of rods with various aspect ratios and volume fractions are investigated in the plane Couette shear flow with different steady rates. The dependence of the kayaking period on the applied shear rate, the shape anisotropy and the volume fraction are deduced from the simulation results. Transitions between different types of motions are also studied by applying shear flows with different rates.

The event-driven Brownian dynamics simulation investigation is then focused on some rheological properties of solutions of rigid rods. In *Chapter 6*, we report on the simulated viscosities as well as the first and the second normal stress differences in both isotropic and nematic states. Besides observing a shear thinning behavior, unusual oscillations of the normal stress differences against shear rate are also detected, showing qualitative agreements with both theories and experiments.

At the end of the Thesis, the results are summarized in both English and Dutch.

2 Self and collective rotational diffusion coefficients of rigid long thin rods

Recently a microscopic theory for the dynamics of suspensions of long thin rigid rods was presented, confirming and expanding the well-known theory by Doi, Edwards and Kuzuu. Here this theory is put to the test by comparing it against computer simulations. A Brownian dynamics simulation program was developed to follow the dynamics of the rods, with a length over a diameter ratio of 60, on the Smoluchowski time scale. The model accounts for excluded volume interactions between rods, but neglects hydrodynamic interactions. The self rotational diffusion coefficients $D_r(\varphi)$ of the rods were calculated by standard methods and by a new, more efficient method based on calculating average restoring torques. Collective decay of orientational order was calculated by means of equilibrium and nonequilibrium simulations. Our results show that, for the currently accessible volume fractions, the decay times in both cases are virtually identical. Moreover, the observed decay of diffusion coefficients with volume fraction is much quicker than predicted by the theory, which is attributed to an oversimplification of dynamic correlations in the theory. [*]

2.1 Introduction

Suspensions of rigid rod-like colloids dissolved in Newtonian liquids are of great importance both in biological and in industrial applications. Already in the first half of the previous

---

[*] The work described in this chapter previously appeared in J. Chem. Phys. **122**, 244903 (2005).

century, Onsager [113, 114] understood that very long and thin rods will display interesting thermodynamic phase behavior at very low volume fractions. The complete phase diagram for varying aspect ratios and volume fractions was determined a decade ago by Bolhuis and Frenkel [10, 11] by means of Monte Carlo simulation. In dilute solutions, the basic equation describing the dynamics of rigid long thin rods is well established [23, 25, 36] and the dynamical properties have been calculated by various authors [27, 64, 86, 142, 143]. The self orientational diffusion of rods in semidilute or concentrated solution, however, is difficult to understand quantitatively due to the complexity of the restoring torque exerted by surrounding rods. A theoretical analysis is very complicated because in principle both excluded volume interactions and hydrodynamic interactions have to be taken into account. Fortunately, it may be argued [24] that the latter are negligible for very large aspect ratios L/D, where L is the length of the rods and D their diameter. Even then, the problem remains to be very tough and results are only obtained on the basis of severe approximations.

In this Chapter, we present the results of Brownian dynamics simulations of a system of interacting rods without hydrodynamic interactions. A justification for the neglect of the latter has been presented in Ref. 24. Besides this justification, the main reason to neglect hydrodynamic interactions in this work is that we intend to provide results with which to compare the theoretical predictions. Any possible deviation between theoretical prediction and corresponding simulation results must then be due to one or more of the remaining approximations in the theory.

In section 2.2 we briefly discuss these approximations mentioned above. In section 2.3 we describe our simulation model, which we prove in Appendix 2.B to be equivalent to the Smoluchowski equation on which the theory is based. Excluded volume interactions are modeled with a pairwise interaction potential whose terms are proportional to the overlap volume of the corresponding pair of rods. It will be shown that this potential is accurate enough to simulate collections of hard rods. In section 2.4 we present the results of our simulations and compare them to the corresponding theoretical prediction. Finally in section 2.5 we summarize our findings.

2.2 Theory

For long and thin rigid rod-like colloids suspended in Newtonian liquids, the fundamental equation of motion, in the overdamped limit, is the N-particle Smoluchowski equation, describing the time evolution of the probability density function (pdf) of the phase space coordinates of the rods. When hydrodynamic interactions between rods are neglected, integration of the N-particle Smoluchowski equation for a very large aspect ratio leads to (see Appendix 2.A)

$$\frac{\partial}{\partial t}P(\hat{\mathbf{u}},t) = D_r\hat{\mathscr{R}} \cdot \left\{ \hat{\mathscr{R}}P(\hat{\mathbf{u}},t) - \beta P(\hat{\mathbf{u}},t)\bar{\mathbf{T}}(\hat{\mathbf{u}},t) \right\} . \tag{2.1}$$

Here, $P(\hat{\mathbf{u}},t)$ is the one-particle pdf of the orientation $\hat{\mathbf{u}}$ of some rod, with $\hat{\mathbf{u}}$ being the unit vector along the long axis of the rod at time t. The rotational operator $\hat{\mathscr{R}} \equiv \hat{\mathbf{u}} \times \frac{\partial}{\partial \hat{\mathbf{u}}}$ plays a role analogous to that of the gradient operator ∇_r in translational diffusion. β is defined as $1/k_B T$ with Boltzmann constant k_B and temperature T, and D_r is the rotational diffusion coefficient of a single rod

$$D_r = \frac{k_B T}{\gamma_r} = \frac{3k_B T \ln(L/D)}{\pi \eta_s L^3} , \tag{2.2}$$

where γ_r is the rotational friction coefficient and η_s the viscosity of the solvent. The average torque acting on the central rod $\bar{\mathbf{T}}(\hat{\mathbf{u}},t)$ in Eq. (2.1) is expressed as

$$\bar{\mathbf{T}}(\hat{\mathbf{u}},t) = -\bar{\rho} \int d\mathbf{r}' \oint d\hat{\mathbf{u}}' \, \bar{P}(\hat{\mathbf{u}}',t)g(\mathbf{r}-\mathbf{r}',\hat{\mathbf{u}},\hat{\mathbf{u}}',t)\hat{\mathscr{R}}V(\mathbf{r}-\mathbf{r}',\hat{\mathbf{u}},\hat{\mathbf{u}}') , \tag{2.3}$$

where $\bar{\rho}$ is the number density of rods and $V(\mathbf{r}-\mathbf{r}',\hat{\mathbf{u}},\hat{\mathbf{u}}')$ is the pair-interaction potential for two rods with orientations $\hat{\mathbf{u}}$ and $\hat{\mathbf{u}}'$ and center-center separation $\mathbf{r}-\mathbf{r}'$; because of translational invariance the pair correlation function $g(\mathbf{r}-\mathbf{r}',\hat{\mathbf{u}},\hat{\mathbf{u}}',t)$ depends on $\mathbf{r}-\mathbf{r}'$ instead of $\mathbf{r}$ and $\mathbf{r}'$ separately and consequently $\bar{\mathbf{T}}(\hat{\mathbf{u}},t)$ does not depend on $\mathbf{r}$. $\bar{P}(\hat{\mathbf{u}}',t)$ is the one-particle pdf of the surrounding rods.

A few remarks about the average torque $\bar{\mathbf{T}}(\hat{\mathbf{u}},t)$ and its use in Eq. (2.1) should be made at this point. First, we note that the most basic equation of motion describing the dynamics of our system, the N-particle Smoluchowski equation, is a first order differential equation of time. Therefore, it requires for its solution a precise description of the initial N-particle pdf, the initial state for short, which obviously depends on the specific experiment that we want to describe. The ensuing N-particle pdf at later times, and consequently the corresponding

reduced pdf's such as $P(\hat{\mathbf{u}},t)$, $\bar{P}(\hat{\mathbf{u}}',t)$ and $g(\mathbf{r}-\mathbf{r}',\hat{\mathbf{u}},\hat{\mathbf{u}}',t)$, will depend on this initial state as well. Now suppose that during our experiment we only monitor the one-particle pdf $P(\hat{\mathbf{u}},t)$. Equation (2.1) then in principle suffices to describe our results. In order to solve this equation, however, we need to specify the average torque $\bar{\mathbf{T}}(\hat{\mathbf{u}},t)$, which according to Eq. (2.3) and the remarks just made depends on the initial state. In Eq. (2.3), depending on the specific experiment under investigation, $\bar{P}(\hat{\mathbf{u}},t)$ may be equal to $P(\hat{\mathbf{u}},t)$ or not. To describe the decay of a single rod initially aligned along $\hat{\mathbf{u}}_0$ in an isotropic environment, $\bar{P}(\hat{\mathbf{u}},t)=1/4\pi$ while $P(\hat{\mathbf{u}},t)$ decays from $P(\hat{\mathbf{u}},0)=\delta(\hat{\mathbf{u}}-\hat{\mathbf{u}}_0)$ to $P(\hat{\mathbf{u}},\infty)=1/4\pi$. To study the decay of rods which are all initially aligned along $\hat{\mathbf{u}}_0$, $\bar{P}(\hat{\mathbf{u}},t)=P(\hat{\mathbf{u}},t)$ at all times.

In Ref. 24 only the case with $\bar{P}(\hat{\mathbf{u}},t)=P(\hat{\mathbf{u}},t)$ has been investigated. Moreover, for analytical purposes, Dhont and Briels [24] neglect all dynamical correlations and put $g(\mathbf{r}-\mathbf{r}',\hat{\mathbf{u}},\hat{\mathbf{u}}',t)$ equal to its equilibrium value $g(\mathbf{r}-\mathbf{r}',\hat{\mathbf{u}},\hat{\mathbf{u}}')$. Next, following Onsager [113, 114], for long and thin rods they write

$$g(\mathbf{r}-\mathbf{r}',\hat{\mathbf{u}},\hat{\mathbf{u}}') = \exp\left\{-\beta V(\mathbf{r}-\mathbf{r}',\hat{\mathbf{u}},\hat{\mathbf{u}}')\right\} . \tag{2.4}$$

With this approximation, the torque is given by [24]

$$\bar{\mathbf{T}}(\hat{\mathbf{u}},t) = -2\beta^{-1}DL^2\bar{\rho}\hat{\mathscr{R}}\oint d\hat{\mathbf{u}}' \, P(\hat{\mathbf{u}}',t)\left|\hat{\mathbf{u}}\times\hat{\mathbf{u}}'\right| . \tag{2.5}$$

In a final step, they use a Ginzburg-Landau type expansion of $\left|\hat{\mathbf{u}}\times\hat{\mathbf{u}}'\right|$ in the above equation:

$$\left|\hat{\mathbf{u}}\times\hat{\mathbf{u}}'\right| \approx \frac{5\pi}{16}\left(1-\frac{3}{5}\hat{\mathbf{u}}\hat{\mathbf{u}}:\hat{\mathbf{u}}'\hat{\mathbf{u}}'\right) . \tag{2.6}$$

Note that in this expansion a factor of $\sqrt{2/3}$ has been replaced by $\pi/4$ for cosmetic reasons (with 3.8% deviation). Evaluation of the average torque $\bar{\mathbf{T}}(\hat{\mathbf{u}},t)$ then leads to [24]

$$\bar{\mathbf{T}}(\hat{\mathbf{u}},t) = -\frac{5}{2}\beta^{-1}\left(\frac{L}{D}\varphi\right)\hat{\mathscr{R}}\left\{1-\oint d\hat{\mathbf{u}}'\,\hat{\mathbf{u}}'\hat{\mathbf{u}}'P(\hat{\mathbf{u}}',t):\hat{\mathbf{u}}\hat{\mathbf{u}}\right\} , \tag{2.7}$$

where φ is the volume fraction of rods.

We now introduce a quantity of central importance for homogeneous suspensions of long thin rods: the orientational order tensor

$$\mathbf{S}(t) = \oint d\hat{\mathbf{u}}\,\hat{\mathbf{u}}\hat{\mathbf{u}}P(\hat{\mathbf{u}},t) , \tag{2.8}$$

which measures the orientational order. The largest eigenvalue of this tensor $\mathbf{S}$ is a measure of the degree of nematic order, while the corresponding eigenvector is "the director" of an aligned state and points in the preferred direction of the orientation of the rods.

Multiplying both sides of Eq. (2.1) by $\hat{\mathbf{u}}\hat{\mathbf{u}}$, applying Eq. (2.7) for the torque and integrating with respect to $\hat{\mathbf{u}}$, we obtain the equation of motion of the orientational order parameter tensor $\mathbf{S}$ as

$$\frac{d}{dt}\mathbf{S} = -6D_r \left\{ \mathbf{S} - \frac{1}{3}\hat{\mathbf{I}} + \frac{L}{D}\varphi(\mathbf{S}^{(4)} : \mathbf{S} - \mathbf{S} \cdot \mathbf{S}) \right\} , \tag{2.9}$$

where $\hat{\mathbf{I}}$ is the unit tensor, $\mathbf{S}^{(4)} = \langle \hat{\mathbf{u}}\hat{\mathbf{u}}\hat{\mathbf{u}}\hat{\mathbf{u}} \rangle$ is a fourth order tensor and brackets $\langle \cdots \rangle$ denote ensemble averaging. In order to make further progress we approximate [24]

$$\mathbf{S}^{(4)} : \mathbf{S} = \frac{1}{5}\left\{ 2\mathbf{S} \cdot \mathbf{S} + 3\mathbf{S}\mathbf{S} : \mathbf{S} \right\} . \tag{2.10}$$

Equation (2.9) is called the DEK equation after Doi, Edwards and Kuzuu [36, 78]. Note that in order to arrive at the DEK equation, $\bar{P}(\hat{\mathbf{u}}',t)$ in Eq. (2.7) has been put equal to the pdf $P(\hat{\mathbf{u}}',t)$ of the central rod. This means that the DEK equation applies to the dynamics of $\mathbf{S}$ of a rod floating among other rods, all having the same initial pdf as the central rod. Consequently, the DEK equation applies to the order tensor of one rod monitored during a collective decay of some collective perturbation. We therefore apply a small perturbation $\delta\mathbf{S}(t)$ to our system and write $\mathbf{S}(t)$ as

$$\mathbf{S}(t) = \mathbf{S}_0 + \delta\mathbf{S}(t) , \tag{2.11}$$

where $\mathbf{S}_0$ is the stationary solution of the equation of motion in Eq. (2.9). Linearizing Eq. (2.9) with respect to $\delta\mathbf{S}(t)$, we obtain

$$\frac{d}{dt}\delta\mathbf{S} = -6D_r^{\text{coll}}(\varphi)\delta\mathbf{S} . \tag{2.12}$$

The collective rotational diffusion coefficient $D_r^{\text{coll}}(\varphi)$ is given by

$$D_r^{\text{coll}}(\varphi) = D_r \left\{ 1 - \frac{1}{5}\frac{L}{D}\varphi \right\} . \tag{2.13}$$

As has been stressed above, $D_r^{\text{coll}}(\varphi)$ is a collective diffusion coefficient, which describes the decay of a very small perturbation of an initially isotropic state. The spinodal concentration can be found at the point where $D_r^{\text{coll}}(\varphi)$ is equal to zero.

17

2.3   Simulation method

2.3.1   Dynamics

In this section we will briefly sketch a motivation for the equations of motion on the diffusive time scale used in this Chapter, starting from the more fundamental Langevin equation on the Fokker-Planck time scale. In Appendix 2.B, we will prove that the resulting equations, Eqs. (2.27), (2.28), (2.30) and (2.31), indeed give rise to a probability distribution function evolving according to the Smoluchowski equation Eq. (2.A1).

Brownian dynamics is basically the solution of a set of Langevin equations on the Smoluchowski time scale. For very long and thin rods [88], the rotational motion around the cylindrical axis does not couple to the remaining degrees of freedom and may be neglected. Assuming that for large aspect ratios L/D and low volume fractions $L\varphi/D$ the flow field around the rods is equal to the externally applied field, the Langevin equations of motion for translation and rotation can be written as

$$\frac{d\mathbf{p}}{dt} = -\mathbf{\Xi}\cdot\mathbf{v}+\mathbf{F}_R+\mathbf{F}_S \tag{2.14}$$

$$\mathbf{v} = \frac{d\mathbf{r}}{dt} \tag{2.15}$$

$$\frac{d\mathbf{J}}{dt} = -\gamma_r\mathbf{\Omega}+\mathbf{T}_R+\mathbf{T}_S \tag{2.16}$$

$$\mathbf{\Omega} = \hat{\mathbf{u}}\times\frac{d\hat{\mathbf{u}}}{dt}\,. \tag{2.17}$$

Here $\mathbf{p}$ and $\mathbf{J}$ denote the momentum and angular momentum of some rod, $\mathbf{v}$ and $\mathbf{\Omega}$ the linear and angular velocity, and $\mathbf{F}$ and $\mathbf{T}$ denote the force and torque respectively. The subscripts R and S refer to random (caused by thermal collisions with solvent molecules) and systematic (due to the interactions between rods). In Eq. (2.14), the translational friction tensor $\mathbf{\Xi}$ is orientation dependent:

$$\mathbf{\Xi} = \gamma_\parallel\hat{\mathbf{u}}\hat{\mathbf{u}}+\gamma_\perp(\hat{\mathbf{I}}-\hat{\mathbf{u}}\hat{\mathbf{u}})\,, \tag{2.18}$$

where $\gamma_\parallel$ and $\gamma_\perp$ are the translational friction coefficients for motions parallel and perpendicular to the axis of the rod, respectively, while in Eq. (2.16), γ_r denotes the orientational friction coefficient [22, 36]. From hydrodynamics, the following expressions can be derived

for long thin rods:

$$\gamma_r \quad = \quad \frac{\pi\eta_s L^3}{3\ln(L/D)} \tag{2.19}$$

$$\gamma_\parallel \quad = \quad \frac{2\pi\eta_s L}{\ln(L/D)} \tag{2.20}$$

$$\gamma_\perp \quad = \quad 2\gamma_\parallel \,. \tag{2.21}$$

In Eqs. (2.19) and (2.20), η_s denotes the viscosity of the solvent. Finally, the random force and torque are related to the corresponding friction tensors by fluctuation-dissipation theorems,

$$\langle \mathbf{F}_R(t)\mathbf{F}_R(0)\rangle \quad = \quad 2k_B T\mathbf{\Xi}\delta(t)\,, \tag{2.22}$$

$$\langle \mathbf{T}_R(t)\mathbf{T}_R(0)\rangle \quad = \quad 2k_B T\gamma_r(\hat{\mathbf{I}}-\hat{\mathbf{u}}\hat{\mathbf{u}})\delta(t)\,, \tag{2.23}$$

where $\delta(t)$ is the Dirac delta function.

In the highly damped systems that we will study, momenta lose their memory and relax to thermal equilibrium well within a time interval Δt, which is still too short for the configuration to change appreciably. We therefore average Eq. (2.14) over time Δt while keeping $\mathbf{\Xi}$ fixed at its value at the beginning of the interval. Doing so, we arrive at

$$0 = -\mathbf{\Xi}\cdot\langle\mathbf{v}\rangle + \langle\mathbf{F}_R\rangle + \mathbf{F}_S\,, \tag{2.24}$$

which is the equation of motion on the Smoluchowski, *i.e.*, diffusive, time scale. The left-hand side is equal to zero because the average acceleration is very small compared to the individual terms on the right-hand side. $\langle\mathbf{v}\rangle$ is the average velocity, which is equal to $d\langle\mathbf{r}\rangle/dt$. Being a sum of Gaussian variables, the average random force $\langle\mathbf{F}_R\rangle$ is itself a Gaussian variable, with auto correlation function

$$\langle\langle\mathbf{F}_R(\tau\Delta t)\rangle\langle\mathbf{F}_R(0)\rangle\rangle = 2k_B T\mathbf{\Xi}\frac{\delta_{\tau,0}}{\Delta t}\,, \tag{2.25}$$

for integer τ and with δ the Kronecker delta. On the Smoluchowski time scale $\delta_{\tau,0}/\Delta t$ acts as a Dirac delta function.

Since from now on we are only interested in the dynamics at the Smoluchowski time scale, we omit the bracket indicating the time average, and simply write $\mathbf{r}$, $\mathbf{v}$ and $\mathbf{F}_R$ instead of $\langle\mathbf{r}\rangle$, $\langle\mathbf{v}\rangle$ and $\langle\mathbf{F}_R\rangle$. Equation (2.24) then reads

$$\frac{d\mathbf{r}}{dt} = \mathbf{\Xi}^{-1}\cdot(\mathbf{F}_R+\mathbf{F}_S)\,. \tag{2.26}$$

19

Assuming that the friction tensor $\boldsymbol{\Xi}$ and the systematic force $\mathbf{F}_S$ are constant over the integration time step δt, we integrate Eq. (2.26), obtaining

$$\mathbf{r}(t + \delta t) = \mathbf{r}(t) + \boldsymbol{\Xi}^{-1}(t) \cdot \mathbf{F}_S(t)\delta t + \delta \mathbf{r}(t) , \tag{2.27}$$

$$\langle \delta \mathbf{r}(t)\delta \mathbf{r}(t) \rangle = 2k_B T \boldsymbol{\Xi}^{-1}(t)\delta t . \tag{2.28}$$

The random displacement $\delta \mathbf{r}(t)$, which is contributed by the random force, is defined as

$$\delta \mathbf{r}(t) \equiv \int_0^{\delta t} d\tau \boldsymbol{\Xi}^{-1}(t + \tau) \cdot \mathbf{F}_R(t + \tau) \approx \boldsymbol{\Xi}^{-1}(t) \cdot \int_0^{\delta t} d\tau \mathbf{F}_R(t + \tau) . \tag{2.29}$$

Since $\boldsymbol{\Xi}^{-1} = \gamma_\parallel^{-1}\hat{\mathbf{u}}\hat{\mathbf{u}} + \gamma_\perp^{-1}(\hat{\mathbf{I}} - \hat{\mathbf{u}}\hat{\mathbf{u}})$ depends on the fluctuating variable $\hat{\mathbf{u}}$, the first integral in Eq. (2.29) is ambiguous and a choice has to be made to its interpretation. Since reorientations are generally much slower than displacements we have chosen to put $\boldsymbol{\Xi}^{-1}(t + \tau)$ equal to $\boldsymbol{\Xi}^{-1}(t)$, which in the mathematical literature is known as the Itô interpretation. Given this interpretation, the moments in Eq. (2.28) follow from the auto correlations in Eq. (2.25). In the simulation program, the random displacements $\delta \mathbf{r}(t)$ are calculated as follows: a random displacement with standard deviation $\sqrt{2k_B T \delta t/\gamma_\parallel}$ is applied along the cylindrical axis direction $\hat{\mathbf{u}}$, and two random displacements, each with standard deviation $\sqrt{2k_B T \delta t/\gamma_\perp}$, are applied in two mutually perpendicular directions, both perpendicular to $\hat{\mathbf{u}}$.

A similar treatment of the reorientations in the strongly damped limit leads to

$$\hat{\mathbf{u}}(t + \delta t) = \hat{\mathbf{u}}(t) + \frac{1}{\gamma_r}\mathbf{T}_S(t) \times \hat{\mathbf{u}}(t)\delta t + \delta \hat{\mathbf{u}}(t) , \tag{2.30}$$

$$\langle \delta \hat{\mathbf{u}}(t)\delta \hat{\mathbf{u}}(t) \rangle = 2k_B T \frac{1}{\gamma_r}(\hat{\mathbf{I}} - \hat{\mathbf{u}}\hat{\mathbf{u}})\delta t . \tag{2.31}$$

Again we have used the Itô interpretation to calculate the moments in Eq. (2.31). The random reorientations $\delta \hat{\mathbf{u}}(t)$ are treated in the same way as $\delta \mathbf{r}(t)$ above: two Gaussian reorientations, with standard deviation $\sqrt{2k_B T \delta t/\gamma_r}$, are applied in two mutually orthogonal directions, both perpendicular to $\hat{\mathbf{u}}$. Since this procedure will slightly change the length of $\hat{\mathbf{u}}(t)$, the latter is normalized to unity after the integration step has been applied.

Equations (2.27), (2.28), (2.30) and (2.31) constitute the equations of motion used in this Chapter. In Appendix 2.B we prove that they indeed give rise to the Smoluchowski equation Eq. (2.A1). This proof should be considered to be the decisive motivation for choosing the above equations of motion.

The simulation system in the present work was based on the experimental data of *fd* virus [88]. All simulations were run using a timestep δt of $0.05\,\mu$s. The simulation box was cubic, and contained $N = 1000L\varphi/D$ rods of diameter $D = 14.8\,$nm and length $L = 0.888\,\mu$m, hence $L/D = 60$. Water was used as the solvent, with viscosity $\eta_s = 10^{-3}\,$Pa s. The temperature was 300 K.

2.3.2 Potential

In this section, the implementation of the excluded volume interactions between rods will briefly be discussed. Excluded volume interactions are described by means of the potential

$$\Phi = k \sum_{i \neq j} V_{\text{ov}}(\mathbf{r}_i, \mathbf{r}_j, \hat{\mathbf{u}}_i, \hat{\mathbf{u}}_j) \,, \tag{2.32}$$

where the sum runs over all pairs of rods. The "hardness" k of the potential is independent of the position $\mathbf{r}$ and orientation $\hat{\mathbf{u}}$ of the rod. In our simulations, the value of this parameter k is chosen such that the pair potential equals the thermal energy $k_B T$ when the distance between two perpendicular rods equals 0.8 times their diameter. The overlap volume between rods i and j, $V_{\text{ov}}(\mathbf{r}_i, \mathbf{r}_j, \hat{\mathbf{u}}_i, \hat{\mathbf{u}}_j)$, is calculated from

$$V_{\text{ov}}(\mathbf{r}_i, \mathbf{r}_j, \hat{\mathbf{u}}_i, \hat{\mathbf{u}}_j) \;\; = \;\; V_{\text{ov}}\left(d(\mathbf{r}_i, \mathbf{r}_j, \hat{\mathbf{u}}_i, \hat{\mathbf{u}}_j), \theta(\hat{\mathbf{u}}_i, \hat{\mathbf{u}}_j)\right) \,, \tag{2.33}$$

$$V_{\text{ov}}(d, \theta) \;\; = \;\; \frac{4}{\sin\theta} \int_{\frac{-D+d}{2}}^{\frac{D-d}{2}} dp \sqrt{(\frac{D}{2})^2 - (\frac{d}{2} + p)^2} \sqrt{(\frac{D}{2})^2 - (\frac{d}{2} - p)^2} \,, \tag{2.34}$$

where d is the shortest distance between the two rods, *i.e.*, d is the projection of the center to center separation onto the direction of $\hat{\mathbf{u}}_i \times \hat{\mathbf{u}}_j$,

$$d(\mathbf{r}_i, \mathbf{r}_j, \hat{\mathbf{u}}_i, \hat{\mathbf{u}}_j) = \frac{\left|(\mathbf{r}_i - \mathbf{r}_j) \cdot (\hat{\mathbf{u}}_i \times \hat{\mathbf{u}}_j)\right|}{\left|\hat{\mathbf{u}}_i \times \hat{\mathbf{u}}_j\right|} \,, \tag{2.35}$$

and θ is the angle between the long axes of the two rods. Details can be found in Ref. 140.

Equation (2.33) is valid only for infinitely long rods. For long thin rods of finite length, the overlap volume must be calculated in a different way in cases when two rods are almost parallel, or, to be more precise, when $\sin\theta < D/L$. In this work we have set the overlap

volume in these cases equal to

$$
\begin{aligned}
V_{\mathrm{ov}}(\mathbf{r}_i,\mathbf{r}_j,\hat{\mathbf{u}}_i,\hat{\mathbf{u}}_j) &= A_{\mathrm{ov}}L_{\mathrm{ov}} \\
&= 2\left(\frac{1}{4}D^2\arccos\frac{d}{D}-\frac{d}{4}\sqrt{D^2-d^2}\right) \\
&\times \left(L-\frac{1}{2}\left(\left|(\mathbf{r}_i-\mathbf{r}_j)\cdot\hat{\mathbf{u}}_i\right|+\left|(\mathbf{r}_i-\mathbf{r}_j)\cdot\hat{\mathbf{u}}_j\right|\right)\right).
\end{aligned} \tag{2.36}
$$

Here, A_{ov} and L_{ov} denote the overlap area and the overlap length, respectively.
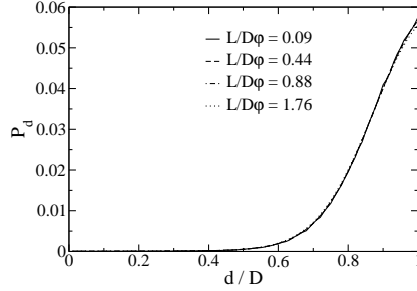

Figure 2.1: *The probability distributions $P_d(x)$ of the dimensionless closest distance x, defined as d/D, between two interacting rods at various volume fractions. There is no overlap between rods when the dimensionless closest distance x becomes larger than one.*

A consequence of using a continuous potential to describe the repulsive or excluded volume interaction between two rods is that the rods can partly overlap. The parameter D is no longer a legitimate measure of the rod's diameter. We therefore propose to use the average shortest distance, calculated according to Eq. (2.35), of two interacting, *i.e.*, overlapping, rods as an effective diameter D^{eff}. The measured probability densities $P_d(x)$ of shortest dimensionless distances x, defined as d/D, between interacting rod pairs are plotted in Fig. 2.1 for various volume fractions $L\varphi/D$. The effective diameter of the rods can be calculated according to

$$
D^{\mathrm{eff}} = D\frac{\int_0^1 dx\,P_d(x)x}{\int_0^1 dx\,P_d(x)} = 0.88\,D\,, \tag{2.37}
$$

and is independent of the density, which illustrate the hardness of the potential. The small

root-mean-square deviation

$$\sigma = \sqrt{\langle x^2 \rangle - \langle x \rangle^2} \approx 0.1 \tag{2.38}$$

confirms the impenetrability of the rods. By introducing the effective diameter, the rods become "thinner", which changes the aspect ratio $L/\mathrm{D}^{\mathrm{eff}}$ from 60 to 68. Henceforth we will use D as shorthand for $\mathrm{D}^{\mathrm{eff}}$, except of course in the calculation of V_{ov}. The volume fraction of the rod material will be calculated as if all rods have a fixed diameter equal to $\mathrm{D}^{\mathrm{eff}}$.

Given the potential Φ, the forces and torques that are needed to propagate the system are calculated according to

$$\mathbf{F}_i = -\nabla_i \Phi = -k \frac{\partial}{\partial \mathbf{r}_i} V_{\mathrm{ov}}(\mathbf{r}_i, \mathbf{r}_j, \hat{\mathbf{u}}_i, \hat{\mathbf{u}}_j) \,, \tag{2.39}$$

$$\mathbf{T}_i = -\hat{\mathscr{R}}_i \Phi = -\hat{\mathbf{u}}_i \times \frac{\partial}{\partial \hat{\mathbf{u}}_i} \Phi = -k \hat{\mathbf{u}}_i \times \frac{\partial}{\partial \hat{\mathbf{u}}_i} V_{\mathrm{ov}}(\mathbf{r}_i, \mathbf{r}_j, \hat{\mathbf{u}}_i, \hat{\mathbf{u}}_j) \,. \tag{2.40}$$

Occasionally two rods may come very close to each other, mainly as a result of the random parts in the equations of motion; the forces and torques become extremely large in these cases. In order to keep the maximum displacements and reorientations per timestep within reasonable limits, one tenth of a diameter and $2D/10L$ radians, respectively, we have restricted forces and torques to be smaller than

$$\mathbf{F}^{\mathrm{max}} \quad = \quad \frac{1}{10} \times \frac{D\gamma_\perp}{\delta t} \,, \tag{2.41}$$

$$\mathbf{T}^{\mathrm{max}} \quad = \quad \frac{1}{10} \times \frac{2D\gamma_r}{L\delta t} \,, \tag{2.42}$$

respectively. The probability densities in Fig. 2.1 used to calculate $\mathrm{D}^{\mathrm{eff}}$ were sampled from runs based on the forces and torques just described.

2.4 Result

We first performed Brownian dynamics simulations on long and thin non-interacting rods, *i.e.*, without considering excluded volume interactions between the rods. By calculating the mean square displacement [1] of the centers of mass of the rods, we confirmed that the translational diffusion coefficient obeys

$$\mathrm{D}_t = \frac{\mathrm{D}_\parallel + 2\mathrm{D}_\perp}{3} \,, \tag{2.43}$$

with $D_\parallel = k_B T / \gamma_\parallel$ and $D_\perp = k_B T / \gamma_\perp$. We measured the rotational diffusion coefficient by calculating

$$\langle P_n(\hat{\mathbf{u}}(t) \cdot \hat{\mathbf{u}}(0)) \rangle = \exp\left(-n(n+1)D_r t\right) , \tag{2.44}$$

where $P_n(x)$ is the Legendre polynomial of n-th order,

$$P_n(x) = \frac{1}{2^n n!} \frac{d^n}{dx^n} (x^2 - 1)^n , \tag{2.45}$$

and found that it agreed well with its input value (see Eqs. (2.2) and (2.19)).

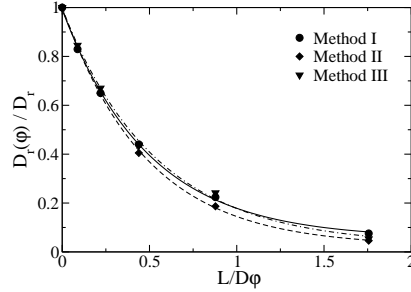### 2.4.1 Measurements of the rotational diffusion coefficient $D_r(\varphi)$

Figure 2.2: *Self rotational diffusion coefficients* $D_r(\varphi)$, *calculated by three different kinds of simulations, at various volume fractions of rods. The curves are normalized by* D_r, *the rotational diffusion coefficient of a single non-interacting rod. Method I is based on the Debye theory, Eq. (2.44), method II on the drag torque on a forceably rotated rod, Eq. (2.46), and method III on the restoring torque, Eq. (2.52).*

In semidilute and concentrated solutions the rotational motion of a typical rod is very much restricted by the rods in its direct neighborhood. This is the more true, the higher the concentration is, and as a consequence the self rotational diffusion coefficient depends on the volume fraction φ. It may still be calculated according to Eq. (2.44), but with D_r replaced by $D_r(\varphi)$. The results of these calculations are presented in Fig. 2.2, together with those of two alternative methods. The second method consists of applying a constant external torque

$\mathbf{T}_{\mathrm{ex}}$ on a chosen rod and measuring the resulting average angular velocity $\langle \boldsymbol{\Omega} \rangle$. A small extra potential was applied to restrict the motion of the rod to a plane perpendicular to $\mathbf{T}_{\mathrm{ex}}$. The rotational diffusion coefficient $\mathrm{D}_r(\varphi)$ is then obtained from the measured rotational friction coefficient according to the Einstein equation:

$$\mathbf{T}_{\mathrm{ex}} = \gamma_r(\varphi)\langle \boldsymbol{\Omega} \rangle = \frac{k_B T}{\mathrm{D}_r(\varphi)}\langle \boldsymbol{\Omega} \rangle \tag{2.46}$$

As can be seen from Fig. 2.2, the results of the two methods are in good agreement with each other, and depend strongly on the volume fraction φ.

In order to obtain reasonable estimates of the rotational diffusion coefficients for the higher volume fractions, the correlation function $\langle P_1(\hat{\mathbf{u}}(t) \cdot \hat{\mathbf{u}}(0)) \rangle = \langle \hat{\mathbf{u}}(t) \cdot \hat{\mathbf{u}}(0) \rangle$ had to be calculated for correlation times up to $t = 0.5$ s. In this subsection we present a method to obtain the same information in a much shorter time. First, take the time derivative of the correlation function $\langle \hat{\mathbf{u}}(t) \cdot \hat{\mathbf{u}}(0) \rangle$:

$$\frac{d}{dt}\langle \hat{\mathbf{u}}(t) \cdot \hat{\mathbf{u}}(0) \rangle = \oint d\hat{\mathbf{u}}\,\hat{\mathbf{u}} \cdot \hat{\mathbf{u}}(0)\frac{\partial}{\partial t}P(\hat{\mathbf{u}},t)\,, \tag{2.47}$$

where $P(\hat{\mathbf{u}},t)$ is the probability distribution function of a rod with initial distribution $P(\hat{\mathbf{u}},0) = \delta(\hat{\mathbf{u}} - \hat{\mathbf{u}}(0))$. Introducing Eq. (2.1) for the time derivative of the pdf we obtain

$$\begin{aligned}\frac{d}{dt}\langle \hat{\mathbf{u}}(t) \cdot \hat{\mathbf{u}}(0) \rangle &= \mathrm{D}_r \oint d\hat{\mathbf{u}}\,\hat{\mathbf{u}} \cdot \hat{\mathbf{u}}(0)\hat{\mathscr{R}} \cdot \hat{\mathscr{R}}P(\hat{\mathbf{u}},t)\\ &\quad - \beta\mathrm{D}_r \oint d\hat{\mathbf{u}}\,\hat{\mathbf{u}} \cdot \hat{\mathbf{u}}(0)\hat{\mathscr{R}} \cdot P(\hat{\mathbf{u}},t)\bar{\mathbf{T}}(\hat{\mathbf{u}},t)\,.\end{aligned} \tag{2.48}$$

Performing two integrations by parts in the first term and one in the second term according to [36]

$$\oint d\hat{\mathbf{u}}\,\mathbf{A}(\hat{\mathbf{u}})\hat{\mathscr{R}}\mathbf{B}(\hat{\mathbf{u}}) = -\oint d\hat{\mathbf{u}}\,[\hat{\mathscr{R}}\mathbf{A}(\hat{\mathbf{u}})]\mathbf{B}(\hat{\mathbf{u}})\,, \tag{2.49}$$

we obtain

$$\frac{d}{dt}\langle \hat{\mathbf{u}}(t) \cdot \hat{\mathbf{u}}(0) \rangle = -2\mathrm{D}_r\langle \hat{\mathbf{u}}(t) \cdot \hat{\mathbf{u}}(0) \rangle + \beta\mathrm{D}_r T_r(\hat{\mathbf{u}},t)\langle \hat{\mathbf{u}}(t) \cdot \hat{\mathbf{u}}(0) \rangle\,. \tag{2.50}$$

The second term, with

$$T_r(\hat{\mathbf{u}},t) = \frac{\langle (\hat{\mathbf{u}}(t) \times \hat{\mathbf{u}}(0)) \cdot \bar{\mathbf{T}}(\hat{\mathbf{u}},t) \rangle}{\langle \hat{\mathbf{u}}(t) \cdot \hat{\mathbf{u}}(0) \rangle}\,, \tag{2.51}$$

25

represents the contribution of the restoring torque exerted by the surrounding rods to the time evolution of $\langle \hat{\mathbf{u}}(t) \cdot \hat{\mathbf{u}}(0) \rangle$.

For long time $T_r(\hat{\mathbf{u}},t)$ becomes constant and $\langle \hat{\mathbf{u}}(t) \cdot \hat{\mathbf{u}}(0) \rangle$ diffusive. Inserting Eq. (2.44), with $n = 1$, into the left hand side of Eq. (2.50) and performing the time derivative, we obtain

$$D_r(\varphi) = \lim_{t \to \infty} D_r(\varphi,t) = \lim_{t \to \infty} D_r \{ 1 - \frac{1}{2} \beta T_r(\hat{\mathbf{u}},t) \} . \tag{2.52}$$

Repeating the same procedure, starting at Eq. (2.47), with higher values of n yields

$$D_r(\varphi) = \lim_{t \to \infty} D_r \left\{ 1 - \frac{\beta}{n(n+1)} \frac{\langle P'_n(\hat{\mathbf{u}}(t) \cdot \hat{\mathbf{u}}(0)) [(\hat{\mathbf{u}}(t) \times \hat{\mathbf{u}}(0)) \cdot \bar{\mathbf{T}}(\hat{\mathbf{u}},t)] \rangle}{\langle P_n(\hat{\mathbf{u}}(t) \cdot \hat{\mathbf{u}}(0)) \rangle} \right\} , \tag{2.53}$$
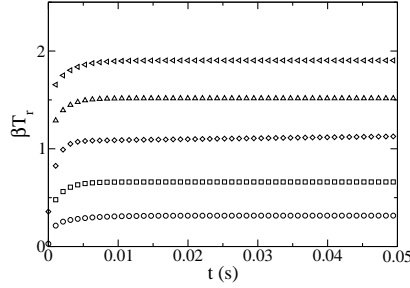
where $P'_n(x)$ is the derivative of $P_n(x)$.

Figure 2.3: *The "restoring torques" T_r shown as functions of time, see Eq. (2.51). From bottom to top, the lines correspond to $L\varphi/D = 0.09$, 0.22, 0.44, 0.88 and 1.76. In each case, a plateau value is reached in a short time.*

The results of our calculations of $\beta T_r(\hat{\mathbf{u}},t)$ are plotted in Fig. 2.3. The total time of these simulations is around $0.1 - 0.2$ s, which is considerably shorter than the traditional methods. The corresponding rotational diffusion coefficients are plotted in Fig. 2.2, referred to as method III. It is seen that all these methods give the same results within statistical errors.

Figure 2.3 reveals clearly that for all volume fractions $\beta T_r(\hat{\mathbf{u}},t)$ becomes constant within about 0.005 s. As a result, only rather short simulations are needed to calculate the rotational diffusion coefficients. Contrary to this, for the higher volume fractions $\langle \hat{\mathbf{u}}(t) \cdot \hat{\mathbf{u}}(0) \rangle$ becomes diffusive only after 0.05 s. In order to understand why this correlation takes much longer

to become diffusive than the time needed for the restoring torque to become constant, we formally solve Eq. (2.50), obtaining

$$\langle \hat{\mathbf{u}}(t) \cdot \hat{\mathbf{u}}(0) \rangle = \exp\left\{-2t\left[\frac{1}{t}\int_0^t d\tau \mathrm{D}_r(\varphi,\tau)\right]\right\}. \tag{2.54}$$

Although $T_r(\hat{\mathbf{u}},t)$, and therefore $\mathrm{D}_r(\varphi,t)$, becomes constant very quickly, it takes some extra time before the corresponding transient effects in $\frac{1}{t}\int_0^t d\tau \mathrm{D}_r(\varphi,\tau)$ have converged. In Fig. 2.4 the results of $\langle \hat{\mathbf{u}}(t) \cdot \hat{\mathbf{u}}(0) \rangle$ calculated according to Eq. (2.54) are plotted, together with those obtained directly from the simulations. Both agree well within statistical errors.
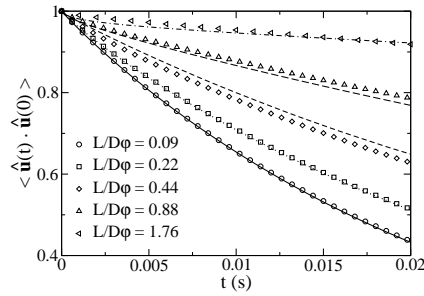

Figure 2.4: *The autocorrelation of $\hat{\mathbf{u}}$ in isotropic systems at various volume fractions, calculated directly (symbols) and from the restoring torque (lines), see Eq. (2.54).*

2.4.2 Collective orientational decay

In this subsection we will study the collective orientational decay of initially aligned, but translationally disordered, rod-like colloids. Since we are only interested in exponential decay close to the equilibrium state, see Eq. (2.12), all runs had to be extended up to the point where the order tensor elements started to fluctuate. The collective rotational diffusion coefficient defined in Eq. (2.12) was calculated for various volume fractions and is plotted in Fig. 2.5, referred to as method A. Obviously, this is not a very efficient method to obtain the quantities aimed for. For this reason, and also to have an independent check of the results, we have resorted to Onsager's regression hypothesis [12, 15] to write

$$\langle \delta \mathbf{S}(t) \delta \mathbf{S}(0) \rangle = \langle \delta \mathbf{S}(0) \delta \mathbf{S}(0) \rangle \exp\{-6\mathrm{D}_r^{\mathrm{coll}}(\varphi)t\}, \tag{2.55}$$
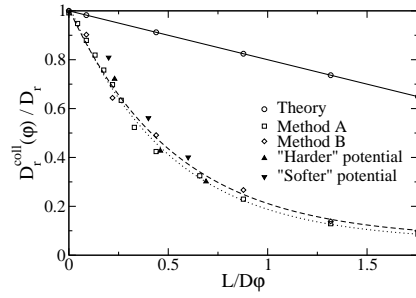
27

Figure 2.5: *The collective rotational diffusion coefficient* $D_r^{coll}(\varphi)$ *at various volume fractions. In method A, an initially fully aligned system is decaying to the isotropic state, while method B uses Onsager's regression hypothesis to analyze equilibrium fluctuations. The dashed and dotted lines are fits to these methods. The value of the potential parameter k for the "harder" and "softer" simulations (both using method A) are twice and half the standard value, respectively. The straight line is the prediction by the theory of Dhont and Briels, and D_r is the rotational diffusion coefficient of a single non-interacting rod.*

where the brackets indicate averages in the equilibrium state. The results of these calculations are also plotted in Fig. 2.5, referred to as method B. The results of both methods agree very well with each other but deviate considerably from the theoretical prediction of Dhont and Briels given in Eq. (2.13). Moreover, they are almost equal to the corresponding self rotational diffusion coefficients $D_r(\varphi)$ discussed in section 2.4.1.

In order to test if our potential $\Phi = V_{ov}$ given in Eq. (2.32) is sufficiently hard, we have performed additional simulations with somewhat different potentials. The results of runs with double and half the original hardness parameter k are included in Fig. 2.5, denoted as "harder" and "softer", respectively. It turns out that the harder potential yields the same results as our original potential, indicating that the latter is most probably hard enough to represent hard colloids.

As already mentioned above, the simulation results of the collective rotational diffusion coefficients differ markedly from the theoretical predictions of Dhont and Briels based on DEK theory. As was shown by these authors, several approximations are used to arrive at the DEK equations. First, the time dependence of $g(\mathbf{r} - \mathbf{r}', \hat{\mathbf{u}}, \hat{\mathbf{u}}', t)$ is neglected by putting it equal
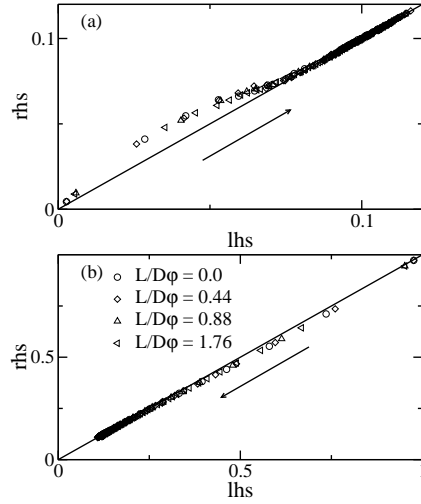
Figure 2.6: *Validation of the approximation made in the doubly contracted form of* $\mathbf{S}^{(4)} : \mathbf{S}$, *see Eq. (2.10). For the xx (a) and yy (b) component of this contraction, the approximate right-hand side is plotted against the exact left-hand side. The analyzed configurations are extracted from nonequilibrium simulations, decaying from fully aligned to isotropic, with arrows indicating the evolution in time. The approximations are seen to hold very well for the isotropic system.*

to its equilibrium value, which to a very good approximation is given by the Onsager formula Eq. (2.4). Next, $\left| \hat{\mathbf{u}} \times \hat{\mathbf{u}}' \right|$ occurring in the torque is approximated by a Landau-Ginzburg expansion. Finally, contractions of the fourth order tensor $\mathbf{S}^{(4)}$ are calculated by means of closure relations like the one in Eq. (2.10). Let us start our discussion with the last of these possible shortcomings of the theory. In order to check the quality of Eq. (2.10), we have calculated both sides directly from the simulations during four typical runs and plotted them in Fig. 2.6. It is seen that the closure approximation performs very well for all values of the order parameter. Next we turn our attention to the Landau-Ginzburg expansion. From Eq. (2.5), *i.e.*, right after the neglect of dynamic correlations, it is obvious that the average torque and, therefore, the equation of motion of the order tensor $\mathbf{S}$ are linear in $L\varphi/D$, although they may be highly nonlinear in $\mathbf{S}$. Since, in order to calculate the decay of $\delta\mathbf{S}$ close to equilibrium, we linearize the equation of motion of $\mathbf{S}$ in any case, we obtain a linear depen-

dence of $D_r^{coll}(\varphi)$ on $L\varphi/D$ irrespective of how exactly the average torque is approximated. This leaves us with the neglect of dynamic correlations as the only possible cause of the difference between theory and simulations. Notice that both in the theory and in the simulations hydrodynamic interactions were neglected, and that these therefore cannot be the cause of the large deviations between theory and simulations.

Finally, let us return to the fact that the collective rotational diffusion coefficients are virtually equal to the self rotational diffusion coefficients. Obviously this tells us that the average decay of different rods is hardly correlated, if at all. In Appendix 2.C we prove that under this condition,

$$\langle \delta S_{ii}(t)\delta S_{ii}(0)\rangle = \langle \delta S_{ii}(0)\delta S_{ii}(0)\rangle \langle P_2(\hat{\mathbf{u}}(t)\cdot\hat{\mathbf{u}}(0))\rangle \ . \tag{2.56}$$

Together with $\langle P_2(\hat{\mathbf{u}}(t)\cdot\hat{\mathbf{u}}(0))\rangle = \exp\{-6D_r(\varphi)t\}$, this proves that under these assumptions $D_r^{coll}(\varphi) = D_r(\varphi)$.

2.5 Conclusion

A Brownian dynamics simulation program has been written to investigate the diffusion properties of rigid long thin rod-like colloids. This program is based on the solution of the Langevin equations of motion on the Smoluchowski time scale. Hard core interactions are taken into account by means of a pairwise additive potential, with each pair contributing proportional to the overlap of the corresponding rods. Hydrodynamic interactions between different rods are neglected. Self and collective rotational diffusion coefficients were calculated from isotropic equilibrium simulations as well as from nonequilibrium simulations of initially fully aligned systems. The results of the present Chapter can be summarized as follows:

1. A new method for calculating the self rotational diffusion coefficient $D_r(\varphi)$ is proposed, by exploiting the restoring torque on a rod by its surrounding rods. The simulation results based on this much quicker technique agree very well with those calculated from two traditional time-consuming approaches, at various volume fractions $L\varphi/D$.

2. The measured collective rotational diffusion coefficients $D_r^{coll}(\varphi)$ show large deviations from the theoretical prediction of Dhont and Briels, for both equilibrium and nonequi-

librium Brownian dynamics simulations. This is attributed to the neglect of dynamical correlations in the theory.

3. The simulations indicate that the self rotational diffusion coefficients $D_r(\varphi)$ and the collective rotational diffusion coefficients $D_r^{\text{coll}}(\varphi)$ are virtually identical for the systems studied here. A theoretical investigation corroborates this observation and the conditions for which it is expected to hold true.

The insights gained from the simulations in the importance of the dynamical correlation between rods are a valuable asset to guide future improvements of the theory on the dynamics of long thin rigid rods. Further algorithmic improvements are needed to extend the current simulations to higher volume fractions, in order to study the dynamics of liquid crystal-like phase transitions, which are computationally too demanding for the current program.

Appendix 2.A: Derivation of Eq. (2.1) from the N-particle Smoluchowski equation

The N-particle Smoluchowski equation is the equation of motion for the probability density function P of the positions $\{\mathbf{r}_1, \cdots, \mathbf{r}_N\}$ and orientations $\{\hat{\mathbf{u}}_1, \cdots, \hat{\mathbf{u}}_N\}$ of the N rigid rods in the system under consideration. This equation reads [22, 40, 72]

$$\frac{\partial P}{\partial t} = \sum_{j=1}^{N} \left\{ \tfrac{3}{4} D_t \nabla_j \cdot \left(\hat{\mathbf{I}} + \hat{\mathbf{u}}_j \hat{\mathbf{u}}_j \right) \cdot [\nabla_j P + \beta P \nabla_j \Phi] + D_r \hat{\mathscr{R}}_j \cdot \left[\hat{\mathscr{R}}_j P + \beta P \hat{\mathscr{R}}_j \Phi \right] \right\} , \quad (2.\text{A1})$$

where D_t and D_r are the translational and rotational diffusion coefficients of a free, non-interacting rod, and Φ is the total interaction energy of the assembly of N rods. The general form for the diffusion tensor of uniaxial rods is $k_B T \mathbf{\Xi}^{-1} = D_{\parallel} \hat{\mathbf{I}} + \Delta D(\hat{\mathbf{u}}\hat{\mathbf{u}} - \hat{\mathbf{I}})$, where $\Delta D = D_{\parallel} - D_{\perp}$, with $D_{\parallel}$ and $D_{\perp}$ the inverse friction coefficients for motion parallel and perpendicular to the long axis, respectively. For very long and thin rods, $D_{\parallel} = 2D_{\perp}$, in which case the above general expression reduces to $\tfrac{3}{4} D_t \left[\hat{\mathbf{I}} + \hat{\mathbf{u}}\hat{\mathbf{u}} \right]$, with $D_t = \tfrac{1}{3}(D_{\parallel} + 2D_{\perp})$. This expression for the translational diffusion tensor has been used in the first term in (2.A1). Hydrodynamic interactions between the rods are neglected in the above equation.

Analytical progress can be made by assuming a pair-wise additive total potential, that is,

$$\Phi(\mathbf{r}_1, \cdots, \mathbf{r}_N, \hat{\mathbf{u}}_1, \cdots, \hat{\mathbf{u}}_N) = \sum_{i<j} V(\mathbf{r}_i - \mathbf{r}_j, \hat{\mathbf{u}}_i, \hat{\mathbf{u}}_j), \tag{2.A2}$$

with V the pair-interaction potential. This is exact for the rods with hard-core interactions considered here. According to the integral theorems of Gauss and Stokes, we have, respectively,

$$\int d\mathbf{r}_j \nabla_j \cdot (\cdots) = 0 \quad \text{and} \quad \oint d\hat{\mathbf{u}}_j \hat{\mathscr{R}}_j \cdot (\cdots) = 0. \tag{2.A3}$$

Using these relations, and noting that

$$P(\hat{\mathbf{u}}_1, t) = \int d\mathbf{r}_1 \cdots \int d\mathbf{r}_N \oint d\hat{\mathbf{u}}_2 \cdots \oint d\hat{\mathbf{u}}_N \, P(\mathbf{r}_1, \cdots, \mathbf{r}_N, \hat{\mathbf{u}}_1, \hat{\mathbf{u}}_2, \cdots, \hat{\mathbf{u}}_N, t), \tag{2.A4}$$

the integration of both sides of the Smoluchowski equation with respect to $\mathbf{r}_1, \cdots, \mathbf{r}_N$ and $\hat{\mathbf{u}}_2, \cdots, \hat{\mathbf{u}}_N$ leads to Eqs. (2.1) and (2.3) (with $\hat{\mathbf{u}} = \hat{\mathbf{u}}_1$, $\hat{\mathbf{u}}' = \hat{\mathbf{u}}_2$, $\mathbf{r} = \mathbf{r}_1$ and $\mathbf{r}' = \mathbf{r}_2$), where the pair-correlation function g is defined as

$$
\begin{aligned}
P(\mathbf{r}, \mathbf{r}', \hat{\mathbf{u}}, \hat{\mathbf{u}}', t) &\equiv \int d\mathbf{r}_3 \cdots \int d\mathbf{r}_N \oint d\hat{\mathbf{u}}_3 \cdots \oint d\hat{\mathbf{u}}_N P(\mathbf{r}, \mathbf{r}', \mathbf{r}_3, \cdots, \mathbf{r}_N, \hat{\mathbf{u}}, \hat{\mathbf{u}}', \hat{\mathbf{u}}_3, \cdots, \hat{\mathbf{u}}_N, t) \\
&\equiv \frac{1}{V^2} P(\hat{\mathbf{u}}, t) \bar{P}(\hat{\mathbf{u}}', t) g(\mathbf{r} - \mathbf{r}', \hat{\mathbf{u}}, \hat{\mathbf{u}}', t),
\end{aligned}
\tag{2.A5}
$$

with $P(\mathbf{r}, \mathbf{r}', \hat{\mathbf{u}}, \hat{\mathbf{u}}', t)$ the pdf for the positions and orientations of two rods and V the volume. The two one-particle pdf's have been assumed to possibly differ. This point is further discussed in section 2.2.

Appendix 2.B: Equivalence of Brownian dynamics equations of motion and the Smoluchowski equation

In this appendix we will briefly sketch the proof of the equivalence of the equations of motion used in this Chapter, Eqs. (2.27), (2.28), (2.30) and (2.31), and the Smoluchowski equation Eq. (2.A1). Although the general approach in this Appendix is fairly standard [13, 51, 136], some of the technical details are a bit intricate. We will closely follow Appendix IV.C in Ref. 13.

From the equations of motion it is obvious that our system is Markovian. Therefore the pdf $P = P(z, z_0; t)$ with $z = \{z_1, \cdots, z_N\}$ and $z_i = \{\mathbf{r}_i, \hat{\mathbf{u}}_i\}$ satisfies the Chapman-Kolmogorov

equation

$$P(z', z_0; t + \delta t) = \int dz \, P(z', z; \delta t) P(z, z_0; t) \,. \tag{2.B1}$$

We explicitly mention the initial value z_0 of z to clarify the meaning of the Chapman-Kolmogorov equation. Since we are interested in the limit of $\delta t \to 0$, in which case $P(z', z; \delta t)$ approaches a Dirac delta distribution, and we prefer not to make a Taylor-expansion of the latter, we multiply the Chapman-Kolmogorov equation by $F(z')$ and integrate, obtaining

$$\int dz \, P(z, z_0; t + \delta t) F(z) = \int dz \left[\int dz' \, P(z', z; \delta t) F(z') \right] P(z, z_0; t) \,. \tag{2.B2}$$

In the integral between the square brackets on the right-hand side we may now safely expand $F(z')$ around $z' = z$, writing

$$F(z') = F(z) + (z' - z) \cdot \nabla_z F(z) + \frac{1}{2} (z' - z)(z' - z) : \nabla_z \nabla_z F(z) + \cdots \tag{2.B3}$$

It will turn out that all terms of order higher than two do not contribute to the final result. Performing the integral we find

$$\int dz' \, P(z, z'; \delta t) F(z') = F(z) + \langle \Delta z; \delta t \rangle \cdot \nabla_z F(z) + \frac{1}{2} \langle \Delta z \Delta z; \delta t \rangle : \nabla_z \nabla_z F(z) \tag{2.B4}$$

with moments defined by

$$\langle \Delta z; \delta t \rangle = \int dz' \, (z' - z) P(z', z; \delta t) \,, \tag{2.B5}$$

$$\langle \Delta z \Delta z; \delta t \rangle = \int dz' \, (z' - z)(z' - z) P(z', z; \delta t) \,. \tag{2.B6}$$

Although the second order moments contribute a $5N \times 5N$ matrix, only those elements which are of first order in δt contribute to the final result. Since elements corresponding to two different particles are of order $(\delta t)^2$, we may restrict our attention to just one particle and write in more detail

$$
\begin{aligned}
\langle \delta z; \delta t \rangle \cdot \nabla_z F(z) \quad + \quad & \frac{1}{2} \langle \Delta z \Delta z; \delta t \rangle : \nabla_z \nabla_z F(z) \\
= \quad & \langle \Delta \mathbf{r}; \delta t \rangle \cdot \nabla F(z) + \langle \Delta \hat{\mathbf{u}}; \delta t \rangle \cdot (\hat{\mathbf{I}} - \hat{\mathbf{u}}\hat{\mathbf{u}}) \cdot \nabla_{\hat{\mathbf{u}}} F(z) \\
+ \quad & \frac{1}{2} \langle \Delta \mathbf{r} \Delta \mathbf{r}; \delta t \rangle : \nabla \nabla F(z) \\
+ \quad & \frac{1}{2} \langle \Delta \hat{\mathbf{u}} \Delta \hat{\mathbf{u}}; \delta t \rangle : (\hat{\mathbf{I}} - \hat{\mathbf{u}}\hat{\mathbf{u}}) \cdot \nabla_{\hat{\mathbf{u}}} (\hat{\mathbf{I}} - \hat{\mathbf{u}}\hat{\mathbf{u}}) \cdot \nabla_{\hat{\mathbf{u}}} F(z) \,, \tag{2.B7}
\end{aligned}
$$

where ∇ is the gradient with respect to $\mathbf{r}$ and $\nabla_{\hat{\mathbf{u}}}$ the derivative with respect to $\hat{\mathbf{u}}$. In the Itô interpretation of the stochastic integrals Eqs. (2.28) and (2.31), mixed second order moments of translational and rotational displacements are uncorrelated and therefore of second order in δt. The remaining moments are

$$
\begin{aligned}
\langle \Delta \mathbf{r}; \delta t \rangle &= -\boldsymbol{\Xi}^{-1}(t) \cdot \nabla \Phi(t) \delta t \,, \\
\langle \Delta \hat{\mathbf{u}}; \delta t \rangle &= \frac{1}{\gamma_r} \hat{\mathbf{u}}(t) \times \hat{\mathscr{R}} \Phi(t) \delta t \,, \\
\langle \Delta \mathbf{r} \Delta \mathbf{r}; \delta t \rangle &= 2 k_B T \boldsymbol{\Xi}^{-1}(t) \delta t \,, \\
\langle \Delta \hat{\mathbf{u}} \Delta \hat{\mathbf{u}}; \delta t \rangle &= 2 k_B T \frac{1}{\gamma_r} (\hat{\mathbf{I}} - \hat{\mathbf{u}}(t)\hat{\mathbf{u}}(t)) \delta t \,.
\end{aligned}
\tag{2.B8}
$$

where we have used Eqs. (2.27), (2.28), (2.30), (2.31), (2.39) and (2.40). Introducing these moments into Eq. (2.B7), using $(\hat{\mathbf{I}} - \hat{\mathbf{u}}\hat{\mathbf{u}}) \cdot \nabla_{\hat{\mathbf{u}}} = -\hat{\mathbf{u}} \times \hat{\mathscr{R}}$, $(\hat{\mathbf{u}} \times (\hat{\mathscr{R}}\Phi)) \cdot (\hat{\mathbf{u}} \times \hat{\mathscr{R}}) = (\hat{\mathscr{R}}\Phi) \cdot \hat{\mathscr{R}}$ and $(\hat{\mathbf{I}} - \hat{\mathbf{u}}\hat{\mathbf{u}}) : (\hat{\mathbf{u}} \times \hat{\mathscr{R}})(\hat{\mathbf{u}} \times \hat{\mathscr{R}}) = (\hat{\mathbf{u}} \times \hat{\mathscr{R}}) \cdot (\hat{\mathbf{u}} \times \hat{\mathscr{R}}) = \hat{\mathscr{R}} \cdot \hat{\mathscr{R}}$, we obtain:

$$
\begin{aligned}
\langle \Delta z; \delta t \rangle \cdot \nabla_z F(z) \quad &+ \quad \frac{1}{2} \langle \Delta z \Delta z; \delta t \rangle : \nabla_z \nabla_z F(z) \\
&= \quad -(\boldsymbol{\Xi}^{-1} \cdot \nabla \Phi) \cdot \nabla F(z) \delta t - \gamma_r^{-1}(\hat{\mathscr{R}}\Phi) \cdot \hat{\mathscr{R}} F(z) \delta t \\
&+ \quad k_B T \boldsymbol{\Xi}^{-1} : \nabla\nabla F(z) \delta t + k_B T \gamma_r^{-1} \hat{\mathscr{R}} \cdot \hat{\mathscr{R}} F(z) \delta t \,.
\end{aligned}
\tag{2.B9}
$$

We finally combine Eqs. (2.B2), (2.B4) and (2.B9) and perform some partial integrations according to [24]

$$
\begin{aligned}
\int d^3\mathbf{r} \, \mathbf{A}(\mathbf{r}) \cdot \nabla F(z) &= - \int d^3\mathbf{r} \, (\nabla \cdot \mathbf{A}(\mathbf{r})) F(z) \,, \\
\oint d\hat{\mathbf{u}} \, \mathbf{A}(\hat{\mathbf{u}}) \cdot \hat{\mathscr{R}} F(z) &= - \oint d\hat{\mathbf{u}} \, (\hat{\mathscr{R}} \cdot \mathbf{A}(\hat{\mathbf{u}})) F(z) \,,
\end{aligned}
\tag{2.B10}
$$

obtaining in the limit of $\delta t \to 0$:

$$
\begin{aligned}
\int dz \, \frac{\partial}{\partial t} P(z, z_0; t) F(z) &= \int dz \, \{ \nabla \cdot \boldsymbol{\Xi}^{-1} \cdot (\nabla\Phi) P(z, z_0; t) + \gamma_r^{-1} \hat{\mathscr{R}} \cdot (\hat{\mathscr{R}}\Phi) P(z, z_0; t) \\
&+ \quad k_B T \nabla\nabla : \boldsymbol{\Xi}^{-1} P(z, z_0; t) + k_B T \gamma_r^{-1} \hat{\mathscr{R}} \cdot \hat{\mathscr{R}} P(z, z_0; t) \} F(z) \,.
\end{aligned}
\tag{2.B11}
$$

Since $F(z)$ is completely general, $\partial/\partial t \, P(z, z_0; t)$ must be equal to the sum between curly brackets on the right-hand side. Summing over all particles on the right hand side and using $\nabla\nabla : \boldsymbol{\Xi}^{-1} P = \nabla \cdot \boldsymbol{\Xi}^{-1} \cdot \nabla P$, we obtain the Smoluchowski equation Eq. (2.A1). The reader will have no difficulties to justify the unproven claims made in the course of the derivation.

Appendix 2.C: Derivation of Eq. (2.56) with approximations of time correlation function

For a homogeneous isotropic equilibrium system the time correlation functions of the spontaneous fluctuations of the orientational order parameter tensor $\langle \delta \mathbf{S}(t) \delta \mathbf{S}(0) \rangle$ are given by

$$\langle \delta S_{yy}(t) \delta S_{yy}(0) \rangle = \frac{1}{N^2} \sum_n \sum_m \left\langle \left(u_{yn}(t) u_{yn}(t) - \frac{1}{3} \right) \left(u_{ym}(0) u_{ym}(0) - \frac{1}{3} \right) \right\rangle , \quad (2.C1)$$

where we have chosen the yy component for convenience. Rewriting Eq. (2.C1) leads to

$$\langle \delta S_{yy}(t) \delta S_{yy}(0) \rangle = -\frac{1}{9} + \frac{1}{N^2} \sum_n \langle u_{yn}(t) u_{yn}(t) u_{yn}(0) u_{yn}(0) \rangle$$

$$+ \frac{1}{N^2} \sum_n \sum_{\neq m} \langle u_{yn}(t) u_{yn}(t) u_{ym}(0) u_{ym}(0) \rangle . \quad (2.C2)$$

Assuming that correlations of $u_y(t)$ for different rods can be neglected, *i.e.*,

$$\sum_n \sum_{\neq m} \langle u_{yn}(t) u_{yn}(t) u_{ym}(0) u_{ym}(0) \rangle = \sum_n \sum_{\neq m} \langle u_{yn}(t) u_{yn}(t) \rangle \langle u_{ym}(0) u_{ym}(0) \rangle , \quad (2.C3)$$

the right-hand side of Eq. (2.C2) results in

$$-\frac{1}{9} + \frac{1}{N^2} \sum_n \sum_m \langle u_{yn}(t) u_{yn}(t) \rangle \langle u_{ym}(0) u_{ym}(0) \rangle$$

$$+ \frac{1}{N^2} \sum_n \left\{ \langle u_{yn}(t) u_{yn}(t) u_{yn}(0) u_{yn}(0) \rangle - \langle u_{yn}(t) u_{yn}(t) \rangle \langle u_{yn}(0) u_{yn}(0) \rangle \right\} \quad (2.C4)$$

Thus,

$$\langle \delta S_{yy}(t) \delta S_{yy}(0) \rangle = \frac{1}{N^2} \sum_n \left\{ \left\langle (u_{yn}(t) u_{yn}(0))^2 \right\rangle - \frac{1}{9} \right\} . \quad (2.C5)$$

In the isotropic state, the time correlation functions for x, y and z components are identical,

$$\sum_n \left\langle (u_{yn}(t) u_{yn}(0))^2 \right\rangle = \frac{1}{3} \sum_n \left[\left\langle (u_{xn}(t) u_{xn}(0))^2 \right\rangle + \left\langle (u_{yn}(t) u_{yn}(0))^2 \right\rangle + \left\langle (u_{zn}(t) u_{zn}(0))^2 \right\rangle \right]$$

$$(2.C6)$$

Assuming that the off-diagonal correlations of the one-particle orientational order parameter tensor decay extremely fast, *i.e.*, $\langle S_{ii}(t) S_{jj}(0) \rangle \sim 0$, we obtain

$$\sum_n \left\langle (u_{yn}(t) u_{yn}(0))^2 \right\rangle \approx \frac{1}{3} \sum_n \left\langle (u_{xn}(t) u_{xn}(0) + u_{yn}(t) u_{yn}(0) + u_{zn}(t) u_{zn}(0))^2 \right\rangle . \quad (2.C7)$$

Finally, Eq. (2.C1) results in

$$\left\langle \delta S_{yy}(t) \delta S_{yy}(0) \right\rangle \approx \frac{2}{9} \frac{1}{N^2} \sum_n \left\langle \frac{3}{2} \left(\hat{\mathbf{u}}_n(t) \cdot \hat{\mathbf{u}}_n(0) \right)^2 - \frac{1}{2} \right\rangle . \qquad (2.C8)$$

Apart from a constant factor, this is nothing but $\langle P_2(\hat{\mathbf{u}}(t) \cdot \hat{\mathbf{u}}(0)) \rangle$.

Isotropic-nematic spinodals of rigid long thin rod-like colloids by event-driven Brownian dynamics simulations

3

The isotropic-nematic spinodals of solutions of rigid spherocylindrical colloids with various shape anisotropies L/D in a wide range from 10 to 60 are investigated by means of Brownian dynamics simulations. To make these simulations feasible, we developed a new event-driven algorithm that takes the excluded volume interactions between particles into account as instantaneous collisions, but neglects the hydrodynamic interactions. This algorithm is applied to dense systems of highly elongated rods, and proves to be efficient. The calculated isotropic-nematic spinodals lie between the previously established binodals in the phase diagram and extrapolate for infinitely long rods to Onsager's theoretical predictions. Moreover, we investigate the shear induced shifts of the spinodals, qualitatively confirming the theoretical prediction of the critical shear rate at which the two spinodals merge and the isotropic-nematic phase transition ceases to exist. *

3.1 Introduction

Solutions of long and thin rigid rods interacting by excluded volume interactions, such as elongated colloidal particles and *fd* viruses [88, 90, 92], exhibit lyotropic liquid crystalline phase behavior. At low concentrations the rods form a disordered isotropic phase, while at higher concentrations the interactions cause the rods to align along a director in a nematic

---

phase. This phase still lacks translational order, which will appear at even higher concentrations. Upon increasing the rod number density, an isotropic solution will become thermodynamically unstable if the concentration crosses the isotropic-nematic spinodal (INS). Conversely, a nematic phase disorders into an isotropic state if the concentration is reduced below the nematic-isotropic spinodal (NIS). Outside these spinodals lie two binodals, *i.e.*, the concentrations at which the coexisting isotropic and nematic phases of a phase separated system are in thermal equilibrium. In the 1940s, Onsager [114] derived expressions for the spinodals and binodals of solutions of hard rods with infinite aspect ratios. The phase diagram of lyotropic rod-like systems has since been investigated extensively using theory [27, 50, 71, 85, 87, 123, 124, 125, 126, 127, 137, 138], experiments [30, 32], and more recently by computer simulations [10, 11, 52]. For a review, we refer the reader to Vroege and Lekkerkerker [139].

Our objective is to establish the spinodals of a solution of hard spherocylinders as a function of the aspect ratio of the rods. To this effect, we employ computer simulations to study the stability and dynamics of homogeneous ordered and disordered solutions in the vicinity of the spinodal concentrations. The dynamics of solvated rods is best simulated using Brownian dynamics (BD). At the high aspect ratios we are interested in, the hydrodynamic interactions between rods are less important [24] than the excluded volume interactions, which are readily incorporated by means of a potential based on the overlap area. Since incorporating hydrodynamic interactions leads to complicated and slow programs, but does not affect the location of the spinodals, we here prefer a simpler and more approximate approach, leaving for future work the assessment of the importance of hydrodynamic interactions on the dynamics. Although recent studies [19, 133] of the self and collective rotational dynamics of rods show that this method works well for dilute systems, it unfortunately turns out that the interaction potentials cause unsurmountable difficulties when performing prolonged simulations of the dense and highly elongated rods needed for a stable nematic phase. We therefore introduce here an event-driven Brownian dynamics algorithm, combining the dynamics equations of traditional fixed time step BD with the collision-based time step commonly used in simulations of hard bodies. The resulting algorithm proves efficient at simulating concentrated solutions of rods, and displays a stable nematic phase for elongated rods. The notoriously slow process of spontaneous ordering of an isotropic system above the INS takes between a

week and a month on a desktop personal computer for the densities and high aspect ratios employed here.

Having direct access to the dynamics of the rods also allows us to investigate the effect of shear flow on the phase diagram. Under shear the rods have a propensity to align along the flow direction, both in the isotropic and in the nematic phase, thus decreasing the spinodal concentrations [23, 24, 25, 26, 111, 112, 119, 122]. At sufficiently high shear rates the spinodals are predicted to terminate at a coalescence point, eliminating the phase transition between ordered and disordered states.

This Chapter is organized as follows: The event-driven Brownian dynamics algorithm is described in detail in the next section, followed by a validation against a traditional BD program at the dilute and semidilute concentrations accessible to the latter. In section 3.3.1 we investigate the density dependence of the self and collective rotational diffusion coefficients. The spinodals as functions of the aspect ratio are presented in section 3.3.2, and in section 3.3.3, we briefly discuss the shear-induced shift of the spinodals. Finally, we summarize our conclusions in section 3.4.

3.2 Simulation method

3.2.1 Event-driven algorithm

In this section we briefly describe the algorithm employed in event-driven Brownian dynamics simulations. The Brownian particles, in this case rigid long and thin colloids, are suspended in a Newtonian liquid with a stationary simple shear velocity field $\mathbf{V}$

$$\mathbf{V}(\mathbf{r}) = \boldsymbol{\Gamma} \cdot \mathbf{r} \, , \tag{3.1}$$

with

$$\boldsymbol{\Gamma} = \dot{\gamma}\hat{\boldsymbol{\Gamma}} \quad \text{and} \quad \hat{\boldsymbol{\Gamma}} = \begin{pmatrix} 0 & 1 & 0 \\ 0 & 0 & 0 \\ 0 & 0 & 0 \end{pmatrix} \, . \tag{3.2}$$

Here $\mathbf{r}$ is a position, $\dot{\gamma}$ is the shear rate and $\boldsymbol{\Gamma}$ is the transposed velocity gradient tensor. This velocity field corresponds to a flow in the *x*-direction, with a gradient in the *y*-direction.

39

The forces and torques acting on the Brownian particles have three origins: potential, friction and random. The first is due to the excluded volume interactions between solute particles; the second is caused by the velocity and angular velocity of the particle relative to the flow field; the last one is due to thermal collisions between particles and solvent molecules. For a very long and thin rod, due to its symmetry, the rotational motion around the cylindrical axis does not couple to the remaining degrees of freedom and may be neglected. Generally, the Brownian motion of particles can be described, on the Smoluchowski or diffusive time scale, by stochastic differential equations (SDEs), also known as Langevin equations. For our long thin rods in a shear flow, these equations are

$$\mathbf{r}(t + \delta t) = \mathbf{r}(t) + \mathbf{\Gamma} \cdot \mathbf{r}(t) \, \delta t + \mathbf{\Xi}^{-1}(t) \cdot \mathbf{F}_S(t) \, \delta t + \delta \mathbf{r}(t) \,, \tag{3.3}$$

$$\hat{\mathbf{u}}(t + \delta t) = \hat{\mathbf{u}}(t) + [\hat{\mathbf{I}} - \hat{\mathbf{u}}(t)\hat{\mathbf{u}}(t)] \cdot \mathbf{\Gamma} \cdot \hat{\mathbf{u}}(t) \delta t + \frac{1}{\gamma_r} \mathbf{T}_S(t) \times \hat{\mathbf{u}}(t) \delta t + \delta \hat{\mathbf{u}}(t) \,. \tag{3.4}$$

Here, $\mathbf{r}$ represents the center of mass position of a rod, $\hat{\mathbf{u}}$ is a unit vector along the axial direction of the rod, $\mathbf{F}_S$ and $\mathbf{T}_S$ denote the systematic force and torque, respectively, $\hat{\mathbf{I}}$ is the unit tensor and δt is the timestep used in the simulations. In Eq. (3.3), the translational friction tensor $\mathbf{\Xi}$ is orientation dependent:

$$\mathbf{\Xi} = \gamma_{\parallel} \hat{\mathbf{u}}\hat{\mathbf{u}} + \gamma_{\perp}(\hat{\mathbf{I}} - \hat{\mathbf{u}}\hat{\mathbf{u}}) \,, \tag{3.5}$$

where $\gamma_{\parallel}$ and $\gamma_{\perp}$ are the translational friction coefficients for motions parallel and perpendicular to the axis of the rod, respectively, while in Eq. (3.4) γ_r denotes the rotational friction coefficient [22, 36]. From hydrodynamics, the following expressions can be derived for long and thin rods of length L and diameter D:

$$\gamma_r = \frac{\pi \eta_s L^3}{3\ln(L/D)} \,, \tag{3.6}$$

$$\gamma_{\parallel} = \frac{2\pi \eta_s L}{\ln(L/D)} \,, \tag{3.7}$$

$$\gamma_{\perp} = 2\gamma_{\parallel} \,, \tag{3.8}$$

where η_s denotes the viscosity of the solvent. The random displacement and reorientation $\delta \mathbf{r}(t)$ and $\delta \hat{\mathbf{u}}(t)$, respectively, are sampled from Gaussian distributions with zero mean and variances

$$\langle \delta \mathbf{r}(t) \delta \mathbf{r}(t) \rangle = 2k_B T \mathbf{\Xi}^{-1}(t) \delta t \,, \tag{3.9}$$

$$\langle \delta \hat{\mathbf{u}}(t) \delta \hat{\mathbf{u}}(t) \rangle = 2k_B T \frac{1}{\gamma_r} (\hat{\mathbf{I}} - \hat{\mathbf{u}}\hat{\mathbf{u}}) \delta t \,, \tag{3.10}$$

with $k_B T$ as the thermal energy. The brackets indicate canonical ensemble averages. In the computer program, $\delta \mathbf{r}(t)$ and $\delta \hat{\mathbf{u}}(t)$ are treated in the same way as mentioned in our previous paper [133]:

$$
\delta \mathbf{r}(t) = G_1 \sqrt{\frac{2k_B T \delta t}{\gamma_\parallel}} \hat{\mathbf{u}} + G_2 \sqrt{\frac{2k_B T \delta t}{\gamma_\perp}} \frac{\hat{\mathbf{u}} \times \hat{\mathbf{e}}_x}{|\hat{\mathbf{u}} \times \hat{\mathbf{e}}_x|}
$$
$$
+ G_3 \sqrt{\frac{2k_B T \delta t}{\gamma_\perp}} \frac{\hat{\mathbf{u}} \times (\hat{\mathbf{u}} \times \hat{\mathbf{e}}_x)}{|\hat{\mathbf{u}} \times (\hat{\mathbf{u}} \times \hat{\mathbf{e}}_x)|} , \tag{3.11}
$$

$$
\delta \hat{\mathbf{u}}(t) = G_4 \sqrt{\frac{2k_B T \delta t}{\gamma_r}} \frac{\hat{\mathbf{u}} \times \hat{\mathbf{e}}_x}{|\hat{\mathbf{u}} \times \hat{\mathbf{e}}_x|} + G_5 \sqrt{\frac{2k_B T \delta t}{\gamma_r}} \frac{\hat{\mathbf{u}} \times (\hat{\mathbf{u}} \times \hat{\mathbf{e}}_x)}{|\hat{\mathbf{u}} \times (\hat{\mathbf{u}} \times \hat{\mathbf{e}}_x)|} , \tag{3.12}
$$

where G_{1-5} are Gaussian random numbers with unit variance.

Note that the above algorithm will gradually change the length of the unit vector $\hat{\mathbf{u}}$. There are two approaches to correct for this artifact: one can reset the length of the rods at the end of every time step by correcting either along the initial or along the final direction of the rod. This point has been thoroughly investigated by Cobb and Butler [19], who found that the first method is the proper way. We have tested both methods in our simulations, and found that for the timestep used here, there was no significant difference between the two approaches.

Equations (3.3), (3.4), (3.9) and (3.10) constitute the equations of motion used in this Chapter. We shall now prove that they give rise to the N-particle Smoluchowski equation,

$$
\frac{\partial P}{\partial t} = \sum_{j=1}^{N} \{ \frac{3}{4} D_t \nabla_j \cdot (\hat{\mathbf{I}} + \hat{\mathbf{u}}_j \hat{\mathbf{u}}_j) \cdot [\nabla_j P + \beta P \nabla_j \Phi] - \nabla_j \cdot [P \boldsymbol{\Gamma} \cdot \mathbf{r}_i]
$$
$$
+ D_r \hat{\mathscr{R}}_j \cdot [\hat{\mathscr{R}}_j P + \beta P \hat{\mathscr{R}}_j \Phi] - \hat{\mathscr{R}}_j \cdot [P \hat{\mathbf{u}}_j \times (\boldsymbol{\Gamma} \cdot \hat{\mathbf{u}}_j)] \} , \tag{3.13}
$$

which is considered to be the fundamental equation of motion [13, 22, 24] for the probability density function P of finding the system at time t in a state $z = \{z_1, \cdots, z_N\}$ with $z_i = \{\mathbf{r}_i, \hat{\mathbf{u}}_i\}$, given that it was in the state z_0 at time zero. Here, ∇_j denotes the gradient with respect to the position of particle j and $\hat{\mathscr{R}}_j \equiv \hat{\mathbf{u}}_j \times \nabla_{\hat{\mathbf{u}}_j}$, where $\nabla_{\hat{\mathbf{u}}_j}$ is the gradient with respect to the orientation of particle j. Furthermore, the diffusion coefficients D_t and D_r are given by

$$
D_t = \frac{D_\parallel + 2D_\perp}{3} = \frac{k_B T \ln(L/D)}{3\pi \eta_s L} , \tag{3.14}
$$
$$
D_r = \frac{3k_B T \ln(L/D)}{\pi \eta_s L^3} . \tag{3.15}
$$

The proof that we are going to give should be considered to be the decisive motivation for choosing the above equations of motion. The equivalence of the Brownian dynamics equa-

tions of motion and the Smoluchowski equation in the absence of shear flow has been derived in Appendix B of Ref. 133. When shear is taken into account, an additional term will appear in each of the expressions of the first moments described by Eq. (B8) of Ref. 133:

$$\langle \Delta \mathbf{r}; \delta t \rangle = -\mathbf{\Xi}^{-1}(t) \cdot \nabla \Phi(t) \delta t + \mathbf{\Gamma} \cdot \mathbf{r}(t) \, \delta t \, , \tag{3.16}$$

$$\langle \Delta \hat{\mathbf{u}}; \delta t \rangle = \frac{1}{\gamma_r} \hat{\mathbf{u}}(t) \times \hat{\mathscr{R}} \Phi(t) \delta t + [\hat{\mathbf{I}} - \hat{\mathbf{u}}(t)\hat{\mathbf{u}}(t)] \cdot \mathbf{\Gamma} \cdot \hat{\mathbf{u}}(t) \delta t \, . \tag{3.17}$$

Introducing these expressions into Eq. (B9) of Ref. 133 and using

$$(\hat{\mathbf{I}} - \hat{\mathbf{u}}\hat{\mathbf{u}}) \cdot \nabla_{\hat{\mathbf{u}}} = -\hat{\mathbf{u}} \times \hat{\mathscr{R}} \, , \tag{3.18}$$

$$\oint d\hat{\mathbf{u}} \, \mathbf{A}(\hat{\mathbf{u}}) \cdot \hat{\mathscr{R}} F(z) = -\oint d\hat{\mathbf{u}} \, (\hat{\mathscr{R}} \cdot \mathbf{A}(\hat{\mathbf{u}})) F(z) \, , \tag{3.19}$$

where F and $\mathbf{A}$ are an arbitrary function and vector field, respectively, we end up with two additional terms inside the curly brackets on the right-hand side of Eq. (B11) of Ref. 133:

$$-\nabla \cdot \mathbf{\Gamma} \cdot \mathbf{r} P(z, z_0; t) + \hat{\mathscr{R}} \cdot \{ [(\hat{\mathbf{I}} - \hat{\mathbf{u}}\hat{\mathbf{u}}) \cdot \mathbf{\Gamma} \cdot \hat{\mathbf{u}}] \times \hat{\mathbf{u}} \, P(z, z_0; t) \} \, . \tag{3.20}$$

Summing over all particles on the right-hand side of Eq. (B11) of Ref. 133, we obtain the N-particle Smoluchowski equation Eq. (3.13) given above.

In the case of dilute solutions, the systematic forces $\mathbf{F}_S$ and torques $\mathbf{T}_S$ are hardly important and can be neglected. However, in the case of concentrated solutions, mutual interactions between rods play a crucial role and the systematic forces $\mathbf{F}_S$ and torques $\mathbf{T}_S$ need to be taken into account. In our previous model, $\mathbf{F}_S$ and $\mathbf{T}_S$ were derived from an excluded volume potential Φ, which was chosen to be proportional to the overlap volume between two interacting rods. This model was successfully applied to measure the self and collective rotational diffusion coefficients in dilute and semidilute rod solutions [133]. But when focusing on concentrated systems of hard rods, some disadvantages of this model appear. As a result of the random displacements and reorientations, sometimes considerable overlaps and even crossings can not be prevented, irrespective of the smallness of the timestep δt. In order to achieve simulations of infinitely hard rod systems, a new simulation technique had to be developed.

In our new simulation program, the excluded volume potential and its corresponding systematic forces and torques have been eliminated in favor of an event-driven technique [118], inspired by the celebrated molecular dynamics simulations of hard spheres by Alder and Wainwright [1], which have been extended to molecular dynamics simulations of infinitely

thin rods by Frenkel and Maguire [48]. Between collisions, every rod performs a Brownian motion, independent of the other rods. At a collision this motion changes abruptly. If the linear and angular velocities of the colliding rods are known, it is straightforward to solve the impulsive collision analytically (including the two constraints on the lengths of the rods). In the overdamped case, when Brownian dynamics applies, the system looses its memory of the initial velocities long before its configuration has changed appreciably. In this case the velocities can be eliminated altogether and the time step is adjusted to the rate of change of the system configurations. Random displacements and reorientations are applied to the particles as, for example, in Eqs. (3.11) and (3.12). If the particle finds itself near a wall or any other obstacle like for example a companion particle, these random contributions have to be modified in a way which is known analytically only in a few simple cases with spherical particles [9, 115, 116]. It has been found, however, that in these cases no noticeable differences occur if the particle is moved in the usual way up to the point of contact with the obstacle and new random displacements, away from overlap, are chosen to complete the timestep. Several alternative approximate methods have been suggested to remove possible overlaps at time $t + \delta t$, all being more or less equally efficient [18, 63, 108, 109, 121, 128].

We propose to use a similar method in the case of Brownian dynamics simulations of rodlike colloids, *i.e.*, we use the random forces and torques at time t to advance two colliding rods up to the time of contact $t + \lambda \delta t$ with $0 < \lambda < 1$, according to an obvious modification of the original equations of motion,

$$\mathbf{r}_i(t + \lambda \delta t) = \mathbf{r}_i(t) + \mathbf{\Gamma} \cdot \mathbf{r}_i(t) \lambda \delta t + \delta \mathbf{r}(t) \sqrt{\lambda} \, , \tag{3.21}$$

$$\hat{\mathbf{u}}_i(t + \lambda \delta t) = \hat{\mathbf{u}}_i(t) + [\hat{\mathbf{I}} - \hat{\mathbf{u}}_i(t) \hat{\mathbf{u}}_i(t)] \cdot \mathbf{\Gamma} \cdot \hat{\mathbf{u}}_i(t) \lambda \delta t + \delta \hat{\mathbf{u}}(t) \sqrt{\lambda} \, . \tag{3.22}$$

At contact, new random displacement $\delta \mathbf{r}'(t)$ and reorientation $\delta \hat{\mathbf{u}}'(t)$ are sampled according to Eqs. (3.11) and (3.12), and

$$\mathbf{r}_i(t + \delta t) = \mathbf{r}_i(t + \lambda \delta t) + \mathbf{\Gamma} \cdot \mathbf{r}_i(t + \lambda \delta t) \delta t (1 - \lambda) + \delta \mathbf{r}'(t) \sqrt{1 - \lambda} \, , \tag{3.23}$$

$$\begin{aligned} \hat{\mathbf{u}}_i(t + \delta t) = {} & \hat{\mathbf{u}}_i(t + \lambda \delta t) + [\hat{\mathbf{I}} - \hat{\mathbf{u}}_i(t + \lambda \delta t) \hat{\mathbf{u}}_i(t + \lambda \delta t)] \cdot \mathbf{\Gamma} \cdot \hat{\mathbf{u}}_i(t + \lambda \delta t) \delta t (1 - \lambda) \\ & + \delta \hat{\mathbf{u}}'(t) \sqrt{1 - \lambda} \, , \end{aligned} \tag{3.24}$$

are used to complete the timestep.

In order to advance the system from time t to time $t + \delta t$, we perform the following steps:

1. At time t, a list of all possible collision pairs is compiled consisting of those pairs whose shortest distance is smaller than a certain distance criterion, say, r_{cut}. Shortest distance here means the shortest possible distance obtained by moving one point along the surface of one rod and another point along the surface of the other rod. This distance can conveniently be calculated for cylinders capped with hemispheres of equal radius. By regarding the oblong rods as being constructed from several segments and using a segment based grid and link-list, this step may be accelerated appreciably.

2. All rods are advanced from t to $t + \delta t$ according to free Brownian motions. The list of possible collision pairs is completed by adding those pairs whose shortest distance is smaller than r_{cut} at this new time $t + \delta t$. The criterion r_{cut} is the maximum separation between two rods that still allows for a collision to occur within a time lapse of $\frac{1}{2}\delta t$ or, in other words, the maximum distance that can occur between two rods during a time lapse of $\frac{1}{2}\delta t$ after initial contact; hence if a collision takes place between t and $t + \delta t$ the distance between the rods must be less than r_{cut} at t and/or at $t + \delta t$. Clearly, r_{cut} is a function of the viscosity, timestep *etc*. With a timestep of $0.5\ \mu$s, it proves that using the criterion $r_{cut} = D$ is always safe for preventing overlaps between rods.

3. For all pairs in the list, the time of first contact is determined by interpolation of the already chosen Brownian displacements and reorientations. To this end, the time interval is subdivided into one hundred smaller intervals and configurations are attributed to the end points of these intervals l using the original random numbers and the time lapse $l\delta t/100$ since the beginning of the time step. Note that this implies that the trajectories are assumed to be rectilinear in configuration space, but that the distance traveled along these trajectories varies with the square root of the time lapse, $\sqrt{l\delta t/100}$. Finally, for each pair the time of first contact is detected and the pairs are ordered according to increasing time of first contact.

4. The pair with the shortest time of first contact is advanced up to contact. Next, new random displacements and reorientations are chosen for this pair such that the rods separate initially and the table of collision pairs is updated. New times of first contact are calculated for all pairs in the list which involve one of the two rods of the last collision and step 4 is repeated until all possible collisions within the given time step have been

exhausted. This way, a rod may collide several times per timestep, as illustrated by rod j in Fig. 3.1, and it is even possible for two rods to collide repeatedly with each other in one step.
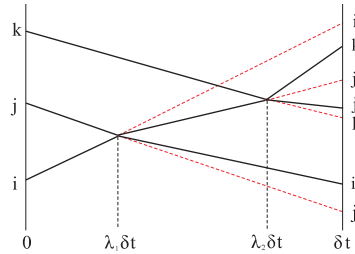

Figure 3.1: *A cartoon of the trajectories of three interacting rods during one timestep δt. On the left hand side, i, j and k mark the start positions of the rods. On the right hand side, i, j and k denote the prospective positions of the rods at the end of the step for the given initial set of random forces and torques. At the collision moments $\lambda_1 \delta t$ and $\lambda_2 \delta t$ new random forces and torques are drawn for the two colliding particles. The resulting modified final positions are indicated by (double) primed indices. Solid lines denote the traversed trajectories, dotted lines are extrapolations.*

A comment as to the chosen method is in order here. As we already mentioned, the exact propagator for colliding Brownian particles is known for a few cases only. For point-like particles near a flat wall, each particle which after a trial step ends in the forbidden area should be mirrored in the wall. For colliding rods no exact solution is known; the reflection method proposed by Doi *et al.* [37], in which a particle retraces its path after a collision, can only be considered a very approximate solution. Harlen *et al.* [58] prevented rods from crossing by introducing a normal constraint force between the rods, whose strength is determined by the condition that the nearest distance can not drop below the rod diameter. These procedures are only correct in the limit of very small timesteps, in which case the number of regular Brownian steps by far exceeds the number of (approximate) collision steps. Therefore, we have chosen to subdivide the large main timestep into smaller timesteps for each colliding pair, assuming that the smallest timestep still exceeds the contact time. The latter assumption is perhaps less realistic at high shear rates, where the flow may force the rods to slip along

one another.

The simulation system in the present work is based on the experimental data of *fd* viruses [88]. The simulation box is cubic and contains $N = cL\varphi/D$ rods, with $c = 500$ for $L/D \leq 30$ and $c = 1000$ for $L/D \geq 60$, of diameter $D = 14.8$ nm. Here φ denotes volume fraction, defined as $\varphi = \frac{1}{4}\pi n D^2 L$ for hard rods with n the number density, and $L\varphi/D$ is referred to as the scaled volume fraction. The aspect ratios L/D range from 10 to 68, hence the lengths of the rods range from $L = 0.148\,\mu$m to $L = 0.888\,\mu$m. Water is used as the solvent, with viscosity $\eta_s = 10^{-3}$ Pa s. The temperature is 300 K. The efficiency of the above described algorithm is largely determined by the chosen timestep. At a low value of δt there will be few collisions, but a large number of timesteps are needed; for high δt the length of the collision list grows rapidly, and we might even need smaller interpolation steps to determine the times of first contact. The optimum value of δt will vary with the system studied. To make sure that during one time step the rods will not move or rotate too much, the time step δt is chosen in such a way that the maximum random displacement is smaller than one tenth of the thickness of the rod and so that the maximum random reorientation will not be larger than $2D/10L$. We thus arrive at a timestep $\delta t = 0.5\ \mu$s used for all simulations in this Chapter, which is ten times larger than that used in our previous simulations [133] with soft interactions between rods. Notice that this is still two orders of magnitude smaller than the timestep for which Cobb and Butler [19] discern a difference between the two approaches to conserve the length of the unit vector $\hat{\mathbf{u}}$.

3.2.2   Validation of the algorithm

In order to test the new algorithm, Brownian dynamics simulations were carried out measuring the self rotational diffusion coefficients $D_r(\varphi)$ of dilute and semidilute solutions of rods. We measured these coefficients by calculating

$$\langle \hat{\mathbf{u}}(t) \cdot \hat{\mathbf{u}}(0) \rangle = \exp\left\{-2D_r(\varphi)t\right\}. \tag{3.25}$$

The results are presented in Fig. 3.2 as a function of $L\varphi/D$ for two values of L/D together with similar results obtained with our previous program [133]. As is clear from this figure, the results obtained with the two programs are in perfect agreement with each other. Besides this agreement, preliminary simulations of the dynamics of dense solutions of rigid rods
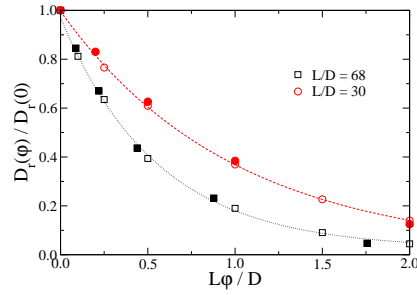
Figure 3.2: *The self rotational diffusion coefficients of rigid rods with aspect ratios $L/D =$ 30 and 68 as a function of the scaled volume fraction $L\varphi/D$. The open symbols denote results calculated with the new event-driven algorithm for hard rods, while the solid symbols are obtained by our previous algorithm in which the interaction potential between rods was proportional to their overlap volume.*

in shear flow have revealed [129] periodic motions whose periods are in good agreement with experimental results. We therefore consider our new algorithm to correctly describe the dynamics of Brownian rods, even when applied to dense systems.

3.2.3 Start configurations

The orientational order is usually measured by the scalar order parameter P_2, defined as $P_2 = (3\lambda - 1)/2$, where λ is the largest eigenvalue of the orientational order parameter tensor

$$\mathbf{S} = \frac{1}{N} \sum_{i=1}^{N} \hat{\mathbf{u}}_i \hat{\mathbf{u}}_i \; . \tag{3.26}$$

Hence, P_2 is zero in an isotropic state and becomes unity in a well aligned nematic state. The director $\hat{\mathbf{n}}$, given by the eigenvector corresponding to λ, points along the average direction of the rods. Investigations of the motions that $\hat{\mathbf{n}}$ exhibits in a shear flow will be published elsewhere [129, 130].

It is relatively easy to construct an initially perfectly aligned state by randomly placing parallel rods in the box, rejecting those rods that overlap with a previously accepted rod. This procedure is repeated until the desired number of rods is reached. An initially isotropic box is made in exactly the same way, selecting both positions and orientations of every inserted rod

47

at random. This production becomes increasingly challenging with rising volume fraction and aspect ratio, as more and more rods are being rejected. In practice, we find that scaled volume fractions $L\varphi/D$ of 3, 3.5 and 4 are attainable this way for $L/D = 10$, 15 and ≥ 20, respectively. Williams and Philipse [141] have shown that the theoretical maximum is given by $L\varphi/D = 5.1$, which lies well above our scaled volume fractions. The isotropy of the produced boxes is tested by confirming that the order matrix is isotropic, $S_{ij}(0) \approx \frac{1}{3}\delta_{ij}$, and by the absence of domains under visual inspection.

3.3 Results and discussions

In this section, we describe the results of our simulations of semidilute and dense systems of rod-like colloids. First, we address the scaling of the self rotational diffusion with density. In the remaining part of this section, we study the spinodals of the isotropic-nematic phase transition.

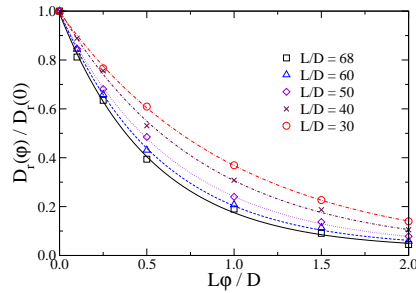### 3.3.1 Rotational diffusion coefficients

Figure 3.3: *The self rotational diffusion coefficients of rigid rods with various aspect ratios as a function of the scaled volume fraction.*

In Fig. 3.3, we have plotted the rotational diffusion coefficients as a function of $L\varphi/D$ for various aspect ratios. At the relatively low volume fractions to which this figure applies, the self rotational diffusion coefficients are virtually equal to the collective rotational diffusion coefficients (*vide infra*), which by Dhont and Briels were predicted to be linear in $L\varphi/D$. The

marked difference between the simulation results and the theoretical prediction must be due to the neglect of dynamic correlations in the latter. An alternative, more phenomenological analysis based on the tube concept has been presented by Doi and Edwards [34, 35], which was then confirmed by Monte Carlo simulations [37] on systems of rods with zero diameter. According to their theory, the self rotational diffusion coefficients in the semidilute regime should scale as

$$D_r(\varphi) = \beta D_r(0)(nL^3)^{-2}, \tag{3.27}$$

where β is some numerical parameter. In Fig. 3.4, we plot our results as a function of nL^3 on a log-log scale. It is clearly seen from this figure that with increasing values of L/D, the curves approach a limiting master curve with a slope equal to -2, thereby confirming the prediction of Doi and Edwards. Similar evidence has recently been published by Cobb and Butler [19].
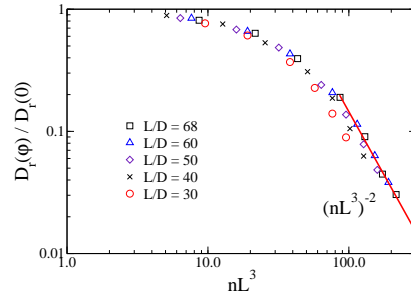

Figure 3.4: *The self rotational diffusion coefficients of rigid rods with various aspect ratios L/D as a function of the scaled volume fraction nL^3 on log-log scale. Here n is the number density. The solid line is a linear fit based on the results for $L/D = 68$.*

The collective rotational diffusion coefficient describes the decay back to zero of a small perturbation $\delta \mathbf{S}(t) = \mathbf{S}(t) - \frac{1}{3}\hat{\mathbf{I}}$ to the isotropic state. This can be obtained by starting with an aligned state and picking up the late stage behaviour. For volume fractions where the decay becomes very slow, this can not be done any more and we resort to invoke Onsager's regression hypothesis [12, 15], which states that time dependent fluctuations in a stable or metastable state decay according to the macroscopic laws, *i.e.*, in the present case:

$$\langle \delta \mathbf{S}(t) \delta \mathbf{S}(0) \rangle = \langle \delta \mathbf{S}(0) \delta \mathbf{S}(0) \rangle \exp\{-6 D_r^{\text{coll}}(\varphi)t\} , \tag{3.28}$$

49

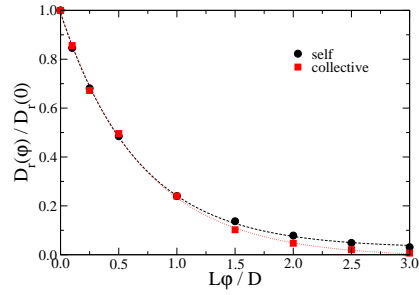Figure 3.5: *The simulated self (circles) and collective (squares) rotational diffusion coefficients as a function of the scaled volume fraction $L\varphi/D$ for solutions of rods with $L/D = 50$.*

where $D_r^{coll}(\varphi)$ is the collective rotational diffusion coefficient.

In Fig. 3.5, we present both the self and collective rotational diffusion coefficients as functions of $L\varphi/D$ for $L/D = 50$. As mentioned before [133], at lower volume fractions, both diffusion constants are almost equal to each other. At higher volume fractions, however, the collective diffusion coefficient keeps decaying, while the self diffusion coefficient levels off to remain nonzero.

3.3.2 Spinodals

As a result of the severe constraints set by the infinitely hard interactions between the particles, dense systems of rods undergo a phase transition from an isotropic state to a nematic state. With increasing volume fractions, the orientations of the individual rods in the isotropic state become more correlated, until at the isotropic-nematic spinodal (INS) the isotropic state becomes absolutely unstable. At volume fractions above the INS, the slightest perturbation will drive an isotropic system towards the ordered nematic state. Similarly, on lowering the volume fraction, an initially stable nematic state will finally become unstable at the nematic-isotropic spinodal (NIS) volume fraction. Actually no ordered state exists below the NIS, not even an unstable one [71]. Between the NIS and INS, the fate of the system depends on its initial state. Initial states with enough order will end up in the nematic state, others will end up in the isotropic state. In the Onsager limit of infinitely long rods, the above scenario has been described in detail by Kayser and Raveché [71]. For completeness we notice that
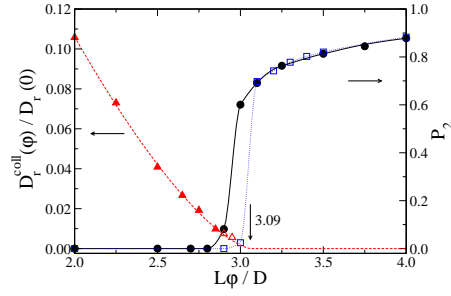
Figure 3.6: *The scalar order parameter P_2 versus the scaled volume fraction $L\varphi/D$ for solutions of rods with aspect ratio $L/D = 20$. The closed circles and open squares denote stationary order parameters obtained when starting the simulations with perfectly aligned and isotropic boxes, respectively. The collective rotational diffusion coefficients are plotted as triangles. The closed triangles are calculated from the decay of an initially aligned state, the open triangles are obtained by autocorrelating thermal fluctuations, see Eq. (3.28). The dashed line is a fit with Eq. (3.29), reaching zero at the isotropic-nematic spinodal indicated by an arrow.*

the thermodynamically stable state is only obtained after the system has splitted into two different phases whose densities are given by the two binodal points.

In Fig. 3.6, we show the measured order parameter P_2 against the scaled volume fraction $L\varphi/D$ for solutions of rods with an aspect ratio of $L/D = 20$. P_2 is taken to be the stable value when the system has reached equilibrium starting from a predescribed state. The solid circles present order parameters of initially perfectly aligned systems decaying to the nematic or isotropic state. For dense systems when $L\varphi/D > 3.0$, the order parameter P_2 decays from unity to some finite value indicative of the nematic state. In the cases when the volume fraction $L\varphi/D < 3.0$, the nematic state becomes unstable and the order parameters P_2 of these systems quickly decay to zero. The NIS can be read from the abrupt decrease of the order parameter, which is considered to occur at 3.0.

In order to measure the INS concentration, we performed simulations of initially isotropic systems with various volume fractions $L\varphi/D$. In systems with $L\varphi/D < 3.0$, the rods remained chaotic, while in cases with $L\varphi/D > 3.1$, all systems spontaneously ordered into a nematic phase. The isotropic-nematic spinodal is therefore located somewhere between
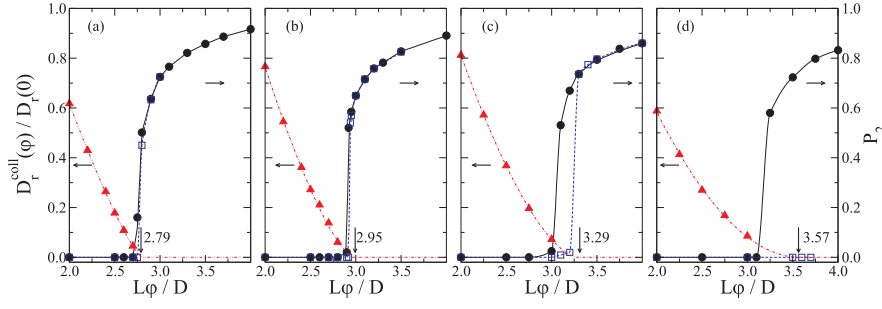
Figure 3.7: *The scalar order parameters P_2 and collective rotational diffusion coefficients $D_r^{coll}(\varphi)$ as functions of the scaled volume fraction $L\varphi/D$ for aspect ratios of 10(a), 15(b), 30(c) and 60(d). The arrows and numbers refer to the INS spinodals obtained by using Eq. (3.29). The values of $D_r^{coll}(\varphi)/D_r(0)$ in (a)-(d) are multiplied by 5, 8, 10, and 20, respectively.*

$L\varphi/D = 3.0$ and 3.1. The results of these simulations are represented by the squares in Fig. 3.6.

For those systems where the density is very close to the INS concentration, the order parameter becomes more and more sensitive against the volume fraction, so that it is difficult to measure an accurate spinodal concentration using this method. In order to better pinpoint the INS volume fraction, we suggest to calculate the collective rotational diffusion coefficient $D_r^{coll}(\varphi)$ and search for the volume fraction where it becomes zero. The rationale for this is that at the INS, the driving force for the system to become either isotropic or nematic is zero. In Fig. 3.6, besides the order parameters already discussed, we have plotted the collective rotational diffusion coefficients for the case $L/D = 20$. The solid triangles are obtained by studying the late stages of decaying perturbations $\delta S(t)$ of the isotropic state, while the open triangles result from applying Eq. (3.28). The dashed line results from a fit through these points according to

$$\frac{D_r^{coll}(\varphi)}{D_r(0)} = A \left(\frac{L}{D}\varphi_{INS} - \frac{L}{D}\varphi \right)^\alpha , \tag{3.29}$$

where φ_{INS} is the INS volume fraction. The fit is only applicable in a restricted interval of $L\varphi/D$ values leading to a value of A different from $(L\varphi_{INS}/D)^{-\alpha}$.

To map out the complete set of spinodals, similar simulations were performed for systems

with aspect ratios $L/D = 10, 15, 30$ and 60. The results are shown in Fig. 3.7(a)-(d). We estimated the nematic-to-isotropic spinodals from the abrupt decay of the order parameter P_2, obtaining $L\varphi_{NIS}/D \approx 2.8$, 2.9, 3.1 and 3.25 for solutions of rods with $L/D = 10$, 15, 30 and 60, respectively. As with boxes with $L/D = 20$, we calculated $D_r^{\text{coll}}(\varphi)$ in the stable and metastable isotropic states and calculated φ_{INS} by fitting the results with Eq. (3.29). The measured $D_r^{\text{coll}}(\varphi)$ and the fits are shown in Fig. 3.7(a)-(d). For curiosity we notice that the exponents in Eq. (3.29) are well described by

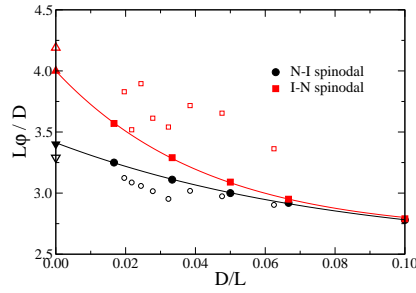$$\alpha = \frac{1}{\sqrt{2}} \left(\frac{L}{D} \right)^{1/4} . \tag{3.30}$$

Figure 3.8: *The INS (solid squares) and NIS (solid circles) spinodals as functions of D/L. The open squares and circles are the binodals calculated in Ref. 10. The use of D/L, rather than the shape anisotropy L/D, facilitates the comparison with theoretical predictions. The theoretical binodals (open triangles) and spinodals (solid triangles) at infinite aspect ratio are plotted on the y-axis for $D/L = 0$; these points were not included when fitting the lines.*

We summarize our findings about the spinodals of the isotropic-nematic phase transition by plotting the scaled volume fractions $L\varphi_{INS}/D$ and $L\varphi_{NIS}/D$ in Fig. 3.8 as functions of D/L. It is seen that the larger the aspect ratio is, the more discrepant are the volume fractions of the two spinodals, while for short rods the region between the two spinodals becomes quite narrow. The drawn lines in Fig. 3.8 are fits to the results of our simulations with

$$
\begin{aligned}
L\varphi_{INS}/D &= 1.4 \, e^{-23D/L} + 2.7 \, , \\
L\varphi_{NIS}/D &= 0.9 \, e^{-12D/L} + 2.5 \, .
\end{aligned} \tag{3.31}
$$

Their extrapolations to the Onsager limit, *i.e.*, to $D/L = 0$, meet the vertical axis at $L\varphi_{NIS}/D =$

3.4 and $L\varphi_{INS}/D = 4.0$, respectively. These results are in good agreement with previous theoretical predictions [71, 114]. The open squares and circles in Fig. 3.8 are taken from Table XI in Bolhuis and Frenkel [10], and represent the binodals at the given values of D/L. It is seen that our spinodals are between the two binodals at all values of D/L, as they should be.

3.3.3 Spinodal shift due to shear

In shear flow, the director of a nematic system of rod-like colloids will orient itself along the flow direction. Besides this, the flow will slightly sharpen the orientational distribution of the individual rods and enlarge the order parameter. Also in the isotropic state an applied shear flow will slightly align the rods along the flow direction. As a result, the two spinodals corresponding to the isotropic-nematic phase transition will slightly shift to lower volume fractions with increasing shear rate. In accordance with our use in the previous section, we define φ_{INS} and φ_{NIS} as the volume fractions where

$$\frac{d\mathbf{S}}{dt} = 0 \,, \ \mathbf{S}(0) = \frac{1}{3}\hat{\mathbf{I}}, \tag{3.32}$$

and

$$\frac{d\mathbf{S}}{dt} = 0 \,, \ \mathbf{S}(0) = \hat{\mathbf{n}}\hat{\mathbf{n}}, \tag{3.33}$$

respectively, fail to have solutions close to $\mathbf{S}(0)$. According to Dhont and Briels [24]

$$\frac{d}{dt}\mathbf{S} = -6\mathrm{D}_r\left\{\mathbf{S} - \frac{1}{3}\hat{\mathbf{I}} + \frac{5}{4}\frac{L}{D}\varphi(\mathbf{S}^{(4)} : \mathbf{S} - \mathbf{S}\cdot\mathbf{S})\right\} + \dot{\gamma}\left\{\hat{\mathbf{\Gamma}}\cdot\mathbf{S} + \mathbf{S}\cdot\hat{\mathbf{\Gamma}}^T - 2\mathbf{S}^{(4)} : \hat{\mathbf{E}}\right\} \,, \tag{3.34}$$

where $\hat{\mathbf{E}} = \frac{1}{2}[\hat{\mathbf{\Gamma}} + \hat{\mathbf{\Gamma}}^T]$, with the superscript T denoting a transposition, and $\mathbf{S}^{(4)} = \langle\hat{\mathbf{u}}\hat{\mathbf{u}}\hat{\mathbf{u}}\hat{\mathbf{u}}\rangle$. We added a factor of $5/4$ to the term proportional to $L\varphi/D$, which results from a slightly better evaluation of the excluded volume interaction between two rods with orientations $\hat{\mathbf{u}}$ and $\hat{\mathbf{u}}'$ respectively (see Appendix 3.A). The above equation may be closed by using the approximation [24]

$$\mathbf{S}^{(4)} : \mathbf{M} \approx \frac{1}{5}\left\{\mathbf{S}\cdot\mathbf{M} + \mathbf{M}\cdot\mathbf{S} - \mathbf{S}\cdot\mathbf{S}\cdot\mathbf{M} - \mathbf{M}\cdot\mathbf{S}\cdot\mathbf{S} + 2\mathbf{S}\cdot\mathbf{M}\cdot\mathbf{S} + 3\mathbf{S}\mathbf{S} : \mathbf{M}\right\} \,, \tag{3.35}$$

where $\mathbf{M}$ is either $\mathbf{S}$ or $\hat{\mathbf{E}}$. Finally, $\mathbf{\Gamma}$ defines the flow by $\mathbf{V} = \mathbf{\Gamma}\cdot\mathbf{r}$ and equals $\dot{\gamma}\hat{\mathbf{e}}_x\hat{\mathbf{e}}_y$ for simple shear flow. Assuming uniaxial ordering and $\dot{\gamma} = 0$, Eq. (3.33) may be solved analytically to
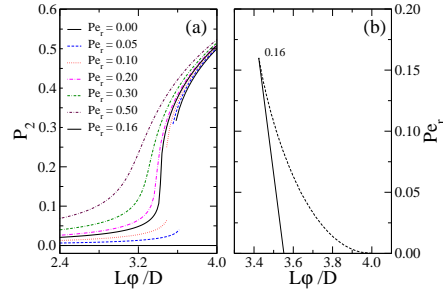
Figure 3.9: *(a) The theoretical scalar order parameter P_2 as a function of the scaled volume fraction $L\varphi/D$ at various shear rates for $L/D = \infty$. At low shear rates, the flow induces a small paranematic alignment in the isotropic phase and increases the alignment of the nematic phase. The end points of these lines are the INS and NIS spinodals, which are plotted in (b) as a function of the Peclet number Pe_r. At the critical shear rate, corresponding to $\mathrm{Pe}_r = 0.16$, the spinodals coalesce and end, hence the two phases merge into a single phase.*

find (see Appendix 3.B)

$$P_2 = \frac{3}{4}\sqrt{1 - \frac{32}{9}\frac{D}{L\varphi}} + \frac{1}{4} \ . \tag{3.36}$$

The results of solving Eqs. (3.32) and (3.33) are presented in Fig. 3.9. It is seen that with increasing Peclet number $\mathrm{Pe}_r = \dot{\gamma}/D_r$ the two spinodal volume fractions approach each other to become equal at the critical Peclet number $\mathrm{Pe}_r = 0.16$ where the isotropic-nematic phase transition ceases to exist [24]. For $\mathrm{Pe}_r = 0$ the spinodals are $L\varphi_{INS}/D = 4.0$ and $L\varphi_{NIS}/D = 32/9$ in good agreement with our finding in the previous section.

In Fig. 3.10 we present the results obtained by solving Eqs. (3.32) and (3.33) by means of Brownian dynamics simulations for $L/D = 20$ and 30 and for various values of the Peclet number. Closed symbols refer to stationary states obtained by starting with $\mathbf{S}(0) = \hat{\mathbf{n}}\hat{\mathbf{n}}$, *i.e.*, by solving Eq. (3.33), while open symbols refer to stationary states obtained by starting with $\mathbf{S}(0) = \frac{1}{3}\hat{\mathbf{I}}$. Obviously the aspect ratios pertaining to this figure are all rather small for the results to apply to the case $L/D = \infty$ treated by the theory presented above. Unfortunately it is extremely difficult to extend these simulations to systems with large aspect ratios. Still, from the results found so far, it is clear that theory and simulations are in agreement qualitatively.
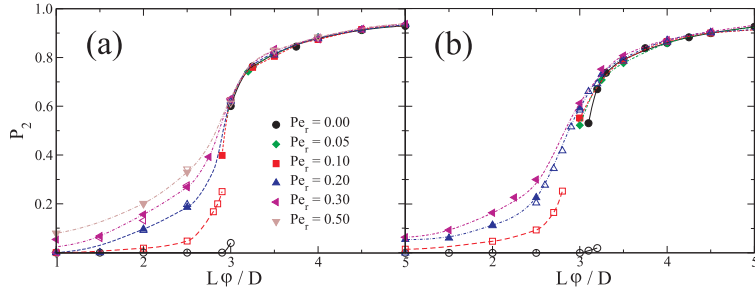
55

Figure 3.10: *The simulated scalar order parameters P_2 as functions of the scaled volume fraction $L\varphi/D$ at various shear rates for (a) $L/D = 20$ and (b) $L/D = 30$.*

The order parameter is underestimated substantially by the theory, but the evolution of the spinodals with increasing Peclet number is qualitatively right. Moreover the estimate of 0.16 for the critical number is well in the range $(0.1, 0.2)$ found from the simulations.

3.4 Conclusion

We have described a new event-driven Brownian dynamics algorithm with which concentrated solutions of rigid spherocylinders in shear flow can be investigated. Compared with existing Brownian dynamics simulations of rigid rods where overlaps between particles are prevented by a repulsive potential, the novelty of the new code is in the fact that its time evolution is controlled by collisions, like in time of flight molecular dynamics simulations. Excluded volume interactions between the rods are considered to be infinitely hard, but hydrodynamic interactions are neglected. The new algorithm is very efficient, as exemplified by the fact that the timestep δt is at least 10 times larger than the one used in our previous work [133]. The general picture of the present Chapter is summarized as follows:

1. The calculated self rotational diffusion coefficients $D_r(\varphi)$ by both the new event-driven Brownian dynamics simulations and our previous program accord very well with each other, confirming the validity of our new simulation algorithm.

2. Isotropic-nematic spinodals are calculated of rod systems with various aspect ratios L/D. The simulated INS and NIS spinodals are well located between the binodals

measured by Bolhuis and Frenkel [10] by Monte Carlo simulations, as they should be. The extrapolations of the spinodals to the infinitely long rod system are in good agreement with previous theoretical predictions by Onsager and Kayser *et al.*

3. Shear-shifts of the spinodals to lower values are investigated. The measured order parameters deviate substantially from the theoretical predictions [24], but the spinodal concentrations agree rather well. The estimated critical rotational Peclet number Pe_r, above which only continuous and reversible changes of the order parameters can be found, agree qualitatively with the predicted value $\text{Pe}_r = 0.16$.

The present successful Brownian dynamics algorithm allows us to investigate in detail the dynamical properties of nematic liquid-crystalline solutions of rigid spherocylinders in shear flow. Some fascinating rheological phenomena such as the oscillating responses of the director, *i.e.*, tumbling, kayaking, wagging or flow-aligning, to a steady driving "force" will be represented in *Chapter* 4 and 5.

Appendix 3.A: Maier-Saupe expansion

In the derivation of Eq. (3.34), the excluded volume of two rigid rods gives rise to an effective potential proportional to

$$\int d^3 \mathbf{R} \, \chi(\mathbf{R}, \hat{\mathbf{u}}, \hat{\mathbf{u}}') = 2DL^2 \left| \hat{\mathbf{u}} \times \hat{\mathbf{u}}' \right| , \tag{3.A1}$$

where $\mathbf{R}$ is the vector separating two rods with orientations $\hat{\mathbf{u}}$ and $\hat{\mathbf{u}}'$, respectively, and $\chi(\mathbf{R}, \hat{\mathbf{u}}, \hat{\mathbf{u}}')$ equals 1 when two rods overlap and 0 otherwise. The vector products $\left| \hat{\mathbf{u}} \times \hat{\mathbf{u}}' \right|$ may be expanded in terms of polyadic products $\mathbf{q}_k$ of $\hat{\mathbf{u}}$'s, which may be chosen such that

$$\oint d\hat{\mathbf{u}} \, \mathbf{q}_k \mathbf{q}_l \sim \delta_{k,l} . \tag{3.A2}$$

The first three of these may be chosen as

$$\begin{aligned}
\mathbf{q}_0 &= 1 , \\
\mathbf{q}_1 &= \hat{\mathbf{u}} , \\
\mathbf{q}_2 &= \hat{\mathbf{u}}\hat{\mathbf{u}} - \frac{1}{3}\hat{\mathbf{I}} .
\end{aligned} \tag{3.A3}$$

Expanding $\left|\hat{\mathbf{u}} \times \hat{\mathbf{u}}'\right|$ up to second order, we obtain

$$\left|\hat{\mathbf{u}} \times \hat{\mathbf{u}}'\right| = a_0 + a_2 \mathbf{q}_2' : \mathbf{q}_2 , \tag{3.A4}$$

where we have used the existing symmetry between $\hat{\mathbf{u}}$ and $\hat{\mathbf{u}}'$. Using

$$\oint d\hat{\mathbf{u}} \left|\hat{\mathbf{u}} \times \hat{\mathbf{u}}'\right| = \pi^2 ,$$
$$\oint d\hat{\mathbf{u}} \left|\hat{\mathbf{u}} \times \hat{\mathbf{u}}'\right| \mathbf{q}_2 = -\frac{\pi^2}{8} \mathbf{q}_2' , \tag{3.A5}$$

we obtain

$$a_0 = \frac{1}{4}\pi , \quad a_2 = -\frac{15}{64}\pi . \tag{3.A6}$$

Using Eq. (3.A6) in Eq. (3.A4) and rewriting the result a bit we arrive at

$$\left|\hat{\mathbf{u}} \times \hat{\mathbf{u}}'\right| = \frac{21\pi}{64} \left[1 - \frac{5}{7}\hat{\mathbf{u}}\hat{\mathbf{u}} : \hat{\mathbf{u}}'\hat{\mathbf{u}}' \right] . \tag{3.A7}$$

Compared with the corresponding expansion in Ref. 24, the second term has an extra factor of $5/4$, which finally leads to the factor of $5/4$ in front of the term proportional to $L\varphi/D$ in Eq. (3.34).

Appendix 3.B: Zero shear nematic order parameter

For the case when $\dot{\gamma} = 0$ the equation of motion of $\mathbf{S}$ simplifies to

$$\frac{d}{dt}\mathbf{S} = -6\mathrm{D}_r \left\{ \mathbf{S} - \frac{1}{3}\hat{\mathbf{I}} + \frac{3}{4}\frac{L}{D}\varphi(\mathbf{SS} : \mathbf{S} - \mathbf{S}\cdot\mathbf{S}) \right\} , \tag{3.B1}$$

where we have made use of the closure equation (3.35). Assuming uniaxial symmetry, $\mathbf{S}$ may be written like

$$\mathbf{S} = \lambda\hat{\mathbf{n}}\hat{\mathbf{n}} + \frac{1}{2}(1-\lambda)\hat{\mathbf{e}}_2\hat{\mathbf{e}}_2 + \frac{1}{2}(1-\lambda)\hat{\mathbf{e}}_3\hat{\mathbf{e}}_3$$
$$= \frac{1}{2}(1-\lambda)\hat{\mathbf{I}} + \frac{1}{2}(3\lambda - 1)\hat{\mathbf{n}}\hat{\mathbf{n}} , \tag{3.B2}$$

where $\hat{\mathbf{e}}_2$ and $\hat{\mathbf{e}}_3$ are two unit vectors perpendicular to each other and to $\hat{\mathbf{n}}$. Introducing this into Eq. (3.B1), one finds after some rewriting

$$\frac{d}{dt}\left[\mathbf{S} - \frac{1}{3}\hat{\mathbf{I}}\right] = -6\mathrm{D}_r \left\{ 1 - \frac{9}{8}\frac{L}{D}\varphi\lambda(1-\lambda) \right\} \left[\mathbf{S} - \frac{1}{3}\hat{\mathbf{I}}\right] . \tag{3.B3}$$

A stationary nonzero value of $\mathbf{S} - \frac{1}{3}\hat{\mathbf{I}}$ can only be found for values of $L\varphi/D$ for which the factor between curly brackets can be put equal to zero. This leads to Eq. (3.36).

4 Kayaking and wagging of rods in shear flow

For the first time, we have simulated the periodic collective orientational motions performed by rigid liquid-crystalline polymers (LCPs) with large aspect ratio in the nematic state in shear flow. In order to be able to do so, we developed a new, event-driven Brownian dynamics technique. We present the results of simulations of rods with aspect ratios L/D ranging from 20 to 60 at volume fractions φ given by $L\varphi/D = 3.5$ and 4.5. By studying the path of the director i.e., the average direction of the rods, we observe kayaking, wagging, flow aligning and log rolling type of orbits, depending on the parameters of the simulation and the initial orientation. We find that the tumbling periods depend on $L\varphi/D$ and the shear rate but not on the type of motion. Our simulation results qualitatively confirm theoretical predictions and are in good agreement with the experimental measurements of tumbling times of fd virus. **

Single elongated rigid particles in a shear flow described by $\mathbf{V}(\mathbf{r}) = \dot{\gamma} \, y \, \hat{\mathbf{e}}_x$, with $\mathbf{r} = x\hat{\mathbf{e}}_x + y\hat{\mathbf{e}}_y + z\hat{\mathbf{e}}_z$, trace out Jeffery orbits named after the scientist who first described this motion [70]. For example, a particle initially aligned along the flow axis $\hat{\mathbf{e}}_x$ will start to rotate in the shear plane, *i.e.*, the *xy*-plane, with a period depending on both the aspect ratio of the particle and the shear rate. Particles whose long axes initially make nonzero angles with the shear plane perform motions akin to that of the paddles of somebody kayaking. It is to be expected that in a dense system of elongated particles in shear flow the particles will strongly interact and will not be able to perform Jeffery motion independently of each other. If there

is any tumbling at all, this has to be performed by the particles collectively. It is this rather spectacular motion that we have investigated by means of Brownian dynamics simulation. and that we address in this Chapter.

The dynamics of dense systems of elongated particles in shear flow was first investigated from a theoretical point of view independently by Hess [59] and Doi [33]. The central object of their investigation was the director, which is the unit vector $\hat{\mathbf{n}}$ pointing along the average direction of the long axes of all particles. A particle with long axis $\hat{\mathbf{u}}$ running through a Jeffery path $\hat{\mathbf{u}}_J(t)$ may be characterized by a time dependent probability density $P(\hat{\mathbf{u}},t) = \delta(\hat{\mathbf{u}} - \hat{\mathbf{u}}_J(t))$ where δ is a Dirac delta function on the two dimensional unit sphere. The corresponding evolution equation may serve as starting point to derive the equation governing the evolution of the probability density $P(\hat{\mathbf{n}},t)$ of the director of a dense system of elongated particles. To this end we must add to the original evolution equation terms which account for perturbations of the Jeffery paths caused by the interactions between particles and by the random kicks exerted by the solvent molecules on these particles. Doing so we arrive at the Smoluchowski equation first derived by Hess and Doi.

The initial motivation for deriving the Doi-Hess equation was to obtain expressions relating the aspect ratio of the particles to the various coefficients occurring in the phenomenological theory by Ericksen [38] and Leslie [89]. The latter theory, in combination with results obtained by means of the Doi-Hess equation, has been very successful in describing the rich rheology of dense rodlike particles systems. Besides describing rheology, solutions of the Doi-Hess equation provide detailed molecular information which is difficult to obtain experimentally. Over the last two decades the following picture has emerged: At low shear rates and sufficiently high volume fractions, all particles collectively tumble in the shear plane [79, 80, 97] or perform Jeffery type of motions [84] called kayaking. Tumbling is only observed if the director is initially in the shear plane. Recently however it has been claimed [41] that tumbling always is unstable with respect to kayaking. With increasing shear rates tumbling and kayaking go over into wagging [41, 80, 84] and finally into a shear aligned state [41, 79, 80, 84, 97]. In the wagging state the director periodically moves up and down in the shear plane in a symmetrical way about the flow direction. In the shear aligned state the director is arrested [80] in the shear plane making a fixed nonzero angle with the flow direction. There is one more stationary state, one in which the director is initially aligned along the

vorticity direction, *i.e.*, the *z*-axis, and remains there; this state is called the log-rolling state. For a more complete description of all possible motions and their dependence on the initial state, we refer to Hess and Kröger [62, 76] and references given there. Recently, a thorough analysis of the predictions of the Doi-Hess equation, avoiding any additional approximation not implicit in the use of the Doi-Hess equation, has been published by Forest *et al.* [44, 45].

The Doi-Hess equation from which the above picture has emerged is based on a number of approximations which were itemized by Dhont and Briels [24]. Recently we have shown by means of Brownian dynamics simulations that at low volume fractions of suspended rods, these have severe consequences for the predictions made by the theory [133]. In particular, the theory neglects dynamic correlations between neighbouring rods and it may therefore be questioned if it is capable of correctly describing collective motions in dense systems. Moreover, although periodic responses have been observed in rheological experiments [14, 56, 105], no simple measurements exist discriminating between the various kinds of periodic motions. In this situation, computer experiments simulating the full *N*-particle Fokker-Planck equation will be of great value. Only very few attempts in this direction have been undertaken. Brownian dynamics simulations by Doi *et al.* [142, 143] are restricted to elongated particles in the semi-dilute isotropic state. The simulations of Mori *et al.* [106, 107] do address the dense state, but are restricted to particles with aspect ratio equal to 3. In the first case overlap between particles was prohibited by very steep, short range lubrication forces, in the second case by a Gay-Berne potential. Such forces become increasingly difficult to handle with increasing aspect ratio and volume fraction. We therefore set out to develop a new, event driven Brownian dynamics algorithm which efficiently handles dense systems of Brownian hard rods, and to perform simulations of such systems in shear flow. The novelty of the code is in the fact that its time evolution is controlled by collisions, like in time of flight molecular dynamics simulations, and not by a potential preventing overlaps.

The simulation was done by means of an event driven Brownian dynamics code neglecting hydrodynamic interaction between rods. During each time step Δt the rods were propagated from position $\mathbf{r}(t)$ to

$$\mathbf{r}(t + \Delta t) = \mathbf{r}(t) + \mathbf{\Gamma} \cdot \mathbf{r}(t)\Delta t + \delta\mathbf{r}(t) \tag{4.1}$$

61

while their orientations were changed from $\hat{\mathbf{u}}(t)$ to

$$\hat{\mathbf{u}}(t+\Delta t) = \hat{\mathbf{u}}(t) + [\hat{\mathbf{I}} - \hat{\mathbf{u}}(t)\hat{\mathbf{u}}(t)] \cdot \boldsymbol{\Gamma} \cdot \hat{\mathbf{u}}(t)\Delta t + \delta\hat{\mathbf{u}}(t) , \qquad (4.2)$$

where $\boldsymbol{\Gamma}$ is a matrix with $\Gamma_{xy} = \dot{\gamma}$ and all remaining elements equal to zero and $\hat{\mathbf{I}}$ is the unit matrix. The random displacements and reorientations were drawn according to

$$\langle \delta\mathbf{r}(t)\delta\mathbf{r}(t) \rangle = 2k_B T \boldsymbol{\Xi}^{-1}(t)\Delta t , \qquad (4.3)$$

$$\langle \delta\hat{\mathbf{u}}(t)\delta\hat{\mathbf{u}}(t) \rangle = 2k_B T \gamma_r^{-1} \left[\hat{\mathbf{I}} - \hat{\mathbf{u}}(t)\hat{\mathbf{u}}(t) \right] \Delta t , \qquad (4.4)$$

where

$$\boldsymbol{\Xi} = \gamma_\parallel \hat{\mathbf{u}}(t)\hat{\mathbf{u}}(t) + \gamma_\perp \left[\hat{\mathbf{I}} - \hat{\mathbf{u}}(t)\hat{\mathbf{u}}(t) \right] , \qquad (4.5)$$

$$\gamma_r = \frac{\pi \eta_s L^3}{3\ln(L/D)} , \qquad (4.6)$$

$$\gamma_\parallel = \frac{2\pi \eta_s L}{\ln(L/D)} , \qquad (4.7)$$

$$\gamma_\perp = 2\gamma_\parallel , \qquad (4.8)$$

with η_s the viscosity of the solvent and T the temperature. Equation (4.6) is sufficiently accurate for the large aspect ratios used in this Chapter. After each time step all pairs were checked for possible overlaps. For each overlapping pair, the collision time $t + \lambda_c \Delta t$ was detected by interpolation between t and $t + \Delta t$ using the already chosen random displacements and reorientations, but with Δt replaced by $\lambda_c \Delta t$. Next the pair was propagated to the point of contact and the remaining part of the time step was completed in a similar way. Results of simulations at low volume fractions were in excellent agreement with those of previous simulations [133] using conventional Brownian dynamics using stiff potential interactions to prevent overlaps between the rods. The current code, however, is more efficient and can be operated at higher densities and larger aspect ratios.

In Fig. 4.1 we present four snapshots of a simulation box containing 1750 rods with aspect ratio $L/D = 25$ at a volume fraction φ determined by $L\varphi/D = 3.5$. For all simulations discussed in this Letter the diameter $D = 0.0148 \mu$m, so the length $L = 0.37 \mu$m in this case. The solvent is always water with viscosity $\eta_s = 1$ mPa s and temperature T $= 300$ K. A time step Δt was chosen equal to 0.5μs.

The boxes shown in Fig. 4.1 were sheared with shear rate $\dot{\gamma} = 125$s^{-1}. In frame **a** the rods are on average aligned along the flow direction. Half of each rod is light grey, the other
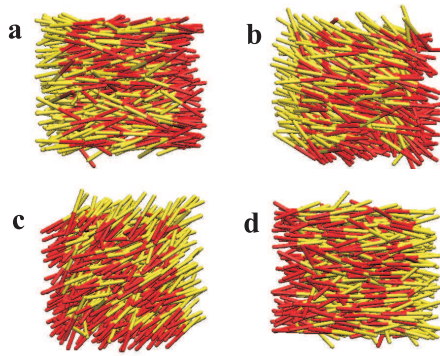
Figure 4.1: *Snapshots of a simulation box with rods collectively changing orientation by 180 degree. The four snapshots are taken at the times indicated as **a**, **b**, **c** and **d** respectively in the upper part of Fig. 4.2. The box contains 1750 rods of which only 500 are shown in each frame, so the density is 3.5 times as high as appears from the pictures.*

half dark grey. The colouring is chosen such that for each rod in frame **a** the dark part is to the right of the light part. As time advances the rods collectively rotate such that the dark parts point southeast in frame **b** and southwest somewhat later in frame **c**. Finally in frame **d** the rods are aligned along the flow direction again, but now with their dark parts to the left of the light parts, *i.e.*, they made a turn of 180° around the *z*-axis. Since the particles are symmetric, this state is indistinguishable from the original state **a**. We stress that the tumbling of the rods is not the result of a rotation of the whole box, but that it is really a rotation of the individual rods performed collectively, without appreciably changing position except along the flow direction.

The details of the motion can hardly be seen from a time-series of snapshots like in Fig. 4.1. Therefore we plot in Fig. 4.2 the three components $\hat{n}_x$, $\hat{n}_y$ and $\hat{n}_z$ of the director $\hat{\mathbf{n}}$ together with the order parameter as a function of time. At each time the order tensor $\mathbf{S}(t) = N^{-1}\sum_i \hat{\mathbf{u}}_i(t)\hat{\mathbf{u}}_i(t)$ was calculated and diagonalised. The eigenvector with the largest eigenvalue λ, $\frac{1}{3} \leq \lambda \leq 1$, is the director $\hat{\mathbf{n}}(t) = \hat{n}_x(t)\hat{\mathbf{e}}_x + \hat{n}_y(t)\hat{\mathbf{e}}_y + \hat{n}_z(t)\hat{\mathbf{e}}_z$ and is characteristic for the average direction of the long axes of the particles. The corresponding eigenvalue is correlated to the scalar order parameter $P_2 = (3\lambda - 1)/2$, which is equal to zero if the rods have random orientations and equal to one in case the rods are all pointing in the same
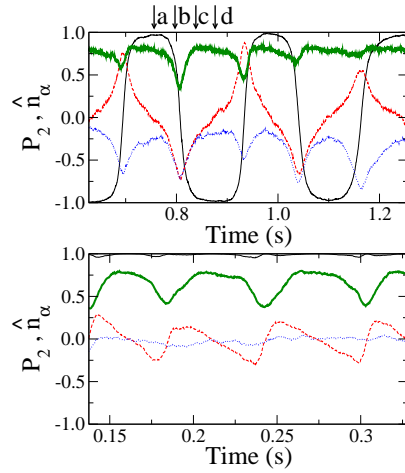
Figure 4.2: *Order parameter P_2 (thick solid line) and director components $\hat{n}_x$ (solid), $\hat{n}_y$ (dashed) and $\hat{n}_z$ (dotted) as a function of time. The upper and the lower figures illustrate the kayaking and wagging motions, respectively. In this figure are also indicated the times at which the snapshots in the upper part of Fig. 4.1 were taken.*

direction. The *x*-component of the director is seen to periodically change from $+1$ to -1 and back again. This confirms what we inferred from inspection of Fig. 4.1.

More interesting is the time evolution of $\hat{n}_y$ and $\hat{n}_z$. At those time spans when $\hat{n}_x$ is changing from $+1$ to -1 or the other way round, $\hat{n}_z$ drops from about -0.25 to about -0.75 and returns to -0.25 again. At the same time $\hat{n}_y$ alternatingly drops from zero to about -0.75 and returns to zero or rises from zero to $+0.75$ in order to return to zero again. This behavior is indicative of the motion called kayaking. Note that the motion is such that the average orientation remains to be along the flow direction for a while and that the actual flip to the reverse orientation occurs during a rather short time span. The results presented in this figure and elsewhere in this Chapter have been confirmed with simulation boxes with volumes twice, four and eight times as large as the present one.

We now summarize our findings on the basis of a large number of simulations with L/D ranging from 20 to 60 for two values of $L\varphi/D$ and $\dot{\gamma}$ ranging from 30 to 1000 s^{-1}. At low shear rates and for all initial conditions except when initially the director is aligned along the vorticity direction, the system ends up kayaking with a period which depends on $\dot{\gamma}$ and on
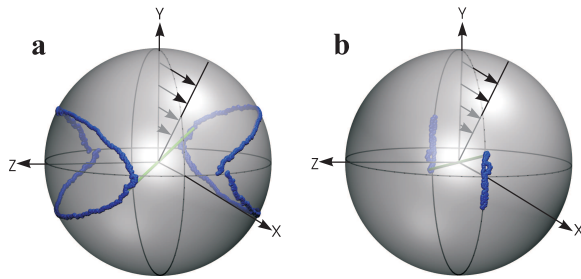
Figure 4.3: *The path on the unit sphere traced out by the director of a kayaking (**a**) and wagging (**b**) box of rod-like particles with L/D = 25 and Lφ/D = 3.5. The arrows attached to the y-axis represent the flow field.*

$L\varphi/D$. In particular tumbling turns out to be unstable with respect to kayaking except maybe for the smallest aspect ratio. A picture of the path traced out by the director during one period is drawn in Fig. 4.3**a** as well as in the upper part of Fig. 4.2. At intermediate shear rates and for the same initial conditions, the director moves towards the shear plane in order to perform a wagging motion, as illustrated in the lower part of Fig. 4.2 and Fig. 4.3**b**. The small value of $\hat{n}_z$ indicates an in-plane motion and the alternation of $\hat{n}_y$ around zero denotes the wagging along the shear direction. There seems to be no abrupt change of the period at the kayaking-to-wagging transition. At even higher shear rates the director gets arrested in the shear plane making a nonzero angle with the *x*-axis. In case the director initially starts along the vorticity direction, it ends up performing small rotations around its initial direction. At high enough shear rates, this state becomes unstable and the director moves towards the shear plane where it gets arrested in the same unique state, for the given shear rate, where all other systems end. So it turns out that the results obtained so far are in qualitative agreement with the predictions of the Doi-Hess theory. Many more simulations will be needed to construct a phase diagram as has been done on the basis of the Doi-Hess equation [44, 45, 62, 76].

As a quantitative test of our simulation method, we plot in Fig. 4.4 the tumbling time T as a function of shear rate $\dot{\gamma}$ for all simulations with $L\varphi/D = 4.5$. In the same plot we present experimental results on the *fd* virus [91], which has an effective diameter equal to the one that we have used and for which $L/D = 60$. Using a molar weight of $1.64 \times 10^7 \text{g/mol}$
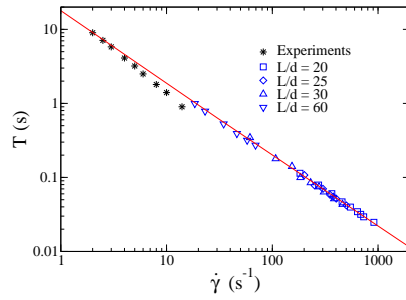
Figure 4.4: *Simulated and experimental tumbling times T as a function of the shear rate $\dot{\gamma}$ at a volume fraction φ determined by $L\varphi/d = 4.5$. Experiments were done [91] on the fd virus for which $L/D = 60$ and $D = 0.0148 \, \mu$m like in our simulations.*

[88], our simulations correspond to a density of 13.6 mg/ml while the experimental density is 13 mg/ml. Our results, when extrapolated to the experimental shear rates, are larger than the experimental ones by a factor of at most 1.5. Since the *fd* virus is slightly flexible, the tumbling periods are expected to be smaller [55] than those of the stiff particles which were used in the simulations, hence, we consider the agreement good. It will be interesting to investigate if the difference between the slopes of the experimental and the simulated curves may also be attributed to this difference in flexibility. As a second test we mention that for $L/D = 60$, the transition from kayaking to wagging was found to occur between $\dot{\gamma} = 27.8$ and 30.1 s^{-1}, whereas the experimental transition occurs at $\dot{\gamma} \approx 30 \text{ s}^{-1}$ when the density is 14 mg/ml [91].

The preliminary results described in this Chapter can be regarded as an Introduction to the much detailed investigation of the collective periodic orientational motions of the director in nematic solutions of rigid rods. In *Chapter* 5, we'll present the dependence of the kayaking period on the aspect ratio, the volume fraction as well as the applied shear rate. The simulation results will be compared with both theoretical predictions and experimental observations. Furthermore, transitions between different types of motions are under investigation.

5 Periodic orientational motions of rigid liquid-crystalline polymers in shear flow

The collective periodic motions of liquid-crystalline polymers (LCPs) in a nematic phase in shear flow have, for the first time, been simulated at the particle level by Brownian dynamics simulations. A wide range of parameter space has been scanned, by varying the aspect ratio L/D between 10 and 60 at three different scaled volume fractions $L\varphi/D$ and an extensive series of shear rates. The influence of the start configuration of the box on the final motion has also been studied. Depending on these parameters, the motion of the director is either characterized as tumbling, kayaking, log-rolling, wagging or flow-aligning. The periods of kayaking and wagging motions are given by $T = 4.2 \frac{L}{D}\varphi\dot{\gamma}^{-1}$ for high aspect ratios. Our simulation results are in agreement with theoretical predictions and recent shear experiments on fd viruses in solution. These calculations of elongated rigid rods have become feasible with a newly developed event-driven Brownian dynamics algorithm. [*]

5.1 Introduction

The flow instability of liquid-crystalline polymers (LCPs) has been studied both theoretically and experimentally since the sixties of the last century [38, 46, 49, 78, 79, 89, 102, 117]. The continual interest in this topic is not only because of the importance of LCPs in technical applications, but also due to some fascinating rheological phenomena such as the oscillating

---

[*] The work described in this chapter previously appeared in J. Chem. Phys., In Press (2006).

response of nematic liquid crystals to steady driving forces, *e.g.*, shear forces [41, 43, 44, 45, 55, 57, 62, 76, 83, 81, 82, 119, 120, 144]. A molecular theory of the orientational motions of LCPs in shear flow was first formulated by Hess [59] and Doi [33], both for the isotropic phase as well as for the liquid crystalline phase. Later on, Marrucci and Maffettone [96, 97, 98, 99] analyzed the Doi-Hess model numerically by restricting the orientational distribution function (ODF) to two dimensions, while Larson and Öttinger [80, 84] studied this model by expanding it in spherical harmonics. Their findings showed that the director of a nematic phase exhibits tumbling, kayaking, wagging, flow-aligning or log-rolling motions, depending on the particular value of the shear rate. An important step was made when Kröger and Sellers [77] and Archer and Larson [6] predicted the dependence of the tumbling period on the scalar second and fourth order parameters. For a lot of valuable information and references, we refer to the papers of Kröger and Hess [62, 76] and Forest *et al.* [44, 45].

The central objective of all theories has been the investigation of the time evolution of the orientational order parameter tensor

$$\mathbf{S} = \langle \hat{\mathbf{u}}\hat{\mathbf{u}} \rangle \ , \tag{5.1}$$

where $\hat{\mathbf{u}}$ is the unit vector along the long axis of the rod and the brackets denote ensemble averaging. The unit eigenvector $\hat{\mathbf{n}}$ of $\mathbf{S}$ corresponding to the largest eigenvalue S represents the average direction of the rods, and is known as the "director" of the system. The scalar order parameter, defined as $P_2 = (3S - 1)/2$, measures the degree of nematic order of the system. P_2 is zero in an isotropic state and becomes unity in the state of perfect alignment. According to the Doi-Hess theory, which was recently re-derived by Dhont and Briels [24] on the basis of the N-particle Smoluchowski equation, the time evolution of the orientational order tensor is governed by

$$\frac{d}{dt}\mathbf{S} = -6\mathrm{D}_r \left\{ \mathbf{S} - \frac{1}{3}\hat{\mathbf{I}} + \frac{5}{4}\frac{L}{D}\varphi(\mathbf{S}^{(4)} : \mathbf{S} - \mathbf{S}\cdot\mathbf{S}) \right\} + \dot{\gamma}\left\{ \hat{\mathbf{\Gamma}}\cdot\mathbf{S} + \mathbf{S}\cdot\hat{\mathbf{\Gamma}}^T - 2\mathbf{S}^{(4)} : \hat{\mathbf{E}} \right\} \ . \tag{5.2}$$

Here D_r stands for the rotational diffusion coefficient of a single non-interacting rod with length L and thickness D. $\hat{\mathbf{I}}$ is the unit tensor and φ denotes the volume fraction of rods. $\dot{\gamma}$ denotes a shear rate and $\hat{\mathbf{\Gamma}}$ is the unit velocity gradient matrix (in the current study $\hat{\mathbf{\Gamma}} = \hat{\mathbf{e}}_x\hat{\mathbf{e}}_y$). $\hat{\mathbf{E}} = \frac{1}{2}[\hat{\mathbf{\Gamma}} + \hat{\mathbf{\Gamma}}^T]$, with the superscript T denoting a transposition. The fourth order tensor is defined as $\mathbf{S}^{(4)} = \langle \hat{\mathbf{u}}\hat{\mathbf{u}}\hat{\mathbf{u}}\hat{\mathbf{u}} \rangle$. We will comment on this equation later, in sections 5.3 and 5.4.

Recent mechanical and rheo-optical experiments [14, 56, 103, 105] on LCPs (in this case, a lyotropic solution of polybenzylglutamate in *m*-cresol) show periodic responses to low and intermediate shear flows but an irregular response to high shear flow. A very recent experimental investigation [91] on solutions of *fd* viruses (rod-like biopolymers with aspect ratio $L/D = 60$) also revealed periodic motions in nematic phases in weak shear flow. Obviously, computer simulations might have helped a great deal in confirming and testing the theoretical predictions. Unfortunately, only very few of these investigations have been done so far. Computer simulations performed by Yamane *et al.* [142, 143] were limited to dilute and semi-dilute solutions. Ding and Yang [28, 29] carried out two-dimensional Brownian dynamics simulations on solutions of rigid rods in steady shear flow, but the translational motions were not taken into account. Recently, three-dimensional simulations were carried out on ellipsoids in shear by Mori *et al.* [106], but the low aspect ratio ($L/D = 3$) used by them makes it difficult to compare their results with those of theories or experiments on LCPs. To the best of our knowledge, no 3-D computer simulations have been done on concentrated rod-like LCPs of large aspect ratios under shear. We therefore set out to apply our newly developed event-driven Brownian dynamics algorithm [129, 132] to test the theoretical predictions and compare with experimental findings.

This Chapter is organized as follows. After this introductory section, the algorithm of the event-driven technique is briefly described in section 5.2. Some simulation results and the corresponding discussions are presented in sections 5.3, 5.4 and 5.5. Finally, we conclude our findings with a summary in section 5.6.

5.2   Simulation method

The Brownian rods are suspended in a Newtonian liquid with a stationary velocity field $\mathbf{V}(\mathbf{r}) = \mathbf{\Gamma} \cdot \mathbf{r}$, where $\mathbf{\Gamma} = \dot{\gamma} \hat{\mathbf{e}}_x \hat{\mathbf{e}}_y$ is the velocity gradient tensor and $\mathbf{r}$ is the position vector of a point in the simulation box. This velocity field corresponds to a simple shear flow in the *x*-direction, with a gradient in the *y*-direction. The Langevin equations of motion for the translation and rotation of the Brownian rods with aspect ratio L/D are solved on the Smoluchowski (diffusive) time scale. The positions $\mathbf{r}$ and orientations $\hat{\mathbf{u}}$ of all rods are therefore updated every timestep by a displacement sampled from a Gaussian distribution, without in-

tervention of the corresponding velocities. With the Itô interpretation that we employ, this propagator gives rise to the N-particle Smoluchowski equation which is considered to be the fundamental equation of motion for the probability density function [13, 22, 24, 36, 133]. Detailed descriptions can be found in our previous publications [133].

In the present Brownian dynamics simulations, an event-driven technique is employed to take the excluded volume interactions between the rigid, long and thin rod-like particles into account. Inspired by the molecular dynamics simulations of hard spherical particles by Alder and Wainwright [1], we prevent the overlap between two solute spherocylindrical colloids by detecting the moment and the position of the collision and then applying random displacements and reorientations (sampled from similar Gaussian distributions as used in the non-collisional time steps) to separate them from the colliding position. This algorithm is rather distinguished from most commonly used Brownian dynamics simulation methods where a repulsive potential is employed to avoid overlaps between hard particles. The great advantage of the present simulation algorithm is that it can efficiently handle concentrated systems of elongated particles in shear flow, which is extremely difficult for ordinary simulation methods. We refer the reader to our previous work [129, 132] for a more extensive discussion of the algorithm and its implementation.

Our simulation systems are modeled after the *fd* virus [30, 88]. In order to set the scales, necessary to calculate translational and rotational diffusion coefficients which involve L and D separately, we put D equal to 14.8 nm and use L/D as an independent parameter. Water is used as the solvent, with viscosity $\eta_s = 10^{-3}$ Pa s. Using hydrodynamics, the rotational diffusion coefficient then becomes [22]

$$\mathrm{D}_r = \frac{3k_B T \ln(L/D)}{\pi \eta_s L^3} \, , \tag{5.3}$$

where the temperature T is always 300 K and k_B is Boltzmann's constant. The timestep $\delta t = 0.5\,\mu$s used in all simulations is on the safe side [129, 132], yet 10 times larger than that used in our previous simulations [133] with soft repulsive interactions between rods. Cubic boxes are employed with periodic boundary conditions in each dimension. The volumes of the boxes are chosen according to $\frac{V}{L^3} = c\frac{\pi}{4}(\frac{L}{D})^{-1}$ with $c = 500$ for $L/D \leq 40$, $c = 750$ for $L/D = 50$ and $c = 1000$ for $L/D = 60$. By doing so, the edges of the boxes are always $2.5 \sim 3$ times as long as the length of the rods. With $\varphi = \frac{\pi}{4}\frac{N}{V}D^2 L$, the volume fraction of rods, the number of particles in the box $N = cL\varphi/D$ ranges from 1750 to 4500. This is a convenient

expression since $L\varphi/D$ roughly measures the mean field potential felt by the individual rods due to the hard repulsive interactions with the surrounding rods, and therefore is the parameter that we want to vary. Typically the simulations take about a month of CPU time on $2.4 - 3.0$ GHz Pentium IV's, with several runs at high L/D and low $\dot{\gamma}$ requiring up to half a year, to complete a couple of periods.
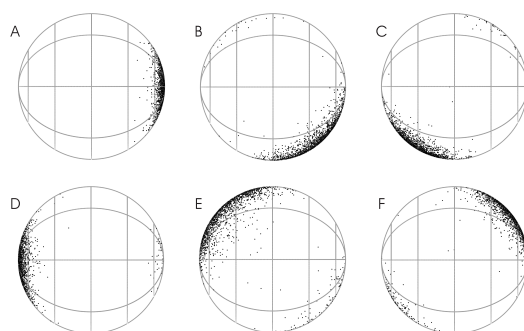
5.3 Results at low and intermediate shear rates

5.3.1 Tumbling and kayaking

Figure 5.1: *Snapshots of the normalized end-to-end vectors of rigid rods in shear flow, plotted as dots on the surface of a unit sphere. The flow direction, which is also the initial orientation of every rod, runs from the left pole to the right pole. Drawn lines represent meridians and parallels. A 2π tumbling/kayaking motion is represented by the snapshots A to F, which are not evenly spaced in time. The simulation box contains 1750 rods with aspect ratio $L/D = 25$, at a scaled volume fraction of 3.5 and an applied shear rate $\dot{\gamma} = 125 \text{ s}^{-1}$. Note that gradually a small secondary cluster develops, diametrically opposed to the main cluster, of rods that have individually flipped from parallel to antiparallel to the director.*

At sufficiently high volume fractions, spherocylinders organize themselves into a nematic state whose director is observed to perform periodic motions in shear flow. Snapshots from a Brownian dynamics simulation, shown in Fig. 1 of Ref. 129, clearly reveal the collective character of the orientational motion of individual rods. In this Chapter, we will visualize

71

this periodic motion by plotting the time evolution of the normalized end-to-end vectors on the surface of a unit sphere. Fig. 5.1 shows six snapshots of such a sphere, viewed along the vorticity direction. These snapshots describe a 2π-tumbling motion, caused by the shear flow. In frame A, the end-to-end vectors (shown as black dots) are located in the area of the sphere where the x-components are about $+1$. As time advances, these black dots move to the left along the surface of the unit sphere, representing a tumbling motion of the rods. In frame D most dots are located in the region where the x-components of the end-to-end vectors are about -1, meaning that the rods made a turn of 180° around the vorticity axis. Note that in frame D some dots are located at the right-hand side of the unit sphere, indicating that some rods tumble independently from the majority. A second 180° rotation can be inferred from the sequence of D to F. In the following we adhere to the experimental convention by referring to a 180° tumbling as one period.
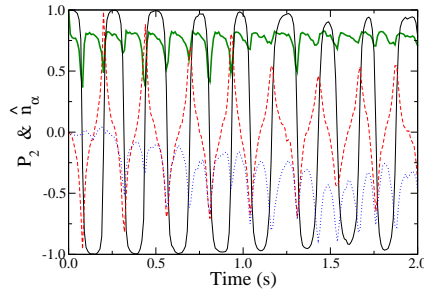

Figure 5.2: *The scalar order parameter P_2 (thick solid line) as well as the three components $\hat{n}_x$ (solid), $\hat{n}_y$ (dashed) and $\hat{n}_z$ (dotted) of the director as functions of time. The $\hat{n}_z$ component reveals how the motion of an initially flow-aligned system evolves from in-plane tumbling to out-of-plane kayaking.*

The collective periodic motions of the individual rods can accurately be described by the time evolution of the scalar order parameter P_2 together with the three components of the director, $\hat{n}_\alpha$. An example is given in Fig. 5.2, applying to a system in which the aspect ratio L/D and the scaled volume fraction $L\varphi/D$ of rods are equal to 25 and 3.5, respectively. The rods are initially perfectly aligned along the shear direction, *i.e.*, the x-direction. A low shear rate $\dot{\gamma} \approx 75$ s^{-1} is chosen, giving a rotational Peclet number Pe$_r = \dot{\gamma}/D_r$ equal to 0.3. The

x-component of the director, represented by a solid line, oscillates between $+1$ and -1 with roughly constant period, while the *y*-component, represented by a dashed line, changes its sign from negative to positive with the same period. The maximum absolute values of $\hat{n}_y$ occur when $\hat{n}_x$ becomes zero, while $\hat{n}_y$ becomes zero when $\hat{n}_x$ comes to its extremum. This behavior is characteristic of periodic tumbling of the director from one flow aligned state to another. During the first two periods, say before 0.3 seconds, $\hat{n}_z$ oscillates with extremely small amplitude around zero, indicating an in-plane tumbling motion. As time goes by, $\hat{n}_z$ develops a periodically changing nonzero value, indicating that the in-plane tumbling motion becomes unstable and is replaced by a periodic out-of-plane motion called kayaking.
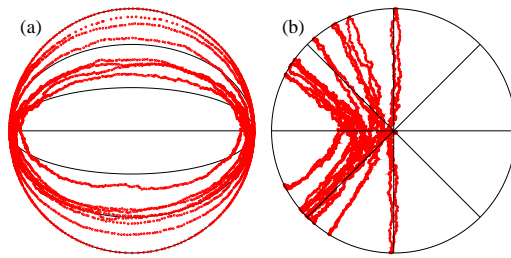

Figure 5.3: *The path traced out by the director* $\hat{\mathbf{n}}$ *of Fig. 5.2 on the surface of a unit sphere as seen along the vorticity (a) and flow (b) direction. The in-plane tumbling motion, characterized by a circle in (a) and a vertical line in (b), turns into an out-of-plane kayaking motion, illustrated by an ellipse in (a) and a* $>$-*shaped path in (b).*

In order to better understand the kayaking motions, we have traced out the path of the director on the unit sphere and plotted the results in Fig. 5.3. Viewed along the *z*-direction, as shown in Fig. 5.3(a), the path initially runs along the unit circle, indicating an in-plane tumbling motion. When next the transformation from tumbling to kayaking occurs, the trace changes from circles to ellipses. Fig. 5.3(b) presents further information to that shown in (a) by viewing the sphere along the *x*-direction. The in-plane tumbling can be easily recognized from the motion of $\hat{n}_y$ between $+1$ and -1 while $\hat{n}_z$ remains zero. After that, the gradual shift of $\hat{n}_z$ from zero to negative values reveals the change from tumbling to kayaking. Obviously, the *z*-component of the director does not always change from zero to negative values; it may just as well adopt positive values. Sometimes it even flips from negative to positive values or

vice versa.

Our results confirm the theoretical findings of Faraoni *et al.* [41] who numerically solved the Doi-Hess equation governing the time evolution of the single particle orientational probability distribution. They indeed found that in-plane tumbling is always unstable with respect to out-of-plane kayaking.

5.3.2 Shear rate and volume fraction dependence of the tumbling and kayaking period
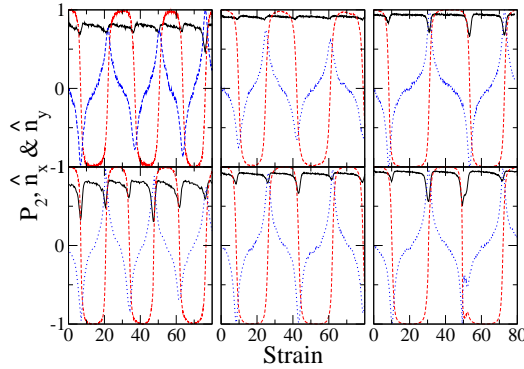

Figure 5.4: *The scalar order parameter P_2 (solid lines) and the x (dashed) and y (dotted) components of the director as functions of elapsed strain. From left to right the scaled volume fractions $L\varphi/D$ are 3.5, 4.0 and 4.5 at fixed $L/D = 20$, while from bottom to top the shear rate doubles.*

An important feature of tumbling and kayaking motions is that their periods remain roughly constant during the complete runs. Since the collective character of the kayaking motion is a result of the excluded volume interaction between the rods, it is to be expected that the kayaking period T depends on the scaled volume fraction $L\varphi/D$, measuring the strength of the average interaction. The shear rate dependence of T may be guessed by assuming that the phase of the motion depends on the elapsed strain, more than on the elapsed time. In order to test these hypotheses we have plotted in Fig. 5.4 the scalar order parameter, and the *x* and *y* components of the director for three values of $L\varphi/D$ and two different shear

rates, all referring to the case $L/D = 20$. The three volume fractions are each well above the isotropic to nematic phase transition [132] as evidenced by the fact that the scalar order parameter P_2 is close to unity in all cases. It is evident from Fig. 5.4 that for all given volume fractions, kayaking indeed takes place in proportion to the elapsed strain, independent of the precise shear rate. This feature is in good agreement with both theoretical predictions [24, 80] and experimental finding [105], and indicates that the dimensionless period $P = T\dot{\gamma}$ is independent of shear rate. Comparing columns in Fig. 5.4, it is found that the more concentrated the system, the less oscillations are made within the same elapsed strain. In Fig. 5.5, we put the statements just made to a quantitative test by plotting the dimensionless period P as a function of $\dot{\gamma}$ for three different values of $L\varphi/D$, all with $L/D = 20$. Within realistic error bounds, P is indeed independent of $\dot{\gamma}$ and only depends on $L\varphi/D$.
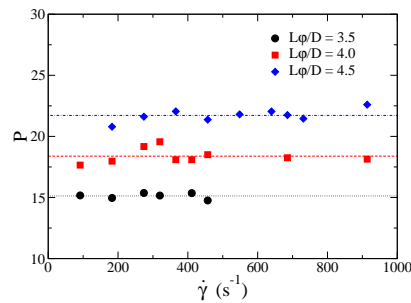

Figure 5.5: *The dimensionless kayaking periods P for $L/D = 20$ as functions of shear rate. Horizontal lines are averages over the simulations corresponding to $L\varphi/D = 3.5$, 4.0 and 4.5, respectively.*

In order to deduce the dependence of the kayaking period T on the aspect ratio L/D, and to expand the above discussed dependence on the scaled volume fraction $L\varphi/D$ and the applied shear rate $\dot{\gamma}$, we simulated about 100 systems with various values of these parameters. Shape anisotropies L/D ranged from 10 to 60, volume fractions were chosen to be $L\varphi/D = 3.5$, 4.0 and 4.5, respectively, and the applied shear rates ranged from $\dot{\gamma} = 20$ to 2000 s^{-1}. First, we plot the kayaking periods T as a function of shear rate $\dot{\gamma}$ on log-log scale. The dotted, dashed and solid lines in Fig. 5.6 are linear fits to the simulation results with volume fractions $L\varphi/D = 3.5$, 4.0 and 4.5, respectively. The power law exponent of each line is very
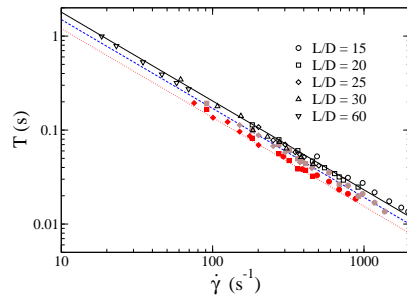
Figure 5.6: *The dependence of the kayaking period T on the aspect ratio, the scaled volume fraction and the applied shear rate. Solid, grey and open symbols represent $L\varphi/D = 3.5$, 4.0 and 4.5, respectively.*

close to -1, indicating that $T \propto \dot{\gamma}^{-1}$, in agreement with the results in Fig. 5.5. Moreover, it is evident from Fig. 5.6 that for a given scaled volume fraction $L\varphi/D$, all measured periods T against shear rate $\dot{\gamma}$ can be fitted by the same straight line independent of the aspect ratio L/D. Only the results for $L/D = 15$ diverge a little bit from the fitting lines at high shear rates. We have omitted the results for $L/D = 10$ because of even larger deviations from the fitting lines.
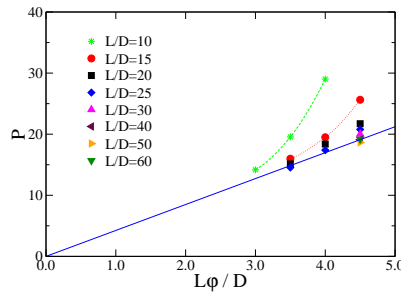

Figure 5.7: *The dimensionless kayaking period P as a function of $L\varphi/D$, for various aspect ratios L/D in a range from 10 to 60. The simulation results are seen to converge with increasing L/D to the master curve of Equation (5.4), shown as a solid line.*

In Fig. 5.7, we plot the dimensionless period P as a function of $L\varphi/D$ in order to deduce

the relationship between the kayaking period and the scaled volume fraction. Again, for short rods ($L/D = 10$ or 15) the results deviate substantially from those for longer rods, which gradually approach a linear master curve described by

$$T = 4.2 \, \frac{L}{D} \, \varphi \, \dot{\gamma}^{-1} \; . \tag{5.4}$$

An initial linear fit resulted in an intercept which was zero within statistical errors. The fit in the above equation was obtained by putting the intercept exactly equal to zero.

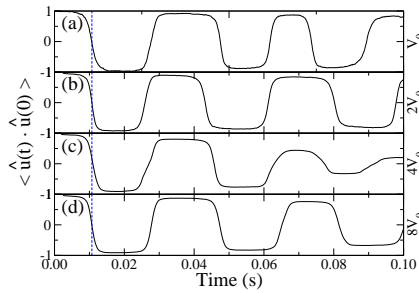### 5.3.3 Finite size analysis

Figure 5.8: *The correlation $\langle \hat{\mathbf{u}}(t) \cdot \hat{\mathbf{u}}(0) \rangle$ between rods' end-to-end vector at time 0 and at time t, in cubic simulation boxes with volumes twice (b), four times (c) and eight times (d) as large as the standard box size (a), respectively. In all four systems, $L/D = 10$, $L\varphi/D = 3.5$ and $\dot{\gamma} = 1124 \; s^{-1}$. For comparison reasons, the origins of time were shifted to make the first occasions of $\hat{n}_x = 0$ coincide (dashed line).*

Before comparing our simulation results with those obtained with theories and experiments, we briefly investigate their dependence on the size of the simulation boxes. Our main interest is to test if the periodic motion and the corresponding periods found in our simulation boxes are inhibited or facilitated by the periodic boundary conditions of our simulations, or if they are real bulk properties. To this end, we have run several simulations with simulation boxes of twice, four times and eight times the volume of our standard simulation box. Since simulation times grow dramatically with the aspect ratio L/D, and obviously also with the system size, we have chosen to perform these tests on solutions of rods with aspect ratio equal

to 10. Instead of plotting the components of the director as a function of time, we now plot $\langle \hat{\mathbf{u}}(t) \cdot \hat{\mathbf{u}}(0) \rangle$ with $\hat{\mathbf{u}}(0)$ being the rod's direction at the beginning of the simulation; note that $\langle \hat{\mathbf{u}}(t) \cdot \hat{\mathbf{u}}(0) \rangle$ is not the usual autocorrelation function. The initial direction of all rods was chosen to be along the flow direction, *i.e.*, $\hat{\mathbf{u}}(0) = \hat{\mathbf{e}}_x$. As a result, $\langle \hat{\mathbf{u}}(t) \cdot \hat{\mathbf{u}}(0) \rangle$ still reveals the periodic motions of the rods by oscillating between positive and negative values, as is shown in Fig. 5.8. Also in Fig. 5.8 we see that the amplitude of this oscillation gradually diminishes with increasing time. This is due to the fact that individual rods occasionally flip their orientation without causing the prevailing director to tumble at the same time. At $t \approx 0.06$ s, in panel (c) only about four fifths of the rods appear to have tumbled collectively, an interpretation that is confirmed by a visual inspection of the box. We conclude from this that the boxes are at the verge of being larger than the correlation length of the collective motion, which together with the fact that the average kayaking period is the same in all boxes, makes us trust that the original boxes with edges of about three rod lengths are sufficiently large to perform these simulations. We refer to the next two subsections for further motivation. For reasons of CPU time we stick with these boxes.

5.3.4 Comparison with theoretical results

In this subsection we compare our simulation results with those of existing theories. Since the director is the main axis of the order tensor $\mathbf{S}$, its time evolution results from that of $\mathbf{S}$ and so is governed by Eq. (5.2). At equilibrium, *i.e.*, when $\dot{\gamma} = 0$, the sum between curly brackets multiplying $6D_r$ in Eq. (5.2) is equal to zero. To a good approximation it may be assumed that in sheared systems this still holds true, or at least that the corresponding term is negligible compared to the term proportional to $\dot{\gamma}$ in Eq. (5.2). The equation of motion for $\mathbf{S}$ then reads

$$\frac{d}{dt}\mathbf{S} = \dot{\gamma}\left\{ 2\hat{\mathbf{E}} \cdot \mathbf{S} + \hat{\omega}^T \cdot \mathbf{S} + \mathbf{S} \cdot \hat{\omega} - 2\mathbf{S}^{(4)} : \hat{\mathbf{E}} \right\} . \tag{5.5}$$

where we have used $\hat{\mathbf{\Gamma}} = \hat{\mathbf{E}} - \hat{\omega}$ with $\hat{\omega} = \frac{1}{2}\{\nabla\hat{\mathbf{u}} - (\nabla\hat{\mathbf{u}})^T\} = -\frac{1}{2}\{\hat{\mathbf{\Gamma}} - \hat{\mathbf{\Gamma}}^T\}$. Using $\mathbf{S} = \frac{1}{3}(1 - P_2)\hat{\mathbf{I}} + P_2\hat{\mathbf{n}}\hat{\mathbf{n}}$, which holds true for uni-axial symmetries (see Appendix B of Ref. 132), and assuming that P_2 does not depend on time, we arrive at

$$\frac{d}{dt}\hat{\mathbf{n}} = \dot{\gamma}\left\{ \hat{\mathbf{n}} \cdot \hat{\omega} + \frac{2}{P_2}\hat{\mathbf{n}} \cdot \left[\frac{1}{3}(1 + 2P_2)\hat{\mathbf{E}} - \mathbf{S}^{(4)} : \hat{\mathbf{E}} \right] \right\} . \tag{5.6}$$

After a lot of algebra this may be shown [77, 6] to be equal to

$$\frac{d}{dt}\hat{\mathbf{n}} = \dot{\gamma}\left\{\hat{\mathbf{n}}\cdot\hat{\omega} + \lambda\left[\hat{\mathbf{E}}\cdot\hat{\mathbf{n}} - \hat{\mathbf{E}}:\hat{\mathbf{n}}\hat{\mathbf{n}}\hat{\mathbf{n}}\right]\right\} , \tag{5.7}$$

where λ, the tumbling parameter, will be given below. Eq. (5.7) admits periodic solutions [82] only when λ is smaller than one; the period of this motion is

$$T = \frac{2\pi}{\dot{\gamma}\sqrt{1-\lambda^2}} . \tag{5.8}$$

From the above approach, the tumbling parameter is found to be given by

$$\lambda \quad = \quad \frac{14 + 5P_2 + 16P_4}{35P_2} , \tag{5.9}$$

$$P_2 \quad = \quad \frac{1}{2}\langle 3\left(\hat{\mathbf{u}}\cdot\hat{\mathbf{n}}\right)^2 - 1\rangle , \tag{5.10}$$

$$P_4 \quad = \quad \frac{1}{8}\langle 35\left(\hat{\mathbf{u}}\cdot\hat{\mathbf{n}}\right)^4 - 30\left(\hat{\mathbf{u}}\cdot\hat{\mathbf{n}}\right)^2 + 3\rangle . \tag{5.11}$$

The second of these equations is just an alternative way of expressing $P_2 = (3S-1)/2$, while the last one defines the fourth order scalar parameter.

Instead of trying to approximate P_4 directly, most theorists have done implicitly so by assuming a closure relation expressing $\mathbf{S}^{(4)}:\hat{\mathbf{E}}$ in Eq. (5.5) in terms of the orientational order parameter tensor $\mathbf{S}$. This finally leads to an approximate expression for λ. The most accurate but complicated approximate expression was suggested by Hinch and Leal [65]

$$\lambda = \frac{1}{9P_2}\left\{2 - P_2 + 8(P_2)^2 + \frac{56 + 80P_2}{35}\exp\left[\frac{-6(P_2)^2}{1-(P_2)^2}\right]\right\} . \tag{5.12}$$

In Fig. 5.9 we show the dependence of the dimensionless kayaking period P on the scalar order parameter P_2. The squares were obtained by measuring P from simulations of sheared boxes and P_2 from the corresponding equilibrium simulations. The open circles were obtained by measuring P_4 from the equilibrium simulations as well and by using the theory of Larson *et al.* [82], Eqs. (5.8) $-$ (5.11). The very good agreement between these two approaches strongly supports Eq. (5.8), and indicates that the orientational probability distribution hardly changes under shear. The dashed line in Fig. 5.9 results from applying Hinch and Leal's approximation [16, 65]. It is seen that, at least for the calculation of kayaking periods, this approximation works rather well.

It is appropriate to comment on the above results. We have seen that the general theory, as long as no closure relations are invoked, works reasonably well. This is evidenced by the
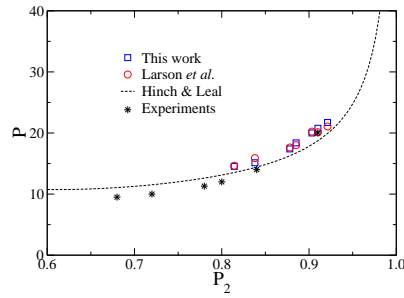
Figure 5.9: *The dimensionless kayaking period P as a function of the scalar order parameter* P_2*. Solid squares denote the direct measurements in this work. Open circles represent calculated periods using the theory of Larson* et al. *[82], Eqs. (5.8) to (5.11), based on* P_2 *and* P_4 *from equilibrium simulations. The dashed curve shows a calculation of P on the basis of* P_2 *alone, proposed by Hinch and Leal [65]. Experimental measurements by Lettinga* et al. *[91] are expressed as stars.*

fact that the squares and circles in Fig. 5.9 coincide. Besides the approximations involved in deriving Eq. (5.2), the theory assumes that (i) the orientational distribution changes little enough to make the thermodynamic term in Eq. (5.2) negligible compared to the shear term, (ii) the distribution remains uni-axial, and (iii) P_2 does not change with time. All these basically mean that the distribution of rods rotates or tumbles, without changing its moments. The first approximation is difficult to test, since the first term on the right-hand side of Eq. (5.2) does not represent thermodynamics very well. It involves several somewhat shaky approximations [24, 133]. A better description of the dynamic correlations would lead to a better term proportional to D_r. Still, this would be equal to zero in the equilibrium situation and put equal to zero in the above approximation. The second approximation mentioned above, *i.e.*, that the distribution remains uni-axial is rather well met during that part of each period when the director is aligned with the flow direction. During the actual tumbling the distribution deviates substantially from being uni-axial. The period, however, is mostly determined by the flow aligned part of each period. The third approximation is also not rigorously true, as can be seen from all our plots so far showing that P_2 varies during the tumbling of the rods. Apparently, this variation is small enough to be negligible.

5.3.5 Comparison with experiments

Recently extensive experiments were done by Lettinga *et al.* [91] on colloidal suspensions of *fd* viruses under shear. In one of their plots they showed kayaking periods as a function of P_2. We have included their results, represented by stars, in Fig. 5.9. It is seen that experimental and simulation results agree reasonably well, particularly at larger values of P_2. The latter correspond to large volume fractions where possibly the semiflexibility of the *fd* virus is less dominant than at lower volume fractions [55].
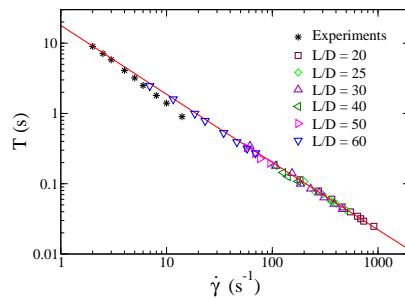

Figure 5.10: *Comparison of the experimental kayaking periods T of the fd virus [91] (stars, $L\varphi/D = 4.4$) and simulation results (open symbols, $L\varphi/D = 4.5$).*

One of the nice aspects of Fig. 5.9 is that it does not involve the diameter of the rods. If we want to compare our predicted kayaking periods with experimental results, however, we need to attribute some numerical value to the effective experimental diameter, which will actually depend on the salt concentration. Following Lenstra *et al.* [88], we have chosen the above mentioned effective diameter of $D = 14.8$ nm; the aspect ratio of the *fd* virus then is 60. Using a molecular weight of 1.64×10^7 g/mol, the experimentally used density of 13 mg/ml corresponds to $L\varphi/D = 4.4$. The experimental periods are shown in Fig. 5.10 as a function of shear rate, together with a large number of simulation results at the value of $L\varphi/D = 4.5$. It is seen that simulations and experiments agree rather well. Obviously, the agreement may be partly due to a lucky choice of the effective diameter. In the next section we will add some extra motivation for this choice. The slight difference in the slopes, *i.e.*, the experimental periods scale as $\dot{\gamma}^{-1.1}$ [91], probably results from the finite flexibility of the *fd* virus [55].

5.4 Results at high shear rate

By solving the Doi-Hess equation, which describes the time dependence of monodomain rigid rod-like colloidal systems, Larson [80] found that with increasing shear rates, nematic systems undergo several transitions between states with qualitatively different director motions. Whereas at low shear rates the director performs a kayaking motion of the kind we described in the previous section, at higher shear rates it performs a motion called wagging, which becomes "arrested" into a flow-aligned state at even higher shear rates [41, 44, 45, 57, 84, 119, 120]. We found similar transitions in our simulations, which we will discuss in this section.
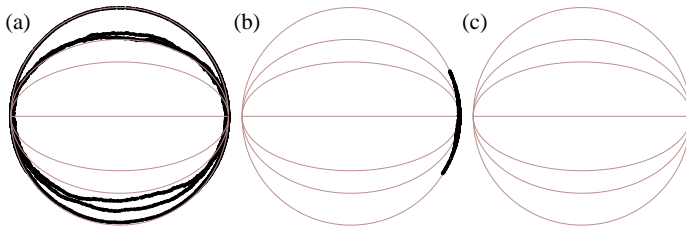
5.4.1 Kayaking to wagging transition

Figure 5.11: *The paths traced out by the directors on unit spheres (viewed along the vorticity direction) at shear rates of* 75 *(a),* 250 *(b) and* 2500 s^{-1} *(c).* $L/D = 25$ *and* $L\varphi/D = 3.5$.

In Fig. 5.11, we represent the paths traced out on the unit sphere by directors of nematic systems with $L/D = 25$ and $L\varphi/D = 3.5$ for different shear rates. The view is along the vorticity axis. Fig. 5.11(a) refers to a shear rate of 75 s^{-1} and it is seen that during the part of the run represented in the figure, the motion changes from tumbling to kayaking similar to our results in the previous section. Fig. 5.11(b) shows the results when $\dot{\gamma} = 250$ s^{-1}. Obviously, at this shear rate the director performs a completely different type of motion than at the lower shear rate. In agreement with theoretical predictions, it is located in the shear plane and symmetrically oscillates about the flow direction. At even higher shear rates, like $\dot{\gamma} = 2500$ s^{-1} shown in Fig. 5.11(c), the director gets arrested in the shear plane, making

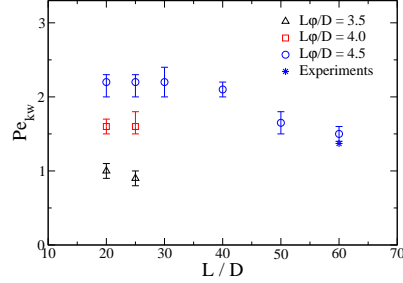a small shear-dependent angle θ with the flow direction. This we will discuss in the next subsection.

Figure 5.12: *The critical rotational Peclet number* $\mathrm{Pe}_{\mathrm{kw}}$ *of the kayaking to wagging transition as a function of aspect ratio for three scaled volume fractions. The experimental result for the fd virus [91], with $L\varphi/D = 4.4$, is shown as a star. See the main text for a discussion of this measurement.*

By performing a large number of simulations at different shear rates, we have found that the transition from kayaking to wagging is rather abrupt, and we have been able to determine the particular shear rate $\dot{\gamma}_{kw}$ at which this transition occurs, for various aspect ratios and volume fractions. The corresponding rotational Peclet numbers $\mathrm{Pe}_{\mathrm{kw}} = \dot{\gamma}_{\mathrm{kw}}/D_r$ are presented in Fig. 5.12 as a function of the aspect ratio L/D for three different values of $L\varphi/D$. Since producing this plot is rather costly, we measured the values of $\mathrm{Pe}_{\mathrm{kw}}$ for large aspect ratios only for the case $L\varphi/D = 4.5$ since this corresponds to the experimental volume fraction that we are interested in. First, for those aspect ratios where we did several volume fractions, it is seen that $\mathrm{Pe}_{\mathrm{kw}}$ depends rather strongly on $L\varphi/D$. Next, for $L\varphi/D = 4.5$ we find that $\mathrm{Pe}_{\mathrm{kw}}$ goes down with increasing aspect ratio beyond $L/D \approx 40$. We cannot infer from our results what will happen in the limit of L/D going to infinity, but it seems reasonable to expect that for large aspect ratios $\mathrm{Pe}_{\mathrm{kw}}$ will drop to very low values. Keeping the diameter finite, this means that for very long rods $\dot{\gamma}_{\mathrm{kw}}$ will go to zero at constant $L\varphi/D$. Finally, the star in Fig. 5.12 represents the result of Lettinga *et al.* [91] on an *fd* suspension of 13 mg/ml. Note that actually the experiment yields $\dot{\gamma}_{\mathrm{kw}}$, so the transition to $\mathrm{Pe}_{\mathrm{kw}}$ involves a choice of the diameter, which in our case is $D = 14.8$ nm. Given the good agreement between simulations and the

experiment, we consider our choice to be fair. It is difficult to be very precise at this point, but notice that a smaller value of D would only slightly diminish D_r and hence the experimental value of Pe_{kw}, while at the same time the experimental system would correspond to a smaller value of $L\varphi/D$ and a larger aspect ratio. The last two changes would substantially change the simulated value of the Pe_{kw} and make the agreement with experiment worse.
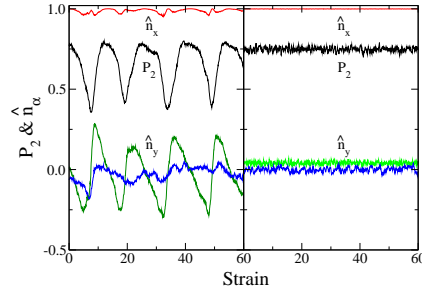

Figure 5.13: *The scalar order parameter P_2 and the three components of $\hat{\mathbf{n}}$ as a function of strain for wagging (left) and flow-aligning (right) motions. The paths of these directors are depicted by Fig. 5.11(b) and (c).*

In the left panel of Fig. 5.13, we have plotted the order parameter P_2 and the components of the director as a function of strain, for the system of Fig. 5.11(b). We see that $\hat{n}_z$ is small and oscillates around zero, indicating an in-plane motion; $\hat{n}_x$ remains close to unity, indicating that no continuous rotation of the director occurs. The wagging type of motion is revealed by the fact that $\hat{n}_y$ oscillates around zero with a substantial amplitude. It is interesting to notice that these oscillations are rather asymmetrical. At the beginning of each period, $\hat{n}_y$ decreases, *i.e.*, the director rotates clockwise when viewed along the vorticity axis, while the distribution becomes broader, as indicated by the fact that P_2 diminishes as well. When P_2 has dropped to about 0.5, the director abruptly changes its motion and rotates quickly counter-clockwise. During this stage, the distribution initially continues to broaden before P_2 rapidly rises as well. Once P_2 has obtained its maximum value again, the director starts to gradually rotate clockwise again and the whole procedure repeats itself. These findings are in agreement with theoretical predictions by Larson [80]. By calculating the periods of the wagging motion for various aspect ratios, scaled volume fractions and shear rates, we recover the same functional

dependence as for the kayaking motion, *i.e.*, Eq. (5.4) applies also to a wagging director. These periods have therefore been added to Figs. 5.6 and 5.10, where it is clear that both kayaking and wagging periods coalesce to a single line for every scaled volume fraction.
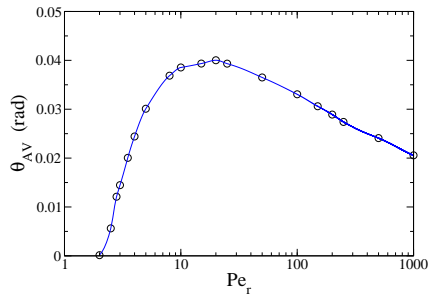
5.4.2   The flow aligned state

Figure 5.14: *The shear-dependent average angle* θ_{AV} *between the arrested director and the flow direction in the flow-aligned system, as a function of* Pe_r.

In the right panel of Fig. 5.13, we have plotted the order parameter P_2 and the components of the director, corresponding to the arrested state of Fig. 5.11(c), as a function of strain. The fluctuations of $\hat{n}_z$ with extremely small amplitude around zero indicate an in-plane motion. The small but nonzero value of $\hat{n}_y = \sin\theta$ allows us to calculate θ_{AV} from $\langle\hat{n}_y\rangle = \sin\theta_{AV}$, which is about 0.04 rad (2.5 degrees) in this case. In Fig. 5.14, we plot θ_{AV} as a function of Pe_r with aspect ratio and volume fraction given by $L/D = 25$ and $L\varphi/D = 3.5$, respectively. The average angle θ_{AV} increases with increasing shear rate until it reaches a maximum value where $\theta_{AV} \approx 0.04$ rad. After that a flow-induced decay of θ_{AV} toward zero is observed, which is attributed to an increase of the orientational order with shear rate. The existence of a maximum angle was found previously by Mori *et al.* [106] when simulating ellipsoids with $L/D = 3$ in shear flow. Before them, Marrucci and Maffettone [97] had analyzed theoretically the nonlinear behavior of nematic rods in shear flow by solving the Doi-Hess equation in two dimensions, and had found a maximum for θ_{AV} as well.

The maximum of θ_{AV} as a function of the aspect ratio of the rods is shown in Fig. 5.15 for various volume fractions. We find that, on the one hand, the larger the shape anisotropy is, the
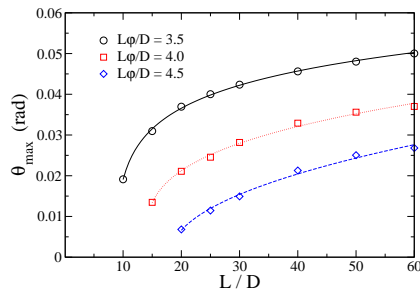
Figure 5.15: *The maximum averaged flow-aligned angle θ_{max} as a function of L/D, for three scaled volume fractions.*

larger is the maximum angle θ_{max}, while on the other hand, θ_{max} decreases with increasing scaled volume fraction.

5.5 Influence of the initial director

Theoretical analysis on the basis of the Doi-Hess equation has revealed that the stationary orbit into which a nematic system finally settles also depends on the initial conditions. We therefore investigate this dependence by simulating rods of aspect ratio equal to 20 at volume fractions given by $L\varphi/D = 3.5$ for various initial configurations and at various shear rates.

Fig. 5.16 applies to a shear rate of $228\ s^{-1}$, *i.e.*, the rotational Peclet number equals 0.5. In Fig. 5.16(a), the rods were initially perfectly aligned along the flow direction $\hat{\mathbf{e}}_x$, in Fig. 5.16(b) along the gradient direction $\hat{\mathbf{e}}_y$, while in Fig. 5.16(c) they were initially placed at random orientations in the box, *i.e.*, the box starts from the (unstable) isotropic state. In all three cases, the director ends up kayaking. In cases (a) and (b), it takes a while before the director develops an out-of-plane component and changes its motion from tumbling to kayaking. In case (c), the order parameter quickly rises to its equilibrium value and the director starts kayaking straight away without first performing some in-plane tumblings. The latter behavior is easily understood by noting that the director has an out-of-plane component from the very beginning. Fig. 5.16(d) shows what happens when the rods start off being perfectly aligned along the vorticity direction, $\hat{\mathbf{e}}_z$. During the whole run, P_2 remains close
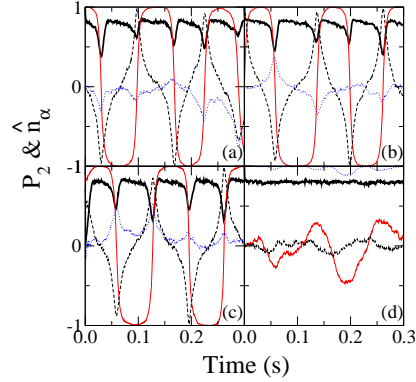
Figure 5.16: *The scalar order parameter P_2 (thick solid line) as well as the three components $\hat{n}_x$ (solid), $\hat{n}_y$ (dashed) and $\hat{n}_z$ (dotted) of the director as functions of time. Nematic simulation boxes initially aligned along the flow (a) and gradient (b) direction, as well as an initially isotropic (c) box, quickly evolve a kayaking motion. The nematic box aligned along the vorticity direction (d), however, shows a log-rolling motion. In all plots, $L/D = 20$, $L\varphi/D = 3.5$ and $\dot{\gamma} = 228\ s^{-1}$.*

to one, while $\hat{n}_z$ also hardly deviates from unity, meaning that the rods remain close to the vorticity axis. The component along the gradient direction only differs slightly from zero, indicating that the motion occurs more or less in the velocity-vorticity plane. In this plane the director is seen to oscillate, or wag, about the vorticity axis. This type of motion is called log-rolling.

So, when the rods were initially aligned along the gradient direction, the final motion was kayaking, while in case they started off from the vorticity direction, the final motion was log-rolling. It is constructive to see what happens to the final state when we gradually change the direction along which the rods start from the gradient direction to the vorticity direction. Thus, we ran several simulations with the rods initially all aligned along $\hat{\mathbf{n}}(0) = \cos(\alpha)\hat{\mathbf{e}}_y + \sin(\alpha)\hat{\mathbf{e}}_z$ with α ranging from 0 to 90 degrees in steps of 10 degrees. We found that for $\alpha \leq 30^o$, the system ended up kayaking, while for $\alpha \geq 40^o$, the end state was of the log-rolling type. Similar results were found by Andrews *et al.* [5] on the basis of a continuum equation similar to Eq. (5.2) in this Chapter. Obviously, it is too costly to perform similar
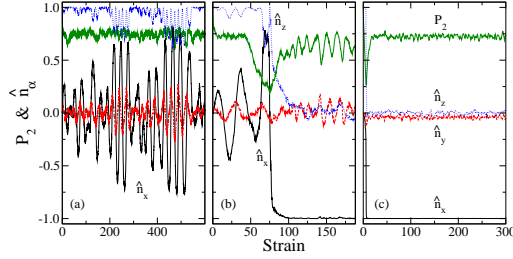
calculations with the methods in present work.

Figure 5.17: *At a low shear rate of* 250 s^{-1}*, a system initially aligned along the vorticity direction shows a log-rolling motion (a), which is stable against occasional fluctuations. At an intermediate shear rate of* 375 s^{-1}*, the system performs a log-rolling motion at the beginning, which gives way to a wagging (b) motion, while the same system immediately progresses to a flow-aligning (c) state at the high shear rate of* 2500 s^{-1}*.* $L/D = 25$ *and* $L\varphi/D = 3.5$*.*

Finally, we study rods which are initially aligned along the vorticity direction, at various shear rates. In Fig. 5.17, we present the scalar order parameter P_2 and the components of the director as a function of strain. At a moderate shear rate of 250 s^{-1}, the director exhibits a log-rolling type of motion. At a much higher shear rate of 2500 s^{-1}, $\hat{\mathbf{n}}$ exhibits a flow-aligning motion. At an intermediate shear rate of 375 s^{-1}, in panel (b) an initially log-rolling system finally makes a transition to the wagging state. At a shear rate of 250 s^{-1} the same system remains in the log-rolling state, while at a shear rate of 500 s^{-1}, it immediately transforms into the wagging state. We conclude from this that the transition takes place at $\dot{\gamma}_{\mathrm{lrw}} \approx 375$ s^{-1}, which is slightly larger than $\dot{\gamma}_{\mathrm{kw}}$ found in the previous section for the system. Note that the run time in Fig. 5.17(a) is much longer than in Fig. 5.16. As a result, Fig. 5.17(a) reveals that the log-rolling motion once in a while becomes severely perturbed, but that the shear forces and torques are not strong enough to overcome the elastic forces and to rotate the whole system to the flow direction. At high shear rates this finally happens. Again, we leave a more thorough analysis for future research.

5.6 Conclusion

A newly developed event-driven Brownian dynamics algorithm has enabled us, for the first time, to simulate the fascinating collective dynamics of dense solutions of highly elongated rigid particles in shear flow. The aspect ratio L/D of the rods was varied from 10 to 60, where the latter value and the diameter D were chosen to facilitate a numerical comparison with recent experimental studies on solutions of *fd* viruses. At scaled volume fractions $L\varphi/D$ of 3.5 to 4.5, the systems are in a stable nematic phase, with an orientation characterized by the director. In shear flow the director is observed to trace out a number of distinct paths, depending on the values of the aforementioned properties and on the initial state of the box. We find good agreement with numerical solutions of the Doi-Hess equation and with experiments on the *fd* virus.

The main conclusions of this Chapter are:

1. At low shear rates, a system with a director initially parallel to the shear plane shows a transient in-plane tumbling motion of the director, which evolves into an out-of-plane kayaking motion over the course of several tumbling periods. This accords with Faraoni's findings that the tumbling motion is unstable in the Doi-Hess theory.

2. For boxes with an initial director outside the shear plane we find that the paths of the directors converge to either a kayaking or a log-rolling motion. Extended simulations in the latter state show that it is a long-lived state at low shear rates, which implies that the transition barrier separating the two orbits must be fairly high.

3. The tumbling period of the kayaking motion is found to scale proportional with the scaled volume fraction and inversely proportional with the shear rate, but is independent of the aspect ratio of the rod: $T = 4.2 \frac{L}{D}\varphi\dot{\gamma}^{-1}$. For the longest rods, $L/D = 60$, we obtain kayaking periods that compare well with experimental values on the *fd* virus. Theoretical predictions by Larson and others relating the tumbling period to the order parameters P_2 and P_4 are corroborated.

4. At higher shear rates both the out-of-plane kayaking and the log-rolling motions give way to an in-plane wagging motion. The critical rate of this transition depends strongly on $L\varphi/D$ and to a weaker extent on L/D. For the longest rods, we again find a favor-

able comparison with the experimental value. The wagging periods closely follow the expression for the kayaking period.

5. With increasing shear rate, the amplitude of the wagging motion steadily decreases till a flow aligned state is reached. The angle between the director of this arrested state and the flow direction, in turn, initially rises with increasing shear rate but returns to zero at the highest shear rates.

In *Chapter* 6 we will report on the rheological properties [131] of these systems.

Shear viscosities and normal stress differences of rigid liquid-crystalline polymers

6

Shear viscosities as well as first and second normal stress differences of solutions of rigid spherocylindrical colloids are investigated by Brownian dynamics simulations for shape anisotropies L/D in a range from 25 to 60 and scaled volume fractions $L\varphi/D$ from 0.5 to 4.5. A shear thinning behavior is observed in all cases. In the isotropic phase, the calculated viscosities at low volume fractions are in agreement with predictions by Dhont and Briels, while over a larger range they are described by the Hess equation. The self rotational diffusion coefficients obtained from the flow curves agree very well with those calculated by traditional methods. In the nematic phase, the inflexion point of the flow curve is associated with the critical shear rate at which the orientational director changes its motion from kayaking to wagging. The first normal stress difference N_1 in the nematic solution is positive at low and high shear rates, but negative at moderate rates, which is rather distinct from the monotone behavior shown by isotropic solutions. The simulated second normal stress difference N_2 is found much smaller in amplitude than N_1 but always opposite in sign. Our findings qualitatively confirm existing theoretical predictions and experimental measurements. A newly developed event-driven Brownian dynamics algorithm, in which the excluded volume interactions between particles are incorporated as collisions instead of repulsive potentials, has made these simulations feasible. *

6.1 Introduction

Suspensions of nematic rod-like colloids or liquid-crystalline polymers (LCPs) in shear flow exhibit unusual rheological behaviors, such as pronounced oscillations of the stress against time or a negative first normal stress difference at intermediate shear rates. Because of this complex dynamics, as compared to conventional polymer liquids, concentrated lyotropic LCPs aroused much scientific interests both in theoretical predictions [2, 20, 21, 23, 24, 25, 33, 36, 41, 42, 59, 62, 69, 80, 81, 82, 83, 84, 96, 97, 98, 99] and in experimental observations [7, 8, 14, 17, 53, 67, 68, 73, 74, 91, 93, 103, 105, 145]. Hess [59] and Doi [33] suggested a molecular theory of rod-like LCPs in shear flow. The Doi-Hess theory has been solved numerically, by restricting it to two dimensions [97] or by expanding the orientational distribution function in spherical harmonics [80, 84]. It was found that the director, *i.e.*, the average direction of the rods, exhibits tumbling, kayaking, wagging, flow-aligning or log-rolling types of motion, depending on the applied shear rates. The theoretical investigations revealed that all peculiar behaviors mentioned above are to be attributed to the periodic oscillation of the director.

Besides theoretical and experimental investigations, computer simulation becomes an increasingly valuable supplement in the quest to understand complex LCPs. Unfortunately, the previous computational studies on the rheology of rigid rods only focused on isotropic solutions [142, 143] or rods with small aspect ratios [106]. In order to study suspensions of rigid long and thin rods in shear flow, we [129, 130, 132] recently developed an event-driven Brownian dynamics simulation algorithm in which excluded volume interactions between rods are taken into account but hydrodynamic interactions are considered unimportant and negligible. This algorithm has its inherent novelty in preventing the overlaps between interacting rods by carefully controlling the collisions in stead of by applying a repulsive potential. By this algorithm, the collective periodic orientational motions of the directors of nematic solutions of rigid rods with large shape anisotropy are clearly described for the first time [129, 130]. As a supplement of the previous work, we continue our investigations with the rheological properties, *i.e.*, viscosities and normal stress differences, of rigid Brownian rods in shear flow.

This Chapter is organized as follows: In section 6.2 we briefly discuss the microscopic theory for the viscoelastic behavior of suspensions of rigid rods with excluded volume interactions. In sections 6.3.1 and 6.3.2 we investigate the shear rate dependence of the viscosities

of rod-like colloids in isotropic and nematic phases, respectively, while the calculated first and second normal stress differences are presented in section 6.3.3. Finally, we summarize our conclusions in section 6.4. The algorithm of the event-driven Brownian dynamics simulation is omitted in the present Chapter, since it has already been discussed in *Chapters* 3, 4 and 5.

6.2 Theory

In this section we briefly comment on the expression that we have used to calculate stresses from our simulation data. In order to motivate our choice, we start with the one-particle Smoluchowski equation [24]

$$\frac{\partial}{\partial t}P(\hat{\mathbf{u}},t) = D_r\hat{\mathscr{R}} \cdot \left\{\hat{\mathscr{R}}P(\hat{\mathbf{u}},t) - \beta P(\hat{\mathbf{u}},t)\bar{\mathbf{T}}(\hat{\mathbf{u}},t)\right\} - \hat{\mathscr{R}} \cdot P(\hat{\mathbf{u}},t)\hat{\mathbf{u}} \times (\mathbf{\Gamma} \cdot \hat{\mathbf{u}}) \,, \qquad (6.1)$$

describing the time evolution of the one-particle orientational probability distribution $P(\hat{\mathbf{u}},t)$ of a collection of rods at time t with unit vectors $\hat{\mathbf{u}}$ along their long axes. The rotational operator $\hat{\mathscr{R}}$ is defined as $\hat{\mathscr{R}} \equiv \hat{\mathbf{u}} \times \frac{\partial}{\partial\hat{\mathbf{u}}}$, and plays a role very similar to that of the gradient operator ∇_r in the description of translational diffusion. D_r is the rotational diffusion coefficient of a single rod

$$D_r = \frac{3k_BT\ln(L/D)}{\pi\eta_sL^3} \,, \qquad (6.2)$$

with η_s the viscosity of the solvent. β is $1/k_BT$ with k_B being Boltzmann's constant and T the temperature. $\mathbf{\Gamma}$ is the velocity gradient tensor, related to the flow velocity $\mathbf{V}$ at position $\mathbf{r}$ by $\mathbf{V} = \mathbf{\Gamma} \cdot \mathbf{r}$; in this work $\mathbf{\Gamma} = \dot{\gamma}\hat{\mathbf{e}}_x\hat{\mathbf{e}}_y$ with $\dot{\gamma}$ the shear rate and $\hat{\mathbf{e}}_\alpha$ a unit vector in the α-direction. The average torque acting on the central rod $\bar{\mathbf{T}}(\hat{\mathbf{u}},t)$ in Eq. (6.1) is expressed as

$$\bar{\mathbf{T}}(\hat{\mathbf{u}},t) = -\bar{\rho}\int d\mathbf{r}' \oint d\hat{\mathbf{u}}' \, P(\hat{\mathbf{u}}',t)g(\mathbf{r} - \mathbf{r}',\hat{\mathbf{u}},\hat{\mathbf{u}}',t)\hat{\mathscr{R}}V(\mathbf{r} - \mathbf{r}',\hat{\mathbf{u}},\hat{\mathbf{u}}') \,, \qquad (6.3)$$

where $\bar{\rho}$ is the number density of rods and $V(\mathbf{r} - \mathbf{r}',\hat{\mathbf{u}},\hat{\mathbf{u}}')$ is the pair-interaction potential for two rods with orientations $\hat{\mathbf{u}}$ and $\hat{\mathbf{u}}'$ and center-center separation $\mathbf{r} - \mathbf{r}'$; similarly, $g(\mathbf{r} - \mathbf{r}',\hat{\mathbf{u}},\hat{\mathbf{u}}',t)$ is the pair correlation function for the two rods mentioned above at time t. The main approximation made in deriving Eq. (6.1) was to neglect hydrodynamic interactions between the rods. For analytical purposes, we now neglect the time dependence of the pair

correlation function and approximate it by its equilibrium value for very long rods

$$g(\mathbf{r} - \mathbf{r}', \hat{\mathbf{u}}, \hat{\mathbf{u}}', t) = \exp\left\{-\beta V(\mathbf{r} - \mathbf{r}', \hat{\mathbf{u}}, \hat{\mathbf{u}}')\right\} . \tag{6.4}$$

Making one more approximation when expanding $\left|\hat{\mathbf{u}} \times \hat{\mathbf{u}}'\right|$ up to second order in orthogonal polyadic products of $\hat{\mathbf{u}}$'s [132], we may calculate the equation of motion of the order tensor $\mathbf{S} = \langle \hat{\mathbf{u}}\hat{\mathbf{u}} \rangle$, with the brackets denoting an ensemble average, obtaining [24]

$$\frac{d}{dt}\mathbf{S} = -6\mathrm{D}_r\left\{\mathbf{S} - \frac{1}{3}\hat{\mathbf{I}} + \frac{5}{4}\frac{L}{D}\varphi(\mathbf{S}^{(4)} : \mathbf{S} - \mathbf{S}\cdot\mathbf{S})\right\} + \dot{\gamma}\left\{\hat{\mathbf{\Gamma}}\cdot\mathbf{S} + \mathbf{S}\cdot\hat{\mathbf{\Gamma}}^T - 2\mathbf{S}^{(4)} : \hat{\mathbf{E}}\right\} , \tag{6.5}$$

where $\hat{\mathbf{I}}$ is the unit tensor, $\hat{\mathbf{\Gamma}} = \mathbf{\Gamma}/\dot{\gamma}$ and $\hat{\mathbf{E}} = \frac{1}{2}[\hat{\mathbf{\Gamma}} + \hat{\mathbf{\Gamma}}^T]$, with the superscript 'T' denoting a transposition. The volume fraction is defined as $\varphi = \frac{1}{4}\bar{\rho}\pi D^2 L$. $\mathbf{S}^{(4)}$ is a fourth order tensor defined by $\mathbf{S}^{(4)} = \langle \hat{\mathbf{u}}\hat{\mathbf{u}}\hat{\mathbf{u}}\hat{\mathbf{u}} \rangle$. In a previous paper [133], we have argued that most probably the last two approximations mentioned above are the most severe in determining the quality of Eq. (6.5). It is important to notice that they are only used in calculating the term proportional to $L\varphi/D$. The extra factor of $5/4$ in this term as compared to the corresponding term in Ref. 24 has been explained in our previous paper [132].

The expression needed to calculate the deviatoric part $\mathbf{\Sigma}$ of the stress tensor has been derived by Dhont and Briels [24, 25] and reads

$$\mathbf{\Sigma} = 2\eta_s\dot{\gamma}\hat{\mathbf{E}} + 3\bar{\rho}k_B T\left\{\mathbf{S} - \frac{1}{3}\hat{\mathbf{I}} + \frac{5}{4}\frac{L}{D}\varphi(\mathbf{S}^{(4)} : \mathbf{S} - \mathbf{S}\cdot\mathbf{S}) + \frac{1}{6}\frac{\dot{\gamma}}{\mathrm{D}_r}\left(\mathbf{S}^{(4)} : \hat{\mathbf{E}} - \frac{1}{3}\hat{\mathbf{I}}\mathbf{S} : \hat{\mathbf{E}}\right)\right\} . \tag{6.6}$$

Also here the somewhat uncontrolled approximations concerning the pair correlation function are only used in a term proportional to $L\varphi/D$, which carries a factor of $5/4$ for the same reason as the term proportional to $L\varphi/D$ in Eq. (6.5). Fortunately, apart from a constant factor, both terms proportional to $L\varphi/D$ are equal in Eqs. (6.5) and (6.6), and so we may eliminate the one in Eq. (6.6), obtaining [24]

$$\mathbf{\Sigma} = 2\eta_s\dot{\gamma}\hat{\mathbf{E}} + \frac{2(L/D)^2}{3\ln(L/D)}\varphi\eta_s\dot{\gamma}\left\{\hat{\mathbf{\Gamma}}\cdot\mathbf{S} + \mathbf{S}\cdot\hat{\mathbf{\Gamma}}^T - \mathbf{S}^{(4)} : \hat{\mathbf{E}} - \frac{1}{3}\hat{\mathbf{I}}\mathbf{S} : \hat{\mathbf{E}} - \frac{1}{\dot{\gamma}}\frac{d\mathbf{S}}{dt}\right\} . \tag{6.7}$$

This expression for $\mathbf{\Sigma}$ may be considered to be largely independent of any approximations concerning the pair correlation function. Obviously, it still suffers from the neglect of hydrodynamic interactions, which under some circumstances may be important. The term proportional to $d\mathbf{S}/dt$ in Eq. (6.7) will be ignored for the following reasons. In the isotropic state,

i.e., at low volume fractions, the order tensor is constant and consequently $d\mathbf{S}/dt$ has no contribution at all. In the nematic state at low shear rates, the order tensor varies periodically in time with constant period, meaning that $d\mathbf{S}/dt$ is non-zero. In the present work, however, we will calculate viscosities and normal stress differences averaged over integer numbers of oscillation periods, rendering zero the contributions of $d\mathbf{S}/dt$ to the final results. In the nematic state at very high shear rates, the order tensor becomes constant and $d\mathbf{S}/dt = 0$ again.

In our simulations, we impose a simple shear flow in the *x*-direction with gradient in the *y*-direction. The relative viscosity η^* averaged over time reads

$$\eta^* = \frac{\bar{\Sigma}_{xy}}{\dot{\gamma}\eta_s} = 1 + \frac{2(L/D)^2}{3\ln(L/D)}\varphi\left(\hat{\mathbf{\Gamma}}\cdot\mathbf{S} + \mathbf{S}\cdot\hat{\mathbf{\Gamma}}^T - \mathbf{S}^{(4)}:\hat{\mathbf{E}} - \frac{1}{3}\hat{\mathbf{I}}\mathbf{S}:\hat{\mathbf{E}}\right), \qquad (6.8)$$

while first and second normal stress differences are calculated from their definitions:

$$N_1 \quad \equiv \quad \bar{\Sigma}_{xx} - \bar{\Sigma}_{yy}, \qquad\qquad\qquad (6.9)$$

$$N_2 \quad \equiv \quad \bar{\Sigma}_{yy} - \bar{\Sigma}_{zz}. \qquad\qquad\qquad (6.10)$$

The bars in $\bar{\Sigma}_{xy}$ denote a time averaging.

6.3 Results and discussions

In this section, we describe our simulation results of stresses in solutions of rod-like colloids. First, we address shear viscosities of isotropic systems as a function of shear rate. Next, we discuss similar results for nematic phases and finally, we study first and second normal stress differences in both isotropic and nematic phases in shear flow.

The simulated rigid rods are based on experimental data of the *fd* viruses [30, 88]. These rod-like biopolymers, because of their monodispersity and well-characterized interparticle interactions, are considered to be among the best representatives of rigid rods for experimental purposes. For a recent review article, we refer the reader to Dogic and Fraden [31]. Our simulation boxes were cubic and periodic boundary conditions were employed in both the velocity and vorticity direction, while the Lees-Edwards boundary conditions were used in the gradient direction [1]. Box volumes were chosen according to $V = c\frac{\pi}{4}\left(\frac{L}{D}\right)^{-1}L^3$ with $c = 500$ for $L/D \leq 40$, $c = 750$ for $L/D = 50$ and $c = 1000$ for $L/D = 60$. By doing so, the edges of the boxes were always $2.5 \sim 3$ times as large as the rod lengths. The number of rods

N was obtained from $N = cL\varphi/D$ and ranged from 250 to 4500. The diameter was chosen to be 14.8 nm. Water was used as solvent, with viscosity $\eta_s = 10^{-3}$ Pa s. The temperature was 300 K in all cases. The event-driven algorithm described previously [132] was used with a timestep δt of 0.5 μs, which is at least one order of magnitude larger than that used in simulations [133] using semi-hard interactions between rods.
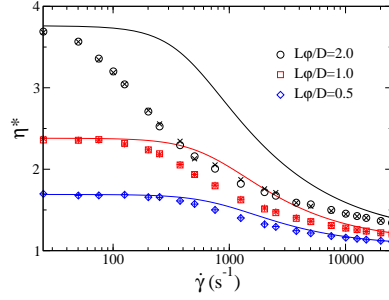
6.3.1 Shear thinning of isotropic systems

Figure 6.1: *The relative viscosities of isotropic suspensions of rigid rods with aspect ratio L/D = 25 for three scaled volume fractions. Circles, squares and diamonds represent the results for Lφ/D = 2.0, 1.0 and 0.5, respectively, while crosses, stars and pluses represent the corresponding η* obtained by using the closure Equation (6.11) on the basis of order tensors S from the simulations. Curves represent theoretical results predicted by Dhont and Briels [24].*

In Fig. 6.1 we have plotted the relative viscosities η^* as a function of shear rate for three isotropic systems consisting of rods with aspect ratio equal to 25. A clear shear thinning is observed in all cases. For comparison we have included the results obtained by calculating $\mathbf{S}^{(4)} : \hat{\mathbf{E}}$ in Eq. (6.7) using the closure relation

$$\mathbf{S}^{(4)} : \hat{\mathbf{E}} \approx \frac{1}{5} \left\{ \mathbf{S} \cdot \hat{\mathbf{E}} + \hat{\mathbf{E}} \cdot \mathbf{S} - \mathbf{S} \cdot \mathbf{S} \cdot \hat{\mathbf{E}} - \hat{\mathbf{E}} \cdot \mathbf{S} \cdot \mathbf{S} + 2\mathbf{S} \cdot \hat{\mathbf{E}} \cdot \mathbf{S} + 3\mathbf{S}\mathbf{S} : \hat{\mathbf{E}} \right\} , \qquad (6.11)$$

on the basis of the simulated orientational order tensor $\mathbf{S}$. The viscosities calculated by using the closure Eq. (6.11) are seen to be within $\approx 3\%$ of the exact values in the case of isotropic suspensions. Apparently, the above closure is very accurate, in agreement with our previous

findings [133]. Also shown in Fig. 6.1 are viscosities calculated by means of a theory by Dhont and Briels [24], using the approximate pair correlation function of Eq. (6.4). In the case of $L\varphi/D = 0.5$ the agreement is limited to the lowest shear rates and the neglect of dynamic correlations is apparently unimportant. This holds true to a lesser extent when $L\varphi/D = 1$. For $L\varphi/D = 2$ the agreement is very bad, which was to be expected since this volume fraction is rather close to the isotropic-nematic phase transition where a good description of pair correlations becomes increasingly important.
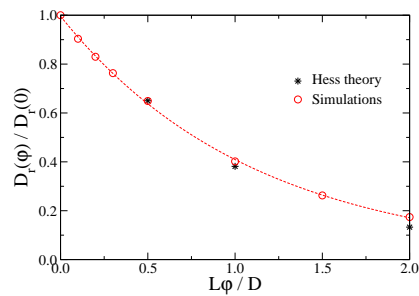

Figure 6.2: *The self rotational diffusion coefficients of rods with $L/D = 25$ in isotropic suspensions, as a function of the scaled volume fraction. Circles denote the traditional measurements by using the Debye expression, Eq. (6.13), while stars are calculated from the viscosity by the Hess theory, Eq. (6.12).*

Some twenty years ago, Hess has suggested that these viscosities may be described by [60, 61, 134]

$$\eta^* = \eta_\infty^* + \frac{\eta_0^* - \eta_\infty^*}{1 + (\dot{\gamma}\tau_r)^2} \, , \tag{6.12}$$

where η_0^* and η_∞^* are the values at zero shear rate and very large shear rates, respectively. τ_r is a characteristic time given by $\tau_r = 1/6D_r(\varphi)$. This latter expression has been tested experimentally by Graf *et al.* [53] on isotropic systems of *fd* viruses. By fitting their measured viscosities with the Hess equation, they found $D_r(\varphi)$ in good agreement with self rotational diffusion coefficients obtained from electric or magnetic birefringence experiments [75, 94, 110]. We have made similar fits and present the $D_r(\varphi)$ obtained this way in Fig. 6.2, together

97

with those obtained by calculating $D_r(\varphi)$ using

$$\langle \hat{\mathbf{u}}(t) \cdot \hat{\mathbf{u}}(0) \rangle = \exp\{-2D_r(\varphi)t\} \ . \tag{6.13}$$

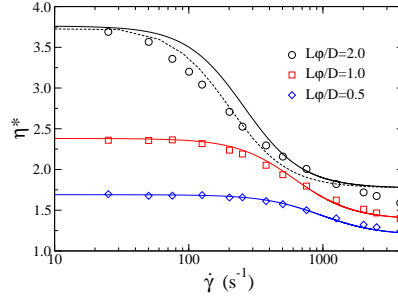It is seen that both methods yield results in very good agreement with each other.

Figure 6.3: *The relative viscosities of isotropic suspensions of rigid rods with $L/D = 25$ as a function of shear rate. Drawn lines show the results of Eq. (6.14) with $D_r(\varphi)$ calculated from the Debye expression, Eq. (6.13), while the dashed curve is a three parameter fit with the Hess theory, Eq. (6.12).*

In their review paper [24], Dhont and Briels apply a perturbation theory to calculate viscosities of isotropic suspensions at low shear rates and low volume fractions. By expanding the Hess equation to the same order and comparing both expressions, η_0^* and η_∞^* may be calculated. Using the results in the Hess equation, we obtain

$$\eta^* = (1 + \alpha \frac{L}{D}\varphi) - \frac{18}{25}\frac{1}{1 + \left(\frac{6D_r(\varphi)}{\dot{\gamma}}\right)^2}\alpha\frac{L}{D}\varphi \ , \tag{6.14}$$

where the coefficient α is given by

$$\alpha = \frac{8}{45}\frac{L/D}{\ln(L/D)} \ . \tag{6.15}$$

In Fig. 6.3 we compare viscosities obtained with this equation with those calculated from our simulation results. It is seen that for the lowest two volume fractions, the results agree remarkably well. For $L\varphi/D = 2.0$ the agreement is less perfect, and in this case a fit with the Hess equation using η_0^*, η_∞^* and τ_r as adjustable parameters performed slightly better, as indicated by the dashed line.
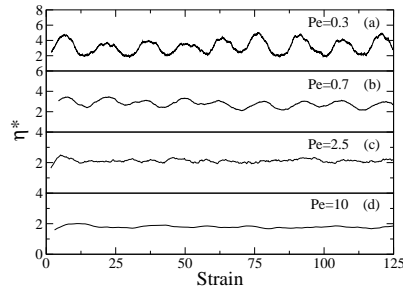
6.3.2 Shear thinning of nematic systems

Figure 6.4: *The relative viscosities η^*, calculated by Equation (6.7) including the $d\mathbf{S}/dt$ term, as a function of strain. In panel (a)-(d), four different shear rates are employed with the corresponding rotational Peclet numbers $\mathrm{Pe}_r = 0.3$, 0.7, 2.5 and 10.0, respectively. A running average of $d\mathbf{S}/dt$ is used for each panel to reduce the noise produced by the numerical differentiation of $\mathbf{S}$.*

In this section we describe our results of calculating shear viscosities of nematic systems. First, in Fig. 6.4 we plot the relative viscosity as a function of strain for a nematic system of rods with aspect ratio equal to 25 and scaled volume fraction $L\varphi/D = 3.5$ for four different Peclet numbers. The viscosities $\eta^*(t) = \Sigma_{xy}(t)/\dot{\gamma}\eta_s$ in this plot are not time averaged and are calculated using Eq. (6.7), including the term proportional to $d\mathbf{S}/dt$. Similar calculations, neglecting the term proportional to $d\mathbf{S}/dt$, reveal that this term smooths the results a bit, but has no influence on the time averaged results that we are interested in. In panels (a) and (b), the viscosity is clearly seen to periodically vary in time. In a previous paper [130] we found that at the corresponding shear rates, the director of the system being studied here performs kayaking motions. Comparing viscosities and director motions, we find, to no surprise, that the peaks in the viscosities in panels (a) and (b) occur at strains where the directors flip from one flow aligned orientation to the other. Panel (c) corresponds to a shear rate just above the kayaking to wagging transition. Hence the director is mainly situated in the shear plane, "wagging" about the velocity direction. The viscosity displays some small oscillations, which are rather insignificant compared to the absolute value. At very high shear rates, in panel (d), the director is arrested in the shear plane making a small angle with the flow direction. The
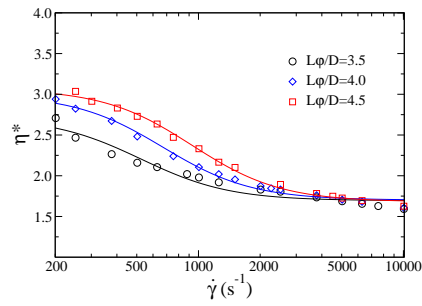
Figure 6.5: *The relative viscosities of nematic suspensions of rigid rods with aspect ratio L/D = 25 at three scaled volume fractions of 3.5, 4.0 and 4.5, respectively.*

corresponding viscosity is virtually constant.

In Fig. 6.5 we display time averaged viscosities as a function of shear rate, again for rods with aspect ratio $L/D = 25$, for three different volume fractions. The drawn lines will be discussed later, and should be considered as guides to the eye for the time being. As in the case of isotropic systems, a clear shear thinning is observed for all three volume fractions. In Fig. 6.6 shear viscosities are shown to be linear in $L\varphi/D$ over a large range of shear rates.
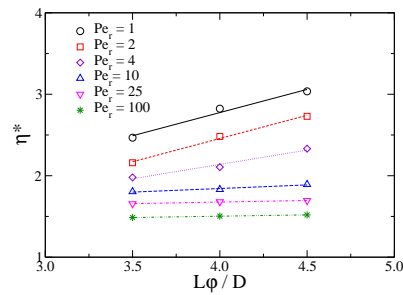

Figure 6.6: *The relative viscosities of nematic solutions of rods with L/D = 25 as a function of the scaled volume fraction, for various shear rates ranging from* $Pe_r = 1$ *to* 100.

Next, in Fig. 6.7 we investigate the dependence of η^* on the aspect ratio L/D; the scaled volume fraction in all cases is given by $L\varphi/D = 4.5$. Two things may be noticed. First, the zero shear rate value of the viscosity increases substantially with increasing values of
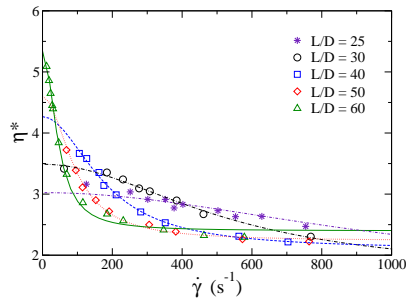
Figure 6.7: *The relative viscosities of nematic systems as a function of shear rate. Solutions of rigid rods with L/D from 25 to 60 are investigated. The simulation results are fitted using the Hess formula [61] given in Eq. (6.12).*

L/D. Second, the inflexion point of the shear thinning curve moves to lower shear rates with increasing aspect ratios.
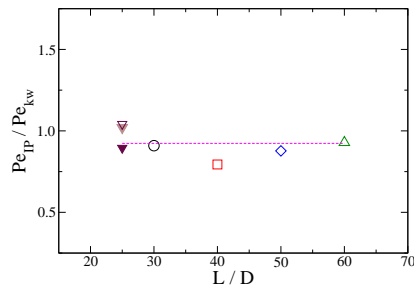

Figure 6.8: *The ratio Pe_{kw}/Pe_{IP} as a function of aspect ratio. Pe_{kw} denotes the critical Peclet number at which the kayaking to wagging transition occurs, as obtained from inspection of the periodic orientational motions exhibited by the director. Pe_{IP} stands for the Peclet number calculated from the inflexion point of the viscosity by using the Hess theory, see Eq. (6.12). Open symbols represent systems with a scaled volume fraction of 4.5, while the grey and solid triangles denote $L\varphi/D = 4.0$ and 3.5, respectively.*

It is intuitively clear that the shear rate $\dot{\gamma}_{IP}$ at the inflexion point of the viscosity curve reveals some dominant characteristic time in the system. It seems therefore to be appropriate

to fit the shear thinning curves for nematic systems with the Hess equation, just as we did with the corresponding curves for isotropic systems. The drawn lines in Figs. 6.5 and 6.7 were obtained in this way. Estimates of $\dot{\gamma}_{IP}$ are then calculated according to

$$\dot{\gamma}_{IP} = (\sqrt{3}\tau_r)^{-1} . \tag{6.16}$$

It is instructive to compare these values with the shear rates $\dot{\gamma}_{kw}$ at the kayaking to wagging transitions in the corresponding systems. Therefore, in Fig. 6.8 we plot $\dot{\gamma}_{IP}/\dot{\gamma}_{kw}$ as a function of L/D for all systems studied in Figs. 6.5 and 6.7. It is seen that for all aspect ratios $\dot{\gamma}_{IP}$ is almost equal to $\dot{\gamma}_{kw}$. The origin of shear thinning in nematic systems may therefore safely be attributed to the kayaking to wagging transition of the director.
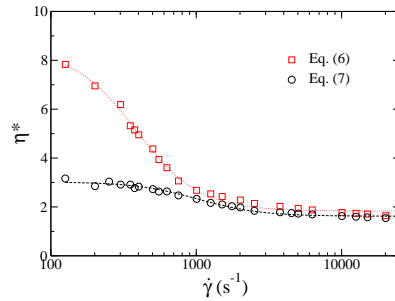

Figure 6.9: *A comparison of the relative viscosities calculated by Eq. (6.6) (shown as squares) and (6.7) (circles) in nematic solutions of rods with $L/D = 25$ and $L\varphi/D = 4.5$ at various share rates. The dotted and dashed lines are fits by the Hess theory, Eq. (6.12).*

Before finishing this subsection, let us make one more remark. In Fig. 6.9 we have plotted flow curves, *i.e.*, viscosities as a function of shear rate, for systems with $L/D = 25$ and $L\varphi/D = 4.5$, once calculated using Eq. (6.6) and once using Eq. (6.7). There is a clear difference between the two curves, with Eq. (6.6) producing the larger viscosities. On fitting the new curve with the Hess equation, we found that its inflexion point occurs at a shear rate $\dot{\gamma}_{IP}$ which is a factor of 2.5 smaller than $\dot{\gamma}_{kw}$. This discrepancy may be considered a, be it weak, argument in favor of Eq. (6.7).

6.3.3 Normal stress difference

Measurements [73, 74] of normal stress differences of nematic liquid crystalline polymers show remarkable differences compared with those exhibited by isotropic suspensions. For a concentrated yet isotropic solution, the first normal stress difference N_1 is always positive and increases monotonically with shear rate, while the second normal stress difference N_2 is negative and decreases with shear rate. In nematic solutions, on the other hand, highly nonlinear rheological behaviors are observed: both the first and the second normal stress differences change signs several times with increasing shear rate.
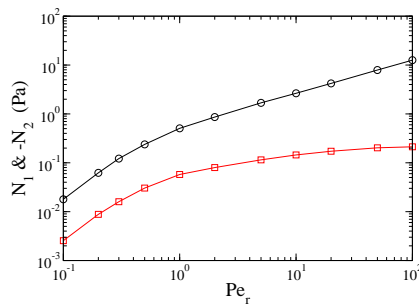

Figure 6.10: *First (shown as circles) and second (squares; note the reversal of sign) normal stress differences of isotropic solutions of rigid rods with $L/D = 25$ as a function of rotational Peclet number. The scaled volume fraction $L\varphi/D$ is chosen equal to* 2.0.

In Fig. 6.10, we plot N_1 and $-N_2$ as a function of the rotational Peclet number in log-log scale. The scaled volume fraction $L\varphi/D$ is chosen equal to 2.0, ensuring an isotropic system [132]. The monotonic increase in magnitude of both N_1 and N_2 agrees qualitatively with experimental results on rod-like PBLG (poly(γ-benzyl L-glutama)) in the isotropic phase by Magda *et al.* [93] It is well known that the probability distribution function of the end-to-end vector of polymers, whether flexible or rigid, in isotropic phases are distorted from spherical to ellipsoidal distributions when such systems are subjected to shear flow. The resulting elastic forces must be balanced by shear forces, making Σ_{xx} invariably positive and Σ_{yy} negative [97]. Since the flow hardly influences the distribution in the vorticity direction, Σ_{zz} remains very small and the normal stress differences have the signs found in our simulation.

The absolute values of N_1 and N_2 of nematic suspensions are plotted as a function of Peclet number in Fig. 6.11(a) and (b), respectively. The aspect ratio L/D is chosen equal to 25 again, while the scaled volume fraction $L\varphi/D = 3.5$, ensuring the nematic state of the systems. Compared with the behaviors shown by the isotropic suspensions, distinctive phenomena are observed in nematic phases: both normal stress differences are not monotonic any more, but change sign with shear rate. The first normal stress difference N_1 is found positive at low and high shear rates, but negative at intermediate shear rates. The second normal stress difference N_2 is much smaller in magnitude than N_1 and always opposite in sign. This feature of N_2 is in accordance with that shown by isotropic solutions.
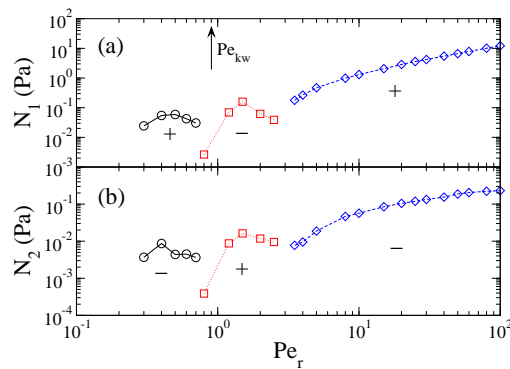

Figure 6.11: *The absolute values of the first and second normal stress differences of nematic solutions of rigid rods with $L/D = 25$ and $L\varphi/D = 3.5$, as a function of rotational Peclet number are plotted in (a) and (b) in log-log scale, respectively. The critical Peclet number of the kayaking to wagging transition Pe_{kw}, is represented by an arrow.*

As can be read from Fig. 6.11, the first change of sign occurs exactly at the transition from kayaking to wagging, indicated by an arrow at the upper horizontal axis, while the second change of sign occurs around the transition from wagging to flow-aligning, which is difficult to pinpoint otherwise. This complex behavior was first analyzed by Marrucci and Maffettone [97] on the basis of the two-dimensional analogue of the Doi-Hess theory. A three-dimensional analysis was provided by Larson [80] who found three distinct regions very much in agreement with our results. The elastic response of the flow aligned state is to

a large extent similar to that of the isotropic state. The orientational probability distribution is already rather narrow at zero shear, since we are in a nematic state. The flow has aligned this distribution along the flow direction and tried to narrow it just like in the isotropic state. The system is therefore rather similar to that in the isotropic state explaining the signs of N_1 and N_2, respectively.
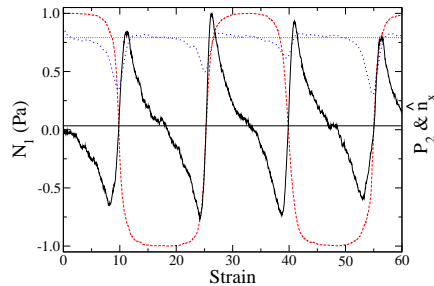

Figure 6.12: *The first normal stress difference N_1 (drawn curve), the scalar order parameter P_2 (dotted) and the x component of the director (dashed) of the nematic solution of rods with $L/D = 25$ and $L\varphi/D = 3.5$ as a function of strain. The upper and lower horizontal lines represent the equilibrium scalar order parameter and the time average of the first normal stress difference, respectively. At the applied shear rate $\dot{\gamma} = 125$ s^{-1}, the director exhibits a tumbling/kayaking motion.*

In Fig. 6.12 we have plotted the first normal stress difference N_1, the scalar order parameter P_2 and the x component of the director $\hat{n}_x$ of a tumbling system with $L/D = 25$, $L\varphi/D = 3.5$ and $\dot{\gamma} = 125$ s^{-1} as a function of strain. N_1 has been calculated on the basis of Eq. (6.7) including the term proportional to $d\mathbf{S}/dt$. We find that N_1 is basically equal to Σ_{xx}. From the plot we see that N_1 rises sharply every time when the rods tumble. After the rods have settled along the flow direction, P_2 is somewhat larger than its equilibrium value at the given value of $L\varphi/D$. N_1, and so also Σ_{xx}, begin to gradually decrease and become negative when P_2 drops below its equilibrium value. At this stage Σ_{xx} opposes the elastic forces caused by the fact that the orientational distribution is too wide for the given value of $L\varphi/D$. N_1 continues to decrease until the whole process starts again with the next tumbling.

As a final remark we notice that the normal stress differences N_1 and N_2 calculated by

Eq. (6.6) are monotonic against shear rate. Since this is not in agreement with experimental observation, we once more conclude that Eq. (6.7) provides a much safer expression to calculate stresses than Eq. (6.6).

6.4 Conclusion

We have calculated relative viscosities as well as first and second normal stress differences of suspensions of rigid liquid crystalline polymers in shear flow. To make this goal realizable, a recently developed event-driven Brownian dynamics algorithm was used. In this algorithm, excluded volume interactions between the rods are considered to be infinitely hard, but hydrodynamic interactions are neglected.

The general picture of the present Chapter is summarized as follows:

1. The suspensions of rigid rods exhibit shear thinning behavior in shear flow, both in isotropic and in nematic states.

2. In the isotropic phase, the measured shear thinning curves accord very well with the Hess equation. At low volume fractions or low shear rates, results by Dhont and Briels were confirmed. The self rotational diffusion coefficients calculated by fitting the simulation results with the Hess equation show good agreement with traditional measurements.

3. The inflexion points of the shear thinning curves of nematic systems are associated to the shear rates at which the director transforms its orientational motion from kayaking to wagging. Our calculated values of the inflexion points are in good agreement with those measured by investigating the motion of the director.

4. The first normal stress difference N_1 in nematic solutions of rigid rods is positive at low or high shear rates, but negative when intermediate shear rates are employed. The second normal stress difference N_2 is found always with opposite sign to that of N_1 and much smaller in amplitude. These fascinating behaviors are rather distinguished compared to the monotonic properties that are exhibited by isotropic solutions. Our simulation results qualitatively confirm both theoretical predictions and experimental measurements.
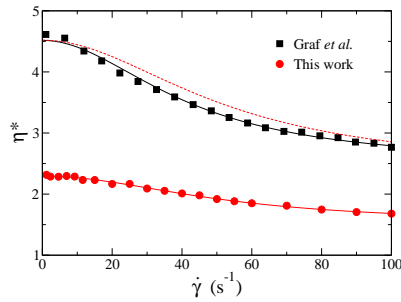
Figure 6.13: *Relative viscosities of solutions of fd viruses (squares: experimental [53] with* 1.56 mg/ml *fd in* 100 mM *NaCl; circles: simulations with* $L/D = 60$ *and* $L\varphi/D = 0.5$*) as a function of shear rate. Solid curves are fits using the Hess theory Eq. (6.12) on the basis of experimental and simulation data, respectively. The dashed curve denotes the simulated viscosities following a rescaling by* $1 + \frac{\eta^*_{\text{exp}}(0)-1}{\eta^*_{\text{sim}}(0)-1}(\eta^*_{\text{sim}}(\dot{\gamma}) - 1)$*; see text for details.*

It is constructive to make a quantitative comparison between our simulations and experiments on rod-like polymers. In Fig. 6.13 we have plotted the experimental viscosities of isotropic solutions of *fd* viruses measured by Graf *et al.* [53]. Using a molar weight [88] of 1.64×10^7 g/mol and an effective aspect ratio of 60, the experimental density of 1.56 mg/ml corresponds to a scaled volume fraction of 0.5. Simulated viscosities of rod suspensions with $L/D = 60$ and $L\varphi/D = 0.5$ are shown as circles. The simulations deviate from the experiments by a factor of 2. Considering the inherent flexibility of the *fd* virus and the ionic strength in the aqueous solution, which highly affects the effective diameter of the virus, this discrepancy is reasonable. Scaling the contribution of the rods such that the simulated and experimental viscosities agree at zero shear rate makes them agree at all shear rates. This scaling amounts to multiplying $\eta^*_{\text{sim}}(\dot{\gamma}) - 1$, and hence α $L\varphi/D$, by a factor of $(\eta^*_{\text{exp}}(0) - 1)/(\eta^*_{\text{sim}}(0) - 1)$.

Summary

In this thesis we report on Brownian dynamics simulations of colloidal suspensions of rigid spherocylinders in shear flow. A widely investigated topic, rod-like liquid crystalline polymers (LCPs) in the nematic phase arouse much scientific interest, both theoretically and experimentally, not only due to the spectacular collective orientational motions that these systems perform under shear but also due to the peculiar rheological properties compared to those of the isotropic phase. The goal of our study is to simulate and to understand the dynamical and rheological behavior exhibited in shear flow. Our simulated systems are based on the *fd* virus, because this slightly flexible nearly monodisperse biopolymer is considered a convenient experimental representative for a rigid rod-like particle.

In order to test a recent microscopic theory by Dhont and Briels for the dynamics of suspensions of long and thin rigid rods, which confirmed and expanded the well-known theory by Doi, Edwards and Kuzuu, we perform computer simulations on solutions of rigid rod-like colloids. A Brownian dynamics (BD) simulation program is developed to follow the dynamics of the rods on the Smoluchowski time scale. For simplicity and efficiency, this model accounts for excluded volume interactions between rods by a repulsive force proportional to the overlap volume between two interacting rods, but neglects the relatively unimportant hydrodynamic interactions. This model is successfully applied to measure the self and collective rotational diffusion coefficients in dilute and semi-dilute solutions of hard rods, which are reported in *Chapter 2*. Moreover, it is found that the decay of the collective rotational diffusion coefficients with the scaled volume fraction is much quicker than predicted by the theory. This deviation is attributed to an oversimplification of dynamical correlations in the theory.

When focusing on concentrated solutions of rods, it unfortunately turns out that the interaction potentials cause unsurmountable difficulties when performing prolonged simulations of the highly elongated rods needed for a stable nematic phase. As a result of the random displacements and reorientations, considerable overlaps and even crossings can not be prevented, irrespective of the smallness of the timestep. To make these simulations feasible, we therefore develop an event-driven Brownian dynamics algorithm, combining the dynamics

equations of traditional fixed time step BD with the collision-based time step commonly used in simulations of hard spherical particles. The novelty of the method is in the fact that its time evolution is controlled by collisions, like in time of flight molecular dynamics simulations, and not by a potential preventing overlaps. The new algorithm takes the excluded volume interactions between particles into account as instantaneous collisions. The effect of shear flow is also included in this method. The resulting algorithm proves efficient at simulating concentrated solutions of rods, and displays a stable nematic phase for elongated rods. The speedup is at least one order of magnitude compared to the previous program!

In *Chapter 3*, we first validate the new algorithm by measuring self rotational diffusion coefficients in the semi-dilute region. The results from both algorithms show perfect agreement with each other and qualitative agreement with Doi's theoretical prediction, which has been also confirmed by the independent Brownian dynamics simulations by Cobb and Butler. The isotropic-nematic spinodals of solutions of rigid spherocylindrical colloids with various shape anisotropies in a wide range from 10 to 60 are investigated by means of the newly developed event-driven Brownian dynamics program. The calculated isotropic-nematic spinodals lie between the previously established binodals (Monte Carlo simulations by Bolhuis and Frenkel) in the phase diagram and extrapolate for infinitely long rods to Onsager's theoretical predictions. Moreover, we investigate the shear induced shifts of the spinodals, qualitatively confirming Dhont and Briels' theory of the critical shear rate at which the two spinodals merge and the isotropic-nematic phase transition ceases to exist.

For nematic solutions of rigid rods in shear flow, it has been predicted theoretically that the director (the average orientation of the anisotropic particles) exhibits a periodic orientational motion, *i.e.*, tumbling, kayaking, wagging, flow-aligning or log-rolling, depending on the applied shear rate and the initial configuration of the system. To investigate these rather spectacular motions, we perform event-driven Brownian dynamics simulations of rigid liquid-crystalline polymers with large aspect ratio in the nematic state in shear flow. The predicted collective periodic orientational motions are therefore observed directly. In *Chapter 4*, we present some snapshots to describe the collective periodic motion of rods in shear flow. Furthermore, we show the path traced out by the director on the unit sphere to clearly illustrate kayaking and wagging motions.

In *Chapter 5*, event-driven Brownian dynamics simulations of the nematic solutions of

rods with various aspect ratios and volume fractions are described in detail. By carefully examining the collective motions of rods at different shear rates, the kayaking period is found to be related to volume fraction, shape anisotropy and applied shear rate. The simulation results qualitatively confirm the theoretical predictions by Marrucci *et al.* and Larson *et al.* and quantitatively agree with the kayaking times of *fd* viruses measured experimentally by Lettinga *et al.* The critical shear rate at which a transition between kayaking and wagging occurs is found to depend strongly on the scaled volume fraction but only slightly on the shape anisotropy of the rods. Moreover, we briefly study sheared rigid rod systems with different initial configurations and map out the regions where the log-rolling type of motion is observed.

In *Chapter 6*, we extend our investigations to some rheological properties, *i.e.*, the viscosities and the first and second normal stress differences of solutions of rigid rods in shear flow. A shear thinning behavior is found both in the isotropic state and in the nematic state. The simulated first normal stress differences in the nematic liquid crystalline solutions exhibit positive values at low and high shear rates, but negative values at intermediate shear rates, while the second normal stress differences are always opposite in sign and much smaller in magnitude. These unusual phenomena which agree qualitatively with both theories and experiments of rod-like polymers, are distinct from the monotone behaviors shown in isotropic solutions.

The event-driven algorithm for hard spherocylinders can be applied to solutions of hard spheres with little modification. In our preliminary simulation results of the shear-behavior of crystals, a zig-zag motion between neighboring 111 layers of the FCC crystal lattice is observed when the flow direction is chosen parallel to a symmetry axis of this plane. Future work may be focused on taking the hydrodynamic interactions into account, which are omitted in the current efficient event-driven Brownian dynamics program, and simulating anisotropic colloidal (rod-like or disk-like) particles embedded in an explicit solvent. The solvent may even be a binary one which contains interfaces.

Samenvatting

In dit proefschrift beschrijven we Brownse dynamica simulaties van colloïdale suspensies van starre sferocilinders in een afschuifstroming. Dit is een veel onderzocht onderwerp: staafvormige vloeibaar kristallijne polymeren (liquid crystalline polymers, LCPs) in de nematische fase hebben veel wetenschappelijke aandacht getrokken, zowel op theoretisch als op experimenteel vlak, niet alleen vanwege de spectaculaire collectieve oriëntationele bewegingen van deze systemen in een afschuifstroming, maar ook door hun bijzondere reologische eigenschappen in vergelijking tot de isotrope fase. Het doel van dit onderzoek is om het dynamische en reologische gedrag in een afschuifstroming te simuleren en te doorgronden. Ons gesimuleerde systeem is gebaseerd op het *fd* virus, omdat dit licht flexibele, bijna monodisperse biopolymeer als een handige experimentele representant van een star staafvormig deeltje beschouwd wordt.

We hebben computersimulaties aan oplossingen van starre staafvormige colloïden gebruikt voor het testen van een recente microscopische theorie van Dhont en Briels, die de bekende theorie van Doi, Edwards en Kuzuu voor de dynamica van suspensies van lange dunne staven bevestigt en uitbreidt. Een Brownse dynamica (BD) simulatie programma is ontwikkeld om de bewegingen van de staven op de Smoluchowski tijdschaal te volgen. Om wille van simpliciteit en efficiëntie worden de uigesloten-volume interacties tussen de staven berekend als een repulsieve kracht die evenredig is met het overlap volume van de twee interacterende staven, terwijl de relatief onbelangrijke hydrodynamische wisselwerkingen verwaarloosd worden. Dit model is met succes toegepast ter bepaling van de zelf- en collectieve rotationele diffusiecoëfficiënten in verdunde en semi-verdunde oplossingen van harde staven, zoals beschreven in hoofdstuk 2. De collectieve rotationele diffusiecoëfficiënt blijkt met stijgende volume fracties veel sneller te vervallen dan door de theorie voorspeld wordt. Dit verschil wordt toegeschreven aan een oversimplificatie van de dynamische correlaties in de theorie.

Bij de overstap naar geconcentreerde oplossingen van staven blijkt evenwel dat de interactiepotentiaal tot onoverkomelijke problemen leidt wanneer langgerekte staven in een nematische fase voor langere tijden gesimuleerd worden. Ten gevolge van de random ver-

plaatsingen en rotaties kunnen aanzienlijke overlappen, en zelfs doorkruisingen, niet verhinderd worden, zelfs niet als er kleine tijdstappen gebruikt worden. Om deze simulaties toch mogelijk te maken hebben we een 'event-driven' Brownse dynamica algoritme ontwikkeld, door de bewegingsvergelijkingen van traditionale vaste-tijdstap BD te combineren met een op botsingen gebaseerde tijdstap zoals die in simulaties van harde bollen gebruikelijk is. Het nieuwe aan deze methode is dat de tijdsontwikkeling nu bepaald wordt door botsingen, zoals in 'time-of-flight' moleculaire dynamica simulaties en niet door een potentiaal die overlap probeert te voorkomen. Het nieuwe algoritme brengt de uitgesloten-volume interacties tussen de deeltjes in rekening als instantane botsingen. De effecten van een afschuifstroming zijn ook opgenomen in de methode. Het resulterende algoritme blijkt efficiënt in het simuleren van geconcentreerde oplossingen van staven en vertoont een stabiele nematische fase voor langgerekte staven. De versnelling ten opzichte van het vorige programma is op zijn minst een factor tien.

In hoofdstuk 3 wordt het nieuwe algoritme allereerst gevalideerd door de zelf rotationele diffusiecoëfficiënt in een semi-verdunde oplossing te meten. De resultaten van beide algoritmes zijn in goede overeenstemming met elkaar en in kwalitatieve overeenstemming met de theoretische voorspellingen van Doi, die ook bevestigd werden door de onafhankelijke Brownse dynamica simulaties van Cobb en Butler. De isotroop-nemaat spinodalen van oplossingen van starre sferocilindrische colloïden met lengte-tot-diameter verhoudingen van 10 tot 60 zijn onderzocht met het nieuw ontwikkelde event-driven Brownse dynamica programma. De berekende isotroop-nemaat spinodalen liggen in het fasediagram tussen de eerder berekende binodalen (Monte Carlo simulaties van Bolhuis en Frenkel), en extrapoleren voor oneindig hoge aspect-ratio naar Onsagers theoretische voorspellingen. Tevens wordt de verschuiving van de spinodalen onder afschuifstromingen onderzocht, resulterend in een kwalitatieve bevestiging van de theorie van Dhont en Briels over de kritische afschuifsnelheid waarbij de twee spinodalen samenvloeien en de isotroop-nemaat faseovergang ophoudt te bestaan.

Voor nematische oplossingen van starre staven in een afschuifstroming wordt theoretisch voorspeld dat de director (de gemiddelde oriëntatie van de anisotrope deeltjes) een periodieke beweging vertoont, gekenschetst als 'tumbling' (tuimelen), 'kayaking' (kayakken), 'wagging' (kwispelen), 'flow-aligning' (stroom-gericht) of 'log-rolling' (boomstamrollen),

114

afhankelijk van de opgelegde afschuifsnelheid en de initiële configuratie van het systeem. Om deze spectaculaire bewegingen te onderzoeken gebruiken we event-driven Brownse dynamica simulaties van starre vloeibaar-kristallijne polymeren met een hoge aspect ratio in een nematische fase onder een afschuifstroming. De voorspelde collectieve periodieke oriëntationele bewegingen worden zo direct zichtbaar gemaakt. In hoofdstuk 4 wordt de collectieve periodieke beweging aan de hand van een aantal snapshots toegelicht. Tevens laten we het pad zien dat de director aflegt op de éénheidsbol, ter verduidelijking van de kayaking en wagging bewegingen.

In hoofdstuk 5 worden event-driven Brownse dynamica simulaties van nematische oplossingen van staven in detail beschreven voor een reeks van aspect-ratios en volumefracties. Door de collectieve beweging van de staven onder verschillende afschuifstroomsnelheden nauwkeurig te bekijken vinden we dat de periode van de kayakbeweging gerelateerd is aan de volumefractie, de anisotropie van de staaf en de opgelegde afschuifsnelheid. De simulatieresultaten bevestigen kwalitatief de theoretische voorspellingen van Marrucci *et al.* en Larson *et al.*, en zijn in quantitatieve overeenstemming met de kayakperiodes van *fd* virussen gemeten in de experimenten van Lettinga *et al.* De kritieke afschuifsnelheid waarbij een overgang plaatsvindt tussen kayaking en wagging blijkt sterk af te hangen van de anisotropie van de staven. Tevens hebben we afgeschoven systemen van starre staven met verschillende startconfiguraties bestudeerd en het domein bepaald waarbinnen de log-rolling beweging optreedt.

In hoofdstuk 6 breiden we onze onderzoekingen uit met enkele reologische eigenschappen, namelijk de viscositeit en de eerste en tweede 'normal stress differences' van oplossingen van starre staven in een afschuifstroming. Zowel de isotrope als de nematische fase vertonen 'shear-thinning' gedrag. In de simulaties van nematische vloeibaar kristallijne oplossingen is het eerste normal stress difference positief voor hoge en lage afschuifsnelheden maar negatief voor tussenliggende afschuifsnelheden, terwijl het tweede stress normal difference altijd het tegenovergestelde teken heeft en veel kleiner is. Deze ongewone verschijnselen stemmen kwalitatief overeen met zowel theorie als experimenten aan staafvormige polymeren en verschillen sterk van het monotone gedrag dat voor isotrope oplossingen gevonden wordt.

Het event-driven algoritme voor harde sferocilinders kan ook, na kleine aanpassingen, worden toegepast op oplossingen van harde bollen. In onze inleidende simulaties naar het

gedrag van kristallen onder een afschuifstroming vinden we een zig-zag beweging tussen naburige 111 vlakken van een FCC kristalrooster als de stroomrichting parallel aan een symmetrie-as van het vlak gekozen wordt. In toekomstig werk kan de hydrodynamische wisselwerking, die in het huidige efficiënte event-driven Brownse dynamica programma verwaarloosd wordt, in rekening worden gebracht bij de simulatie van anisotrope colloïdale staaf- of discusvormig deeltjes in een expliciet oplosmiddel. Het oplosmiddel kan zelfs een binair mengsel zijn met grensvlakken.

Acknowledgment

Just at the moment when this thesis is finished, I strongly realize that I own to acknowledge people who have given me great help during my four years in the University of Twente.

First and foremost, I want to extend deepest sense of gratitude to my promoter, Professor W. J. Briels, for offering me the opportunity pursuing my Ph.D. study in the group of Computational Biophysics. Dear Wim, thank you so much for your guidance and endless encouragement throughout all these years. I truly appreciate your personal advice and concern on my future. I also own to appreciate Professor J. K. G. Dhont for many useful discussions on almost all the aspects of my research work. The Dhont-Briels theory enhanced my academic knowledge greatly.

I wish to express my humble regards to two young scientists in my group: Dr. Ir. J. T. Padding and Dr. Ir. W. K. den Otter. Dear Johan, I appreciate your active suggestions which lead me into the gate of Molecular Simulation. Dear Wouter, thank you very much for your thoughtful consideration, unlimited patience, and always being available for discussions. Thanks a lot for teaching me so much and for spending an awful amount of time on my presentations, posters, and papers.

There are numerous people who made my life beautiful in the Netherlands. As a foreigner, I got a good deal of advice and support from my colleagues: Albert van der Noort, Peter Kindt, Sergey Shkulipa, Amol Thakre, Wladimir Shchettinin, Tanya Tolpekina, especially Marieke Janssen. My Chinese Friends: GANG Tian, ZHANG Zheng and LI Xiao, SONG Jing, GU Hao and YANG Lanti, CHEN Qi and MA Yujie, XU Jiang, I thank you very much for your company which makes me not feeling lonely any more.

Finally, and most importantly, I want to thank my wife, Shan, for the encouraging support and absolute understanding!

Yu-Guo TAO

Enschede, April 2006

117

Curriculum Vitae

Yu-Guo TAO was born on September 8th, 1975 in Changchun, P. R. China. In 1994, he entered the College of Chemistry, Jilin University (Changchun, China) without taking the National examinations due to his outstanding performance in Chemistry Olympiad (1994) of high school students all over China. Four years later, he obtained his Bachelor's degree (with distinction) in the institute of catalytic chemistry, Jilin University. In the same year, he joined the State Key Lab of Theoretical and Computational Chemistry and started his Master study on the subject of *ab initio* calculations on the mechanism of chemical reactions between small molecules and radicals. After his graduation at the end of 2001, he joined the Computational Biophysics group, University of Twente, the Netherlands, and became a Ph.D. student under the supervision of Prof. Dr. W. J. Briels. His Ph.D. research subject was focused on Brownian dynamics simulations of rigid liquid crystalline polymers in shear flow. Starting from June 1st, 2006, he will work in the research group of Prof. Dr. G. Gompper (Forschungszentrum Jülich, Germany) as a postdoctoral researcher.

List of publications

1. Yu-Guo Tao, W. K. den Otter, J. T. Padding, J. K. G. Dhont and W. J. Briels,

   Brownian dynamics simulations of the self- and collective rotational diffusion coefficients of rigid long thin rods,

   J. Chem. Phys., **122**, 244903, 2005.

2. Yu-Guo Tao, W. K. den Otter and W. J. Briels,

   Kayaking and wagging of rods in shear flow,

   Phys. Rev. Lett., **95**, 237802, 2005.

3. Yu-Guo Tao, W. K. den Otter, J. K. G. Dhont and W. J. Briels,

   Isotropic-nematic spinodals of rigid long thin rod-like colloids by event-driven Brownian dynamics simulations,

   J. Chem. Phys., **124**, 124904, 2006.

4. Yu-Guo Tao, W. K. den Otter and W. J. Briels,

   Periodic orientational motions of rigid liquid-crystalline polymers in shear flow,

   J. Chem. Phys., In press, 2006.

5. Yu-Guo Tao, W. K. den Otter and W. J. Briels,

   Shear viscosities and normal stress differences of rigid liquid-crystalline polymers,

   Macromolecules, Submitted, 2006.

6. Yu-Guo Tao, W. K. den Otter and W. J. Briels,

   Do nematic liquid crystals really make a wagging or flow-aligning motion in shear flow?

   In preparation, 2006.

7. Yu-Guo Tao, W. K. den Otter and W. J. Briels,

   Shear simulation of Brownian hard spherical crystals,

   In preparation, 2006.

8. Yu-Guo Tao, Y.-H. Ding, J.-J. Liu, Z.-S. Li, X.-R. Huang and C.-C. Sun,

   Theoretical mechanistic study on the ion-molecule reactions of CCN^+/CNC^+ with H_2S,

   J. Phys. Chem. A, **106**, 2949, 2002.

9. Yu-Guo Tao, Y.-H. Ding, J.-J. Liu, Z.-S. Li, X.-R. Huang and C.-C. Sun,

   Theoretical mechanistic study on the ion-molecule reactions of CCN^+/CNC^+ with H_2O and HCO^+/HOC^+ with HCN/HNC,

   J. Chem. Phys., **116**, 1892, 2002.

10. Yu-Guo Tao, Y.-H. Ding, J.-J. Liu, Z.-S. Li, X.-R. Huang and C.-C. Sun,

    Theoretical study on reaction mechanism of the CF radical with nitrogen dioxide,

    J. Comput. Chem., **22**, 1907, 2001.

11. Yu-Guo Tao, Y.-H. Ding, Z.-S. Li, X.-R. Huang and C.-C. Sun,

    Theoretical study on triplet potential energy surface of the $CH(^2\Pi) + NO_2$ reaction,

    J. Phys. Chem. A, **105**, 9598, 2001.

12. Yu-Guo Tao, Y.-H. Ding, Z.-S. Li, X.-R. Huang and C.-C. Sun,

    Theoretical study on reaction mechanism of methylidyne radical with nitrogen dioxide,

    J. Phys. Chem. A, **105**, 3388, 2001.

Bibliography

[1] M. P. Allen and D. J. Tildesley. *Computer Simulation of Liquids*. Clarendon, Oxford, 1987.

[2] A. R. Altenberger and J. S. Dahler. *Macromolecules*, 18:1700, 1985.

[3] E. Anczurowski and S. G. Mason. *J. Colloid Interface Sci.*, 23:522, 1967.

[4] E. Anczurowski and S. G. Mason. *J. Colloid Interface Sci.*, 23:533, 1967.

[5] N. C. Andrews, A. J. McHugh, and B. J. Edwards. *J. Rheol.*, 40:459, 1996.

[6] L. A. Archer and R. G. Larson. A molecular theory of flow-alignment and tumbling in sheared nematic liquid-crystals. *J. Chem. Phys.*, 103:3108, 1995.

[7] S.-G. Baek, J. J. Magda, and R. G. Larson. *J. Rheol.*, 37:1201, 1993.

[8] S.-G. Baek, J. J. Magda, R. G. Larson, and S. D. Hudson. *J. Rheol.*, 38:1473, 1994.

[9] Th. M. A. O. M. Barenbrug, E. A. J. Peters, and J. D. Schieber. *J. Chem. Phys.*, 106:8624, 1997.

[10] P. G. Bolhuis and D. Frenkel. *J. Chem. Phys.*, 106:666, 1997.

[11] P. G. Bolhuis, A. Stroobants, D. Frenkel, and H. N. W. Lekkerkerker. *J. Chem. Phys.*, 107:1551, 1997.

[12] W. J. Briels. *Theory of Simple Liquids*. Lecture notes, Uppsala University, 1993.

[13] W. J. Briels. *Theory of Polymer Dynamics*. Lecture notes, Uppsala University, 1994.

[14] W. R. Burghardt and G. G. Fuller. *Macromolecules*, 24:2546, 1991.

[15] D. Chandler. *Introduction to Modern Statistical Mechanics*. Oxford University Press, New York, 1987.

[16] C. V. Chaubal, L. G. Leal, and G. H. Fredrickson. *J. Rheol.*, 39:73, 1995.

[17] A. W. Chow, R. D. Harlin, and C. M. Ylitalo. *Macromolecules*, 25:7135, 1992.

[18] B. Cichocki and K. Hinsen. *Physica A*, 166:473, 1990.

[19] P. D. Cobb and J. E. Butler. *J. Chem. Phys.*, 123:054908, 2005.

[20] J. S. Dahler, S. Fesciyan, and N Xystris. *Macromolecules*, 16:1673, 1983.

[21] R. M. Davis and W. B. Russel. *Macromolecules*, 20:518, 1987.

[22] J. K. G. Dhont. *An Introduction to Dynamics of Colloids*. Elsevier, Amsterdam, 1996.

[23] J. K. G. Dhont and W. J. Briels. *J. Chem. Phys.*, 117:3992, 2002.

[24] J. K. G. Dhont and W. J. Briels. *Colloids Surfaces A*, 213:131, 2003.

[25] J. K. G. Dhont and W. J. Briels. *J. Chem. Phys.*, 118:1466, 2003.

[26] J. K. G. Dhont and W. J. Briels. *Phys. Rev. E*, 72:031404, 2005.

[27] J. K. G. Dhont, M. P. B. van Bruggen, and W. J. Briels. *Macromolecules*, 32:3809, 1999.

[28] J. Ding and Y. Yang. *Rheol. Acta*, 33:405, 1994.

[29] J. Ding and Y. Yang. *Polymer*, 37:5301, 1996.

[30] Z. Dogic and S. Fraden. *Phil. Trans. R. Soc. Lond. A*, 359:997, 2001.

[31] Z. Dogic and S. Fredan. *Curr. Opin. Coll. Int. Sci., in press*, 2006.

[32] Z. Dogic, K.R. Purdy, E. Grelet, M. Adams, and S. Fraden. *Phys. Rev. E*, 69:051702, 2004.

[33] M. Doi. *J. Polym. Sci., Polym. Phys. Ed.*, 19:229, 1981.

[34] M. Doi and S. F. Edwards. *J. Chem. Soc. Faraday Trans. II*, 74:560, 1978.

[35] M. Doi and S. F. Edwards. *J. Chem. Soc. Faraday Trans. II*, 74:918, 1978.

[36] M. Doi and S. F. Edwards. *The Theory of Polymer Dynamics*. Clarendon, Oxford, 1986.

[37] M. Doi, I. Yamamoto, and F. Kano. *J. Phys. Soc. Japan*, 53:3000, 1984.

[38] J. L. Ericksen. *Arch. Ration. Mech. Anal.*, 4:231, 1960.

[39] D. L. Ermak and J. A. McCammon. *J. Chem. Phys.*, 69:1352, 1978.

[40] J. J. Erpenbeck and J. G. Kirkwood. *J. Chem. Phys.*, 38:1023, 1963.

[41] V. Faraoni, M. Grosso, S. Crescitelli, and P. L. Maffettone. *J. Rheol.*, 43:829, 1999.

[42] S. Fesciyan and J. S. Dahler. *Macromolecules*, 15:517, 1982.

[43] P Fischer. *Rheol. Acta*, 39:234, 2000.

[44] M. Forest, Q. Wang, and R. H. Zhou. *Rheol. Acta*, 43:17, 2003.

[45] M. Forest, Q. Wang, and R. H. Zhou. *Rheol. Acta*, 44:80, 2004.

[46] D. Forster. *Phys. Rev. Lett.*, 32:1161, 1974.

[47] S. Fraden. *Phase Transition in Colloidal Suspensions of Virus Particles*. Kluwer Academic, Dordrecht, 1995.

[48] D. Frenkel and J. F. Maguire. *Mol. Phys.*, 49:503, 1983.

[49] Ch. Gähwiller. *Phys. Rev. Lett.*, 28:1554, 1972.

[50] E. Garcia, D. C. Williamson, and A. Martinez-Richa. *Mol. Phys.*, 98:179, 2000.

[51] C. W. Gardiner. *Handbook of Stochastic Methods*. Springer, Berlin, 1985.

[52] G. Germono and F. Schmid. *J. Chem. Phys.*, 123:214703, 2005.

[53] C. Graf, H. Kramer, M. Deggelmann, M. Hagenbüchle, C. Johner, and R. Weber. *J. Chem. Phys.*, 98:4920, 1993.

[54] G. W. Gray and J. W. Goodby. *Smectic Liquid Crystals*. Leonard Hill Publishers, London, 1984.

[55] F. Greco and G. Marrucci. *Liq. Cryst.*, 22:11, 1997.

[56] M. Grosso, S. Crescitelli, E. Somma, J. Vermant, P. Moldenaers, and P. L. Maffettone. *Phys. Rev. Lett.*, 90:098304, 2003.

[57] M. Grosso, R. Keunings, S. Crescitelli, and P. L. Maffettone. *Phys. Rev. Lett.*, 86:3184, 2001.

[58] O. G. Harlen, R. R. Sundararajakumar, and D. L. Koch. *J. Fluid Mech.*, 388:355, 1999.

[59] S. Hess. *Z. Naturforsch. A*, 31:1034, 1976.

[60] S. Hess. *Physica A*, 87:273, 1977.

[61] S. Hess. *Z. Naturforsch. A*, 35:915, 1980.

[62] S. Hess and M. Kröger. *J. Phys.: Condens. Matter*, 16:S3858, 2004.

[63] D. M. Heyes and J. R. Melrose. *J. Non-Newtonian Fluid Mech.*, 46:1, 1993.

[64] A. Hijazi and M. Zoaeter. *Eur. Polym. J.*, 38:2207, 2002.

[65] E. J. Hinch and L. G. Leal. *J. Fuild Mech.*, 76:187, 1976.

[66] H. Hoffmann-Berling, D. A. Marvin, and H. Duerwald. *Z. Naturforsch B*, 18:876, 1963.

[67] K. Hongladarom and W. R. Burghardt. *Macromolecules*, 26:785, 1993.

[68] K. Hongladarom, W. R. Burghardt, S.-G. Baek, S. Cementwala, and J. J. Magda. *Macromolecules*, 26:772, 1993.

[69] S. Jain and C. Cohen. *Macromolecules*, 14:759, 1981.

[70] G. B. Jeffery. *Proc. R. Soc. Lond. Ser A*, 102:161, 1922.

[71] R. F. Kayser, Jr. and H. J. Raveché. *Phys. Rev. A*, 17:2067, 1978.

[72] J. G. Kirkwood. *J. Chem. Phys.*, 29:909, 1958.

[73] G. Kiss and R. S. Porter. *J. Polym. Sci. Polym. Symp.*, 65:193, 1978.

[74] G. Kiss and R. S. Porter. *J. Polym. Sci. Polym. Phys. Ed.*, 18:361, 1978.

[75] H. Kramer, M. Deggelmann, C. Graf, M. Hagenbüchle, C. Johner, and R. Weber. *Macromolecules*, 25:4325, 1992.

[76] M. Kröger. *Phys. Rep.*, 390:453, 2004.

[77] M. Kröger and H. S. Sellers. *J. Chem. Phys.*, 103:807, 1995.

[78] N. Kuzuu and M. Doi. *J. Phys. Soc. Japan*, 52:3486, 1983.

[79] N. Kuzuu and M Doi. *J. Phys. Soc. Japan*, 53:1031, 1984.

[80] R. G. Larson. *Macromolecules*, 23:3983, 1990.

[81] R. G. Larson. *Rheol. Acta*, 31:213, 1992.

[82] R. G. Larson. *The Structure and Rheology of Complex Fluids*. Oxford University Press, New York, 1999.

[83] R. G. Larson and M. Doi. *J. Rheol.*, 35:539, 1991.

[84] R. G. Larson and H. C. Öttinger. *Macromolecules*, 24:6270, 1991.

[85] G. Lasher. *J. Chem. Phys.*, 53:4141, 1970.

[86] S. H. Lee, H. S. Kim, and H. Pak. *J. Chem. Phys.*, 97:6933, 1992.

[87] H. N. W. Lekkerkerker, Ph. Coulon, R. van der Haegen, and R. Deblieck. *J. Chem. Phys.*, 80:3427, 1984.

[88] T. A. Lenstra, Z. Dogic, and J. K. G. Dhont. *J. Chem. Phys.*, 114:10151, 2001.

[89] F. M. Leslie. *Arch. Ration. Mech. Anal.*, 28:265, 1968.

[90] M. P. Lettinga and J. K. G. Dhont. *J. Phys.: Condens. Matter*, 16:S3929, 2004.

[91] M. P. Lettinga, Z. Dogic, H. Wang, and J. Vermant. *Langmuir*, 21:8048, 2005.

[92] M. P. Lettinga, K. Kang, A. Imhof, D. Derks, and J. K. G. Dhont. *J. Phys.: Condens. Matter*, 17:S3609, 2005.

[93] J. J. Magda, S.-G. Baek, K. L. DeVries, and R. G. Larson. *Macromolecules*, 24:4460, 1991.

[94] J. F. Maguire and J. P. McTague. *Phys. Rev. Lett.*, 45:1891, 1980.

[95] W. Maier and A. Saupe. *Z. Naturforsch. A*, 14:882, 1959.

[96] G. Marrucci. *Macromolecules*, 24:4176, 1991.

[97] G. Marrucci and P. L. Maffettone. *Macromolecules*, 22:4076, 1989.

[98] G. Marrucci and P. L. Maffettone. *J. Rheol.*, 34:1217, 1990.

[99] G. Marrucci and P. L. Maffettone. *J. Rheol.*, 34:1231, 1990.

[100] D. A. Marvin and H. Hoffmann-Berling. *Nature*, 197:517, 1963.

[101] S. C. McFrother, D. C. Williamson, and G. Jackson. *J. Chem. Phys.*, 104:6755, 1996.

[102] S. Meiboom and R. C. Hewitt. *Phys. Rev. Lett.*, 30:261, 1973.

[103] J. Mewis, M. Mortier, J. Vermant, and P. Moldenaers. *Macromolecules*, 30:1323, 1997.

[104] P. Model and M. Russel. *The Bacteriophages*. Edited by R. Clender, Plenum, New York, 1988.

[105] P. Moldenaers, G. Fuller, and J. Mewis. *Macromolecules*, 22:960, 1989.

[106] N. Mori, H. Fujioka, R. Semura, and K. Nakamura. *Rheol. Acta*, 42:102, 2003.

[107] N. Mori, Y. Semura, and K. Nakamura. *Mol. Cryst. Liq. Cryst.*, 367:3233, 2001.

[108] I. Moriguchi. *J. Chem. Phys.*, 117:9202, 1997.

[109] I. Moriguchi, K. Kawasaki, and T. Kawakastu. *J. Phys. II*, 5:143, 1995.

[110] H. Nakamura and K Okano. *Phys. Rev. Lett.*, 505:186, 1983.

[111] P. D. Olmsted and P. M. Goldbart. *Phys. Rev. A*, 46:4966, 1992.

[112] P. D. Olmsted and C.-Y. D. Lu. *Phys. Rev. E*, 60:4397, 1999.

[113] L. Onsager. *Phys. Rev.*, 62:558, 1942.

[114] L. Onsager. *Ann. N. Y. Acad. Sci.*, 51:627, 1949.

[115] E. A. J. Peters and Th. M. A. O. M. Barenbrug. *Phys. Rev. E*, 66:056701, 2002.

[116] E. A. J. Peters and Th. M. A. O. M. Barenbrug. *Phys. Rev. E*, 66:056702, 2002.

[117] P. Pieranski and G. Etienne. *Phys. Rev. Lett.*, 32:924, 1974.

[118] D. C. Rapaport. *The Art of Molecular Dynamics Simulation*. 2nd. Edition, Cambridge University Press, 2004.

[119] G. Rienäcker and S. Hess. *Physica A*, 267:294, 1999.

[120] G. Rienäcker, M. Kröger, and S. Hess. *Physica A*, 315:537, 2002.

[121] W. Schaertl and H. Sillescu. *J. Stat. Phys.*, 74:687, 1994.

[122] H. See, M. Doi, and R. Larson. *J. Chem. Phys.*, 92:792, 1990.

[123] T. Shimada, M. Doi, and K. Okano. *J. Chem. Phys.*, 88:7181, 1988.

[124] K. Shundyak and R. van Roij. *J. Phys.: Condens. Matter*, 13:4789, 2001.

[125] K. Shundyak and R. van Roij. *Phys. Rev. E*, 69:041703, 2004.

[126] A. Speranza and P. Sollich. *J. Chem. Phys.*, 117:5421, 2002.

[127] A. Speranza and P. Sollich. *Phys. Rev. E*, 67:061702, 2003.

[128] P. Strating. *Phys. Rev. E*, 59:2175, 1999.

[129] Y.-G. Tao, W. K. den Otter, and W. J. Briels. *Phys. Rev. Lett.*, 95:237802, 2005.

[130] Y.-G. Tao, W. K. den Otter, and W. J. Briels. *J. Chem. Phys., In Press*, 2006.

[131] Y.-G. Tao, W. K. den Otter, and W. J. Briels. *Macromolecules, Submitted*, 2006.

[132] Y.-G. Tao, W. K. den Otter, J. K. G. Dhont, and W. J. Briels. *J. Chem. Phys.*, 124:134906, 2006.

[133] Y.-G. Tao, W. K. den Otter, J. T. Padding, J. K. G. Dhont, and W. J. Briels. *J. Chem. Phys.*, 122:244903, 2005.

[134] H. Thurn, M. Löbl, and H. Hoffmann. *J. Phys. Chem.*, 89:517, 1985.

[135] P. Turq, F. Lantelme, and H. L. Friedman. *J. Chem. Phys.*, 66:3039, 1977.

[136] N. G. van Kampen. *Stochastic Processes in Physics and Chemistry*. North-Holland, Amsterdam, 1992.

[137] R. van Roij. *Euro. J. Phys.*, 26:S57, 2005.

[138] S. Varga, G. Jackson, and I. Szalai. *Mol. Phys.*, 93:377, 1998.

[139] G. J. Vroege and H. N. W. Lekkerkerker. *Rep. Prog. Phys.*, 55:1241, 1992.

[140] P. B. Warren. *J. Phys. I*, 4:237, 1994.

[141] S. R. Williams and A. P. Philipse. *Phys. Rev. E*, 67:051301, 2003.

[142] Y. Yamane, Y. Kaneka, and M. Doi. *J. Non-Newtonian Fluid Mech.*, 54:405, 1994.

[143] Y. Yamane, Y. Kaneka, and M. Doi. *J. Phys. Soc. Japan*, 64:3265, 1995.

[144] A. V. Zakharov, A. A. Vakulenko, and J. Thoen. *J. Chem. Phys.*, 118:4253, 2003.

[145] M. Z. Zirnsak, D. U. Hur, and D. V. Boger. *J. Non-Newtonian Fluid Mech.*, 54:153, 1994.